



## CORE-COLLAPSE SUPERNOVAE FROM 9 TO 120 SOLAR MASSES BASED ON NEUTRINO-POWERED EXPLOSIONS

TUGULDUR SUKHBOLD<sup>1</sup>, T. ERTL<sup>2,3</sup>, S. E. WOOSLEY<sup>1</sup>, JUSTIN M. BROWN<sup>1</sup>, AND H.-T. JANKA<sup>2</sup>

<sup>1</sup>Department of Astronomy and Astrophysics, University of California, Santa Cruz, CA 95064, USA

<sup>2</sup>Max-Planck-Institut für Astrophysik, Postfach 1317, D-85741 Garching, Germany

<sup>3</sup>Physik Department, Technische Universität München, James-Franck-Str. 1, D-85748 Garching, Germany

Received 2015 October 15; accepted 2016 January 26; published 2016 April 6

### ABSTRACT

Nucleosynthesis, light curves, explosion energies, and remnant masses are calculated for a grid of supernovae (SNe) resulting from massive stars with solar metallicity and masses from  $9.0$  to  $120 M_{\odot}$ . The full evolution is followed using an adaptive reaction network of up to 2000 nuclei. A novel aspect of the survey is the use of a one-dimensional neutrino transport model for the explosion. This explosion model has been calibrated to give the observed energy for SN 1987A, using five standard progenitors, and for the Crab SN using a  $9.6 M_{\odot}$  progenitor. As a result of using a calibrated central engine, the final kinetic energy of the SN is variable and sensitive to the structure of each pre-SN star. Many progenitors with extended core structures do not explode, but become black holes (BHs), and the masses of exploding stars do not form a simply connected set. The resulting nucleosynthesis agrees reasonably well with the Sun provided that a reasonable contribution from SNe Ia is also allowed, but with a deficiency of light s-process isotopes. The resulting neutron star initial mass function has a mean gravitational mass near  $1.4 M_{\odot}$ . The average BH mass is about  $9 M_{\odot}$  if only the helium core implodes, and  $14 M_{\odot}$  if the entire pre-SN star collapses. Only  $\sim 10\%$  of SNe come from stars over  $20 M_{\odot}$ , and some of these are Type Ib or Ic. Some useful systematics of Type IIp light curves are explored.

**Key words:** nuclear reactions, nucleosynthesis, abundances – stars: black holes – stars: massive – stars: neutron – supernovae: general

*Supporting material:* FITS files

### 1. INTRODUCTION

The study of nucleosynthesis in massive stars has a rich history (e.g., Burbidge et al. 1957; Woosley & Weaver 1995; Thielemann et al. 1996; Woosley et al. 2002; Nomoto et al. 2013). These studies have frequently taken the form of a detailed analysis for individual events, e.g., SN 1987A (87A), or surveys for stars of just a few different masses. In some cases where broader surveys were done, the nucleosynthesis was calculated separately from any consideration of the explosion physics, and the central engine was linked in as a parameterized inner boundary condition for a calculation that included only the matter outside of the collapsing core. The explosion was parameterized either by dumping a prescribed amount of energy into inner zones or by the motion of a piston, generally constrained to give a fixed value of kinetic energy for the final supernova (SN). Sometimes this energy was varied over a limited range and the sensitivity of outcomes determined.

Here we report the results of a different approach. The starting point is an ensemble of 200 pre-SN models that together span the range of masses expected for common SNe ( $9.0$ – $120 M_{\odot}$ ). For the most part, these models or very similar ones have been published before (Woosley & Heger 2007, 2015; Sukhbold & Woosley 2014). All have solar metallicity. Each was calculated using the KEPLER code and identical stellar physics. The major innovation here is the treatment of the explosion mechanism. Two sorts of calculations of the explosion are carried out for each mass. Iron-core collapse and bounce, neutrino transport, and the propagation of the outgoing shock are followed in one simulation until sufficiently late that the final mass cut and explosion energy have been well

determined. This calculation, which includes a high-density equation of state (EOS) and neutrino transport that captures the essential effects of neutrinos, also gives an estimate of nucleosynthesis, especially for  $^{56}\text{Ni}$ . The second calculation tracks the results of the first in a study of detailed nucleosynthesis and radiation transport that gives the bolometric light curve. A consistent mapping between the two codes gives, for each pre-SN star, very nearly the same remnant mass, kinetic energy at infinity, and  $^{56}\text{Ni}$  mass. Nucleosynthesis is calculated for all isotopes from hydrogen through lead, except that the nucleosynthesis in the neutrino wind is not included.

Both calculations are one-dimensional (1D). While the actual physics of neutrino-powered SNe cannot be fully represented in a such a limited study (Janka 2012; Burrows 2013; Foglizzo et al. 2015), multidimensional models are expensive, are scarce, and often lack community consensus. Of necessity, an expedient track is adopted that should capture many characteristics of a real explosion. The 1D core-collapse code is used to calculate the explosion of five different progenitors for SN 1987A (Ertl et al. 2015) and one progenitor for SN 1054 (the “Crab”; Section 2.2.2). Adjustable parameters in the central engine model are varied to give the well-determined  $^{56}\text{Ni}$  mass, kinetic energy, and neutrino burst timescale for SN 1987A and the kinetic energy of the Crab. Based on the systematics of pre-SN core structure (Section 3.1.3), SNe below  $12.0 M_{\odot}$  are deemed to be “Crab-like,” while heavier stars are “87A-like.” Further partition of the mass space might be practical given more observational constraints, especially SNe with well-determined masses, but was not attempted here.

These central engines are then used to explore the outcomes when placed in the 200 pre-SN stars. The use of these

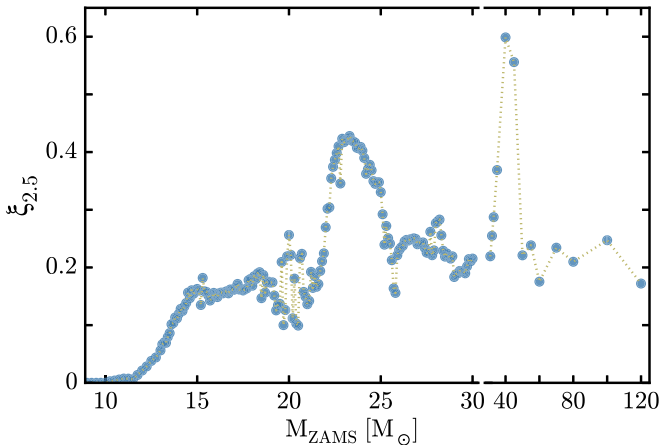


**Figure 1.** Compactness parameter,  $\xi_{2.5}$  (Equation (1); O’Connor & Ott 2011), characterizing the inner  $2.5 M_\odot$  of the pre-SN star shown as a function of zero-age main-sequence (ZAMS) mass for all 200 models between 9.0 and  $120 M_\odot$ . The compactness was evaluated when the collapse speed anywhere in the core first exceeded  $1000 \text{ km s}^{-1}$ . Studies have shown little difference for  $\xi_{2.5}$  evaluated at this time and at core bounce (Sukhbold & Woosley 2014). Note the scale break at  $32 M_\odot$ . Above about  $40 M_\odot$  the compactness parameter declines to a nearly constant value owing to the reduction of the helium core by mass loss. Stars below  $12 M_\odot$  have an especially dilute density structure around the iron core, owing to the lingering effects of degeneracy on the late stages of evolution. Stars below  $15 M_\odot$  (helium core mass below  $4 M_\odot$ ) explode comparatively easily, while stars from  $22$  to  $26 M_\odot$  are hard to explode.

“calibrated central engines,” which are really just standardized descriptions of the inner  $1.1 M_\odot$  of the proto-neutron star (PNS), allows a calculation of the neutrino and accretion physics outside the inner core that depends sensitively on the structure of individual pre-SN stars. For some models, the standard central engine is unable to provide enough energy for explosion, and a black hole (BH) forms. For others, the star explodes with a variable amount of kinetic energy. For the stars that do explode, the resulting patterns of SN energetics, nucleosynthesis, remnant masses, and light curves are reasonable for four out of five of the calibrations for SN 1987A. One set of calculations that used a model for SN 1987A that exploded too easily gave explosions that, on average, were deemed too weak. In this case an inadequate number of stars exploded to make the abundances we see in the Sun (Section 4). Thus, nucleosynthesis was not studied in detail using this model as a basis.

We are particularly interested in how the “explodability” of the pre-SN models and their observable properties correlate with their “compactness” (Figure 1; O’Connor & Ott 2011),

$$\xi_M = \frac{M/M_\odot}{R(M)/1000 \text{ km}}|_{t_{\text{bounce}}}, \quad (1)$$

and other measures of pre-SN core structure (Section 3.1.3; Ertl et al. 2015). Using a standard central engine in pre-SN models of variable compactness, a significant correlation in outcome is found (Section 4). As previously suggested, the resulting mass spectrum of successful SNe is not simply connected (O’Connor & Ott 2011; Ugliano et al. 2012; Sukhbold & Woosley 2014). That is, there is no single mass above which stars make BHs and below which they explode. Rather, there are mass ranges that “tend” to explode, albeit with significant variations, even in narrow ranges. The model stars below  $15 M_\odot$  always explode easily, while those in the range  $22$ – $25 M_\odot$  and  $27$ – $30 M_\odot$  rarely

explode. The outcome for other masses is either variable ( $15$ – $22 M_\odot$  and  $25$ – $27 M_\odot$ ) or sensitive to the treatment of mass loss ( $M > 30 M_\odot$ ).

The input physics and the systematics for all of the progenitors, including the models used for the explosion calibrations, have been discussed in previous publications, but they are summarized in Section 2. Details of the explosion modeling for both the P-HOTB code, which is used to study core collapse, and the KEPLER code, which is used to calculate nucleosynthesis and light curves, and how agreement is enforced between the two codes are discussed in Section 3. The properties of the explosions in relation to the progenitor compactness parameter, especially their explosion energies and  $^{56}\text{Ni}$  masses, are addressed in Section 4, and the mass distributions of neutron stars and BHs from the explosions are discussed in Section 5. The resulting nucleosynthesis from different mass ranges and the integrated yields for different element groups are examined in Section 6, and the light curves of various types emerging from the explosions and their systematics are analyzed in Section 7. In Section 8, we offer some conclusions.

## 2. Pre-SN PHYSICS AND MODELS

### 2.1. Stellar Physics

All pre-SN models were calculated using the KEPLER code (Weaver et al. 1978), the physics of which has been previously discussed (e.g., Woosley et al. 2002), and are included in the electronic edition in a tar.gz package. Indeed, most of the models, or very similar ones, have been published previously (Woosley & Heger 2007, 2015; Sukhbold & Woosley 2014). All stars, except for one model used for the calibration of 87A, were nonrotating. Except for the calibration models for 87A and the Crab (Section 2.2), each had an initially solar (Lodders 2003) composition. All were evolved from the main sequence until the onset of iron-core collapse. The lower bound to the survey,  $9.0 M_\odot$ , is set by the lightest star to experience iron-core collapse in the KEPLER code (Woosley & Heger 2015). The evolution of still lighter stars in the  $7$ – $9 M_\odot$  range was not calculated. Some uncertain fraction of these will evolve to electron-capture SNe and contribute to the SN rate and remnant distribution. Those contributions are neglected here. Their contribution to nucleosynthesis, other than the *r*- and *s*-processes, is likely to be small, however.

Full stars, including their hydrogenic envelopes, were calculated, and mass loss was included (Nieuwenhuijzen & de Jager 1990; Wellstein & Langer 1999; Woosley et al. 2002). The nuclear physics varied (though not the individual reaction rates). A rate for  $^{12}\text{C}$  ( $\alpha, \gamma$ )  $^{16}\text{O}$  equal to 1.2 times that of Buchmann (1996) was employed. For stars  $13.0 M_\odot$  and heavier, including the models for SN 1987A, the evolution up to core oxygen depletion was followed using a 19-isotope approximation network and, after central oxygen decreased to below 4% by mass, using a 128-isotope quasi-equilibrium network (Weaver et al. 1978). Those calculations were “co-processed” using an adaptive network (Rauscher et al. 2002) that, near the end, typically included 1500 isotopes, and sometimes over 2000. In addition to following the nucleosynthesis zone by zone and step by step, the evolution of the (slowly evolving) electron mole number,  $Y_e$ , calculated by the large network, was fed back into the structure calculation.

Energy generation within an iterative loop, however, came from the 19-isotope network or the quasi-equilibrium network.

For stars lighter than  $13 M_{\odot}$ , the tracking of off-center burning and convectively bounded flames requires a more careful treatment of the nuclear physics (Woosley & Heger 2015). For these stars, the large network and all neutrino losses from weak reactions on individual nuclei were coupled directly to the structure calculation. The 19-isotope network and quasi-equilibrium network were not employed. Several stars in the  $12\text{--}13 M_{\odot}$  range were computed using both the direct coupling of the big network and co-processing. The results were nearly identical.

During the explosion, all shock-induced transformations were followed, as well as nucleosynthesis by the neutrino process (Woosley et al. 1990; Heger et al. 2005). The  $r$ -,  $s$ -, and  $\gamma$ -processes were all followed in matter outside the iron core, but nucleosynthesis in the neutrino-powered wind was not followed in any detail.

Formally, only single stars were included. The key quantity for nucleosynthesis and remnant masses is the mass of the core of helium and heavy elements at the time of the explosion. To the extent that the Salpeter initial mass function (IMF) properly reflects this distribution of helium core masses, our results would not be changed if a substantial fraction of the stars were in binary systems. If mass exchange proceeds so far as to appreciably reduce the mass of the helium core from what it would have been for a single star, including radiatively driven mass loss, then the answer will change. For example, it seems most likely that common SNe Ib and Ic result from binary systems containing stars whose pre-SN mass is only  $3$  or  $4 M_{\odot}$  (Enzman & Woosley 1988; Dessart et al. 2012). Many of these may come from  $12\text{--}15 M_{\odot}$  main-sequence stars that lost their envelopes and little else to a companion. Treating these as single stars does not greatly distort the nucleosynthetic outcome, though it obviously changes the rate of SNe Ib and Ic a lot. If the progenitors in binaries were much heavier, some of their nucleosynthesis, especially in the helium shell, might have been lost to a companion, and it becomes an issue whether that star blows up, returning what it accreted to the interstellar medium. If more massive stars in binaries are involved in making SNe Ic, then our results would be altered. The explosion of stripped down  $4 M_{\odot}$  cores of oxygen and heavy elements is different from the explosion of a  $4 M_{\odot}$  helium core, in both mechanism and consequence (Woosley et al. 1993). However, such SNe are relatively rare, and we do not expect substantial changes from what we report here. Including the contributions of SN Ib and Ic models explicitly would be a worthwhile project for the future.

## 2.2. Calibration Models

### 2.2.1. SN 1987A

The pre-SN evolution of Sk  $-69^{\circ}$  202 and its explosion as SN 1987A have been studied extensively for almost 30 yr (e.g., Arnett et al. 1989; Utrobin et al. 2014, and references therein), yet a comprehensive, self-consistent model for the progenitor star, its ring structure, and the explosion is still lacking. The observational constraints are tighter, though, than for any other SN, so it is worthwhile to try to use SN 1987A as a calibration point.

It is known that the progenitor star was a Type B3-I blue supergiant, Sk  $-69^{\circ}$  202 (Walborn et al. 1987), with an

effective temperature of  $14,000\text{--}17,000$  K (Humphreys & McElroy 1984; Crowther et al. 2006; Smith 2007), a luminosity of  $3\text{--}6 \times 10^{38}$  erg s $^{-1}$  (Humphreys & McElroy 1984; Arnett et al. 1989), and thus a radius of  $2\text{--}4 \times 10^{12}$  cm. Since the pre-SN luminosity is determined chiefly by the helium core mass, a core mass of  $6 \pm 1 M_{\odot}$  has been inferred theoretically (e.g., Woosley 1988). Based on analysis of the SN light curve, this core was surrounded by about  $10 M_{\odot}$  of envelope in which helium and nitrogen were enriched but hydrogen was still a major constituent (Shigeyama et al. 1988; Woosley 1988). The star had been a red supergiant before dying as a blue one in order to produce the colliding wind structure seen shortly after the explosion. Spectral analysis, as well as the light curve, gives an explosion energy near  $1.5 \times 10^{51}$  erg (Arnett et al. 1989; Utrobin et al. 2014), and the late-time light curve shows unambiguously that the explosion produced  $0.07 M_{\odot}$  of  $^{56}\text{Ni}$  (Bouchet et al. 1991; Suntzeff et al. 1992). The explosion also ejected approximately  $1.4 \pm 0.7 M_{\odot}$  of oxygen (Fransson & Kozma 2002).

### 2.2.1.1. Models for Sk $-69^{\circ}$ 202

Numerous attempts have been made to model the pre-SN evolution of Sk  $-69^{\circ}$  202. The final stages are complicated by the widespread belief that SN 1987A may have been a merger event (Podsiadlowski 1992; Morris & Podsiadlowski 2007), though see Smith (2007). In any case, the star that exploded was single at the time, in hydrostatic and, given the necessary timescale for the red-to-blue transition, probably in approximate thermal equilibrium. Its helium core mass is thus constrained by the pre-SN luminosity, and so single-star models are relevant.

Five principal models for SN 1987A are considered here, the ones above the blank line in Table 1, and span the space of possible helium and heavy-element core structures (Figure 2). The 3D explosion and observable properties of four of them have been explored previously (Utrobin et al. 2014) and agree well with experimental data. These models are N20, W15, W18, and W20.

Model N20 (Shigeyama & Nomoto 1990; Nomoto & Hashimoto 1988; Saio et al. 1988), a historical model, was “prepared” by artificially combining the pre-SN structure of an evolved  $6 M_{\odot}$  helium core from one calculation with the hydrogen envelope from another. This model was thus defined to satisfy observational constraints on helium core mass, hydrogen envelope mass, radius, and luminosity, but lacks the physical basis of a pre-SN model evolved intact from the main sequence onward. Since the helium core of model N20 was evolved using the Schwarzschild criterion for convection (Nomoto & Hashimoto 1988), its carbon–oxygen (CO) core is large compared with some of the other models (Table 1), which used restricted semiconvection in order to produce a blue supergiant progenitor. It is not clear that, had the  $6 M_{\odot}$  core been included in a self-consistent calculation with an envelope always in place, a blue supergiant would have resulted rather than a red one.

Model W15 (Woosley et al. 1988), another early model calculated shortly after SN 1987A occurred, was produced by evolving a single  $15 M_{\odot}$  star from beginning to end, but relied on opacities that are now outdated, reduced metallicity, and greatly restricted semiconvection to produce a blue supergiant. Mass loss was not included. The small ratio (less than about 0.6) of the CO core mass to helium core mass in W15 is

**Table 1**  
SN 1987A Models

Model	$M_{\text{preSN}}/M_{\odot}$	$M_{\text{He}}/M_{\odot}$	$M_{\text{CO}}/M_{\odot}$	$L/10^{38} \text{ erg s}^{-1}$	$T_{\text{eff}}$	$\zeta_{2.5}$	$Z/Z_{\odot}$	Rotation
W18	16.93	7.39	3.06	8.04	18,000	0.10	1/3	Yes
N20	16.3	6	3.76	5.0	15,500	0.12	low	No
S19.8	15.85	6.09	4.49	5.65	3520	0.13	1	No
W15	15	4.15	2.02	2.0	15,300	...	1/4	No
W20	19.38	5.78	2.32	5.16	13,800	0.059	1/3	No
W16	15.37	6.55	2.57	6.35	21,700	0.11	1/3	Yes
W17	16.27	7.04	2.82	7.31	20,900	0.11	1/3	Yes
W18x	17.56	5.12	2.12	4.11	19,000	0.10	1/3	Yes
S18	14.82	5.39	3.87	4.83	3520	0.19	1	No

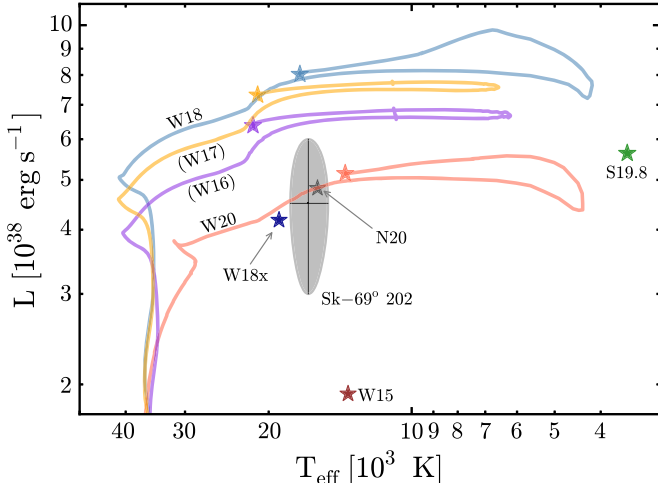


**Figure 2.** Hertzsprung–Russell diagram for the SN 1987A progenitors used in this study. The shaded region shows the observed properties of Sk –69° 202 (see text). Model S19.8 produced a red supergiant; all the rest gave blue supergiants at the time of core collapse, but were preceded by a phase as a red supergiant. Models W16, W17, W18, and W18x included rotation; the rest were nonrotating. Model N20 was a construct obtained by joining a  $6 M_{\odot}$  helium star to an envelope. All models beginning with a “W” were calculated using the KEPLER code assuming reduced metallicity and restricted semiconvection. Model W18x had  $3/4$  the angular momentum of Model W18, but was otherwise identical. See also Table 1.

characteristic of all models in Table 1 that produce blue supergiant progenitors. As far as we know, this is a hallmark of all solutions that use Ledoux convection or restricted semiconvection to achieve this goal. The helium core mass and luminosity of W15 are too small compared with more accurate observations of Sk –69° 202. Still, W15 is included here because it has been studied in the literature and it brackets, on the low side, the observed luminosity and helium core mass of Sk –69° 202 (Figure 2).

Model W20 (Woosley et al. 1997) used more modern opacities (Rogers & Iglesias 1992; Iglesias & Rogers 1996) and included mass loss. Its luminosity, radius, and helium core mass agree well with observations of Sk –69° 202 (Figure 2). Its pre-SN oxygen mass,  $0.68 M_{\odot}$ , is on the small side compared with observations (Fransson & Kozma 2002), especially when allowance is made for the processing of some oxygen into heavier elements during the explosion. The envelope is also not enriched in helium. The surface mass fraction of helium is 0.26.

Model W18 is a more recent unpublished model that will be presented in greater detail later in this section. It achieves the desired goals of making a blue supergiant progenitor,

producing a relatively large mass of oxygen, and displaying large enhancements in surface helium and nitrogen abundances, by invoking reduced metallicity, restricted semiconvection, and a substantial amount of rotation. Rotation makes the helium core larger and also stirs more helium into the envelope, raising the mean atomic weight there, and reducing the opacity. A larger helium core implies a larger luminosity, somewhat above the observed limit for SN 1987A (Figure 2), but the increased helium fraction in the envelope facilitates a blue solution (Saio et al. 1988; Langer 1992).

Three other models similar to W18 are also given in Table 1 and Figure 2 to illustrate some sensitivities, but were not used in the remainder of the paper. W16 and W17 are identical to W18 except for their different masses and rotation rates. The angular momentum on the ZAMS for models W16, W17, and W18 was  $J_{\text{ZAMS}} = (2.7, 2.9, 3.1) \times 10^{52} \text{ erg s}$ , respectively. The pre-SN core properties for W16 and W17 are similar to W18, and one would expect similar results were they to be employed as standard central engines. W18x, on the other hand, is slightly different in input physics, yet quite different in outcome. Like W18, W18x includes rotation, but the total angular momentum on the main sequence was reduced by  $\sim 25\%$  to  $J_{\text{ZAMS}} = 2.3 \times 10^{52} \text{ erg s}$ . This small reduction in  $J$  resulted in a dramatic decrease in the helium core mass and pre-SN luminosity (Table 1; Figure 2). Another model, not shown, with an angular momentum 50% of W18, gave almost identical results to W18x, showing that W18 itself was on the verge of becoming a chemically homogeneous model (Maeder 1987; Langer 1992; Woosley & Heger 2006). Nevertheless, we chose to use model W18 itself as one of our standard models because it gave reasonable agreement with the observed properties of Sk –69° 202; had a core structure similar to the nonrotating, solar-metallicity stars in the present survey; was available a few years ago when this study began; and had been previously studied in the literature (Utrobin et al. 2014; Ertl et al. 2015).

In addition to the above models with restricted semiconvection and low metallicity, a nonrotating, solar-metallicity red supergiant progenitor was also examined. “S19.8” (Woosley et al. 2002) was not considered by Utrobin et al., but has a similar helium core structure to W18 and N20 (Table 1). Because the surface boundary pressure is small in both cases, the structure of the helium core is insensitive to whether the envelope is that of a blue or red supergiant. Despite its vintage, model S19.8 was calculated using essentially the same initial composition and stellar physics as in the present survey—including opacities, mass loss, semiconvection, and metallicity. The luminosity, helium core mass, and hydrogen envelope mass of pre-SN model S19.8 are all what one would want for

SN 1987A, but the pre-SN star was a red supergiant. Also given in Table 1 is an  $18 M_{\odot}$  pre-SN model from the present survey. The luminosity is very similar to Sk –69° 202 and the structure similar to S19.8.

The point of these calculations was not to generate the best possible model for SN 1987A itself, but to use its well-studied properties to bracket and calibrate a central engine capable of exploding helium cores with similar characteristics. It was important to study a range of models to test the sensitivity of the results to the choice of a model for SN 1987A (see Section 4 for results).

### 2.2.1.2. The Pre-SN Evolution of Model W18

Because it will be used to generate one of the standard engines and is not documented in the refereed literature, model W18 warrants some additional description. The star had an initial mass of  $18.0 M_{\odot}$  and a composition of 74.6% H, 25.0% He, 0.052% C, 0.012% N, and 0.25% O, with traces of heavier elements. Its iron mass fraction was  $7.6 \times 10^{-4}$ . These abundances, which for CNO are roughly 1/3 of solar, may reflect the smaller metallicity of the Large Magellanic Cloud. The star was given sufficient angular momentum that, while burning hydrogen on the main sequence, its equatorial rotational speed was  $240 \text{ km s}^{-1}$ . On the main sequence, halfway through hydrogen burning, its luminosity and effective temperature were  $2.3 \times 10^{38} \text{ erg s}^{-1}$  and  $36,100 \text{ K}$ , respectively. The star spent most of its helium-burning lifetime as a blue supergiant with radius near  $2.5 \times 10^{12} \text{ cm}$ , a luminosity of  $7.7 \times 10^{38} \text{ erg s}^{-1}$ , and an effective temperature of  $20,000 \text{ K}$ . Only toward the end of its life, when the central helium mass fraction declined below 7%, did the radius increase above  $5 \times 10^{12} \text{ cm}$ . When the radius reached  $1 \times 10^{13} \text{ cm}$ , the helium mass fraction was only 1.5%. The radius continued to increase, reaching a maximum of  $6.2 \times 10^{13} \text{ cm}$  after helium had already been depleted, and the central temperature was  $3.6 \times 10^8 \text{ K}$ . The luminosity at that point was  $8.1 \times 10^{38} \text{ erg s}^{-1}$ .

Over the next 15,000 yr, the radius of the star shrank back to less than  $10^{13} \text{ cm}$ , and the star remained a blue supergiant for another 5000 yr before dying with a radius of  $3.3 \times 10^{12} \text{ cm}$  and luminosity  $8.04 \times 10^{38} \text{ erg s}^{-1}$ . At that time, its helium core mass (where hydrogen mass fraction equals 1%) was  $7.39 M_{\odot}$ . Nucleosynthesis in W18, prior to any explosion, included  $1.25 M_{\odot}$  of  $^{16}\text{O}$ , in agreement with observations suggesting an oxygen mass of  $1.4 \pm 0.7 M_{\odot}$  (Fransson & Kozma 2002). The helium mass fraction at the surface of the pre-SN star was 53%, in agreement with evidence for rotationally induced mixing (e.g., Saio et al. 1988; Weiss et al. 1988; Arnett et al. 1989). The final total star mass for W18 was  $16.92 M_{\odot}$ , and its iron-core mass was  $1.47 M_{\odot}$ , which was also the location of the entropy jump  $S/N_{Ak} = 4$  associated with the oxygen shell. Some further details of pre-SN composition and structure of W18 and our other models for SN 1987A are given in Utrobin et al. (2014) and Ertl et al. (2015).

Because the model included both rotation and the transport of angular momentum by magnetic torques (Heger et al. 2005), it was possible to estimate the importance of rotation and magnetic fields to the explosion. The angular momentum interior to  $1.47 M_{\odot}$  in the pre-SN model W18 was  $6.1 \times 10^{47} \text{ erg s}$ , implying a rotation rate of the resultant pulsar of about 12 ms. No pulsar has been discovered yet in SN

1987A, but this amount of rotation would be inadequate to provide the observed  $\sim 1.5 \times 10^{51} \text{ erg}$  explosion. It seems likely therefore that the explosion was neutrino powered.

In summary, W18 is the heaviest possible blue supergiant model for SN 1987A in terms of its helium core mass. While a bit overluminous, it fits many other observed characteristics of the SN well, especially the oxygen mass synthesized, and its central core structure is similar to other lighter models, W16 and W17. Table 1 of Ertl et al. (2015) shows that, at least in terms of compactness, W18 is quite similar to W20, N20, and S19.8.

### 2.2.2. SN 1054—the Crab

While the Crab SN was not studied spectroscopically, modern observations of its remnant suggest that the kinetic energy was much lower than that of SN 1987A and other common SNe from more massive stars (Arnett et al. 1989; Kasen & Woosley 2009; Yang & Chevalier 2015). The event has been successfully and repeatedly modeled as the explosion of a star near  $10 M_{\odot}$  (Nomoto et al. 1982; Nomoto 1987; Smith 2013; Tominaga et al. 2013). Such stars are known to have compact structures that explode easily by the neutrino-heating mechanism, even in spherical symmetry (Kitaura et al. 2006; Fischer et al. 2010; Melson et al. 2015). Use of an 87A-like central engine in stars of this sort thus overestimates the power of the SN and gives an unphysically large kinetic energy (Section 3.1.3). Systematics of the pre-SN core structure, to be discussed later, suggest that, for KEPLER models, this low-energy branch of SNe should characterize events from 9.0 (or less) to  $12.0 M_{\odot}$ .

The fiducial model employed to represent the core physics in this low-mass range was a  $9.6 M_{\odot}$  zero-metallicity model (Z9.6) provided by A. Heger (2012, private communication). This star was also calculated using the KEPLER code using physics described in Heger & Woosley (2010), and, while a star of zero metallicity, it has a very similar core structure to the lightest solar-metallicity models employed here (Figure 3). The model has the merit of having been successfully exploded in 1D and multidimensional calculations (Janka et al. 2012; Melson et al. 2015), developing an explosion dynamically similar to collapsing O–Ne–Mg core progenitors (Kitaura et al. 2006; Janka et al. 2008). It also gives similar nucleosynthesis to the electron-capture SNe (S. Wanajo et al. 2015, in preparation) often mentioned as candidates for the Crab (Wanajo et al. 2011c; Jerkstrand et al. 2015), but has the advantage of being an iron-core-collapse SN similar to the ones we are currently modeling.

### 2.3. Pre-SN Models Used for This Study

The pre-SN models into which these calibrated central engines are placed are all the outcomes of nonrotating stars with initially solar metallicity. Mass loss was included in all calculations. Qualitatively, the models reflect four partitions of expected behavior (e.g., Woosley & Heger 2015):

1.  $9\text{--}12 M_{\odot}$ . These are stars with degenerate compact cores, essentially tightly bound white-dwarf-like cores inside loosely bound envelopes. They are easy to explode. Starting at  $9 M_{\odot}$ , an iron core is produced before the star dies. Slightly below  $9 M_{\odot}$ , an electron-capture SN results or an oxygen–neon white dwarf is made. The presence of an active oxygen-burning shell at the edge of the effective

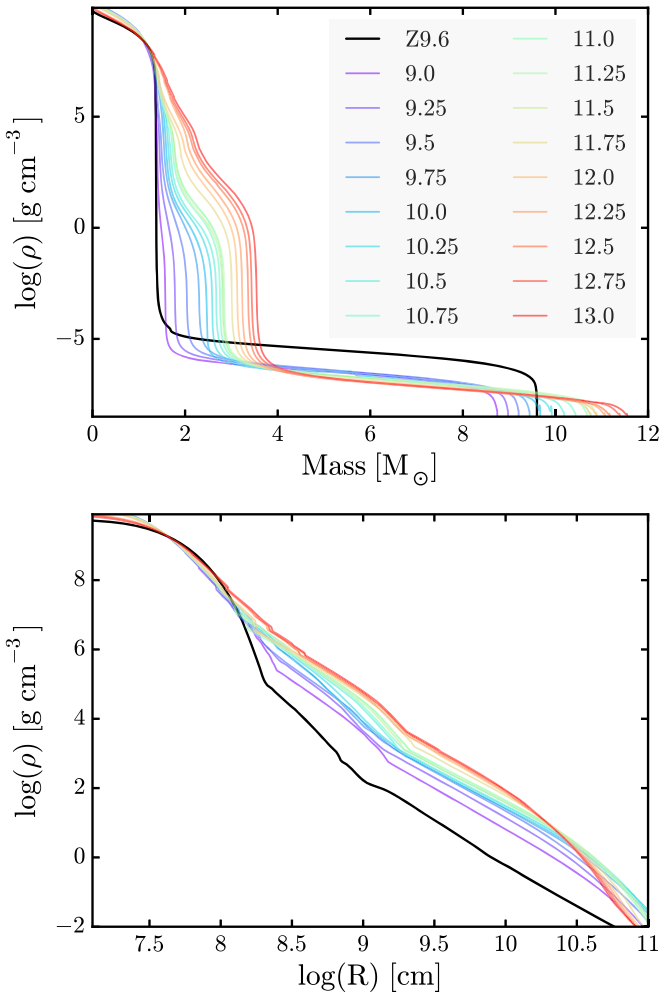


**Figure 3.** Density profiles for the 17 new pre-SN models used for stars from 9.0 to  $13.0 M_{\odot}$ . These have a high degree of central concentration and are relatively easy to explode. Also shown for comparison is the zero-metallicity calibration model used for Crab, Z9.6, which is similar in structure to the  $9.0 M_{\odot}$  solar-metallicity models studied here.

Chandrasekhar mass in the pre-SN star causes a rapid fall-off in density near the edge of a dense central core for models below  $12 M_{\odot}$ .

2.  $12-20 M_{\odot}$ . Starting at about  $10.5 M_{\odot}$ , all fuels ignite in the center of the star (Woosley & Heger 2015). The compactness parameter, Equation (1), which is a measure of the core’s density structure, increases rapidly from 12 to  $15 M_{\odot}$  and then remains roughly constant (Figure 1). Carbon ignites exoergically and powers convection in all stars up to about  $20 M_{\odot}$ , and models near the transition to radiative central carbon burning end up creating highly variable pre-SN core structures (Sukhbold & Woosley 2014). The central core is degenerate and is surrounded by helium and heavy-element shells of increasing thickness. Most of these stars are also relatively easy to explode.
3.  $20-30 M_{\odot}$ . These stars ignite central carbon burning endoergically and are thus not convective during a critical phase when excess entropy might have been radiated by neutrinos. Thick shells of oxygen, neon, and carbon contribute appreciably to nucleosynthesis but, depending on the location of carbon- and oxygen-burning shells

during the later stages of evolution, lead to a greater compactness parameter. These stars may be difficult to explode (Sukhbold & Woosley 2014).

4. Above  $30 M_{\odot}$ , pre-SN stars have increasingly thick shells of heavy elements and shallow density gradients around large iron cores, making them difficult to explode with neutrinos. Mass loss plays a very important role. For the assumed prescription, the pre-SN mass actually decreases with increasing initial mass above  $23.5 M_{\odot}$ . The maximum pre-SN mass there is  $\sim 16.5 M_{\odot}$ . Rotation may be increasingly important to the explosion mechanism of stars in this mass range (Heger et al. 2005). If mass loss succeeds in removing the entire hydrogen envelope, as it did here for main-sequence stars above  $40 M_{\odot}$ , these stars may explode as an SN Ib or Ic.

Because of their different characteristics, these mass ranges are often modeled separately. Our models for  $9-13 M_{\odot}$  stars,  $13-30 M_{\odot}$  stars, and  $30-120 M_{\odot}$  stars come from different studies, but all were calculated using the KEPLER code. All pre-SN models, along with data from Sections 3, 6, and 7, are available at the MPA-Garching archive.<sup>4</sup>

### 2.3.1. $9-13 M_{\odot}$

The 17 models in this mass range,  $9.0-13.0 M_{\odot}$ , in intervals of  $0.25 M_{\odot}$ , are based on the recent study of Woosley & Heger (2015). They use the same stellar physics, especially for the propagation of convectively bounded oxygen- and silicon-burning flames, as in that work (see also Timmes et al. 1994), but differ by carrying a much larger network throughout the whole evolution. They are new models.

Stars from  $9.0$  to  $10.25 M_{\odot}$  ignite silicon in a strong flash that, for the  $10.0$  and  $10.25 M_{\odot}$  models, could be violent enough to eject the hydrogen envelope and helium shell prior to iron-core collapse. What actually happens is uncertain, though, and depends on how much silicon burns in the flash (Woosley & Heger 2015). For the present study, silicon burning in the flash was constrained to be small by using a small convective transport coefficient, and envelope ejection did not occur. For models  $10.5 M_{\odot}$  and heavier, all fuels ignited stably in the center of the star.

The nuclear reaction network used was complete up to Bi ( $Z=93$ ) and contained roughly 1000 isotopes during helium burning and over 1200 during oxygen and silicon burning. Pre-SN stars contained approximately 1900 isotopes. Woosley & Heger (2015), who were interested chiefly in stellar structure and not nucleosynthesis, truncated their network at Ge. The extra nuclei included here allowed a better representation of the *s*-process in the pre-SN star and its modification during the explosion, but did not greatly alter the structure.

### 2.3.2. $13.1-30 M_{\odot}$

Models in this mass range were calculated using the same nuclear and stellar physics as in Woosley & Heger (2007). The survey includes 151 models from  $15$  to  $30 M_{\odot}$  taken from the “S-series” in Sukhbold & Woosley (2014) and 19 additional models from  $13.1$  to  $14.9 M_{\odot}$  calculated the same way. In order to demonstrate the agreement among models from two different surveys, several additional models from  $12$  to  $13 M_{\odot}$  were calculated for comparison with models from Section 2.3.1, but

<sup>4</sup> <http://doi.org/10.17617/1.b>

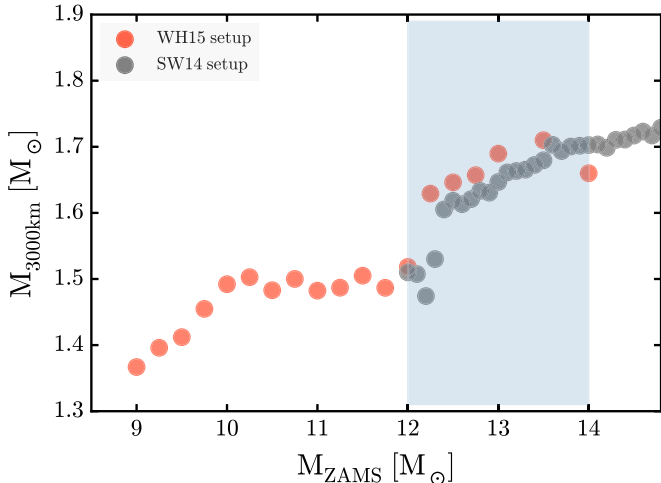


**Figure 4.** Pre-SN core mass inside of 3000 km shown for the 17 new models (see also Woosley & Heger 2015) up to  $13.0 M_{\odot}$ , along with the 19 new models down to  $13.1 M_{\odot}$  calculated with the same input physics as in Sukhbold & Woosley (2014). Though the models come from different studies, they are in good agreement. Several models between  $12$  and  $14 M_{\odot}$  were calculated both ways to highlight the agreement (gray region).

were not used in the survey. The pre-SN structures of stars calculated both ways were in good agreement, having, e.g., nearly identical values of the mass enclosed by the inner 3000 km (Figure 4).

The mesh of stellar masses was relatively fine,  $0.1 M_{\odot}$ , as is necessary to calculate the rich variation of stellar structure in this mass range.

### 2.3.3. 31–120 $M_{\odot}$

A total of 13 models with varying mass increments were studied in this range—31, 32, 33, 35, 40, 45, 50, 55, 60, 70, 80, 100, 120  $M_{\odot}$ —all coming from Woosley & Heger (2007). Starting at about  $40 M_{\odot}$ , these models lost their entire envelopes and ended their lives as Wolf-Rayet stars. The final masses are thus sensitive to the treatment of mass loss for both red supergiant stars and stripped cores. The final pre-SN masses for the 60, 70, 80, 100, and  $120 M_{\odot}$  stars were 7.29, 6.41, 6.37, 6.04, and  $6.16 M_{\odot}$ , respectively. Some additional properties of all the pre-SN models are given in Table 2.

## 3. EXPLOSION MODELING

The pre-SN models were exploded using two different one-dimensional hydrodynamics codes, Prometheus-Hot Bubble (henceforth P-HOTB; Janka & Müller 1996; Kifonidis et al. 2003) and KEPLER. For central engines Z9.6, W18, and N20, all models were exploded using both codes. For W15, W20, and S19.8, models were exploded only with P-HOTB. All of our explosion results from the P-HOTB calculations are included in the electronic edition in a tar.gz package.

P-HOTB includes the necessary neutrino and high-density physics to follow iron-core collapse and neutrino energy and lepton-number transport. It also carries a small reaction network with 14 alpha nuclei (Müller 1986), which is capable of tracking bulk nucleosynthesis (Ugliano et al. 2012; Ertl et al. 2015). The neutrino transport is approximated by a fast, gray scheme that solves the coupled set of neutrino number and energy equations for all flavors as described in Scheck et al. (2006). The implementation of gravity, including general

**Table 2**  
Progenitor Data

$M_i (M_{\odot})$	$M_f (M_{\odot})$	$M_{\alpha} (M_{\odot})$	$M_{CO} (M_{\odot})$	$\log(R_f)$ (cm)
9.0	8.746	1.571	1.402	13.46
9.25	8.978	1.783	1.452	13.45
9.5	9.208	2.041	1.501	13.46
9.75	9.445	2.305	1.555	13.49
10.0	9.675	2.476	1.608	13.55
10.25	9.927	2.590	1.648	13.58
10.5	10.194	2.672	1.689	13.58
10.75	10.440	2.752	1.741	13.59
11.0	10.688	2.819	1.781	13.60
11.25	10.889	2.842	1.793	13.60
11.5	10.754	2.806	1.781	13.60
11.75	10.775	2.999	1.910	13.63
12.0	10.902	3.116	2.086	13.65
12.25	11.083	3.220	2.166	13.66
12.5	11.188	3.342	2.254	13.68
12.75	11.404	3.418	2.332	13.68
13.0	11.567	3.516	2.416	13.69
13.1	11.469	3.636	2.496	13.71
13.2	11.538	3.660	2.515	13.71
13.3	11.703	3.656	2.509	13.70
13.4	11.733	3.708	2.566	13.71
13.5	11.777	3.762	2.610	13.72
13.6	11.766	3.824	2.654	13.73
13.7	11.885	3.835	2.680	13.73
13.8	11.864	3.905	2.726	13.73
13.9	12.124	3.876	2.707	13.73
14.0	12.079	3.950	2.765	13.74
14.1	12.084	4.012	2.831	13.74
14.2	12.315	3.994	2.805	13.74
14.3	12.347	4.038	2.864	13.74
14.4	12.384	4.082	2.904	13.75
14.5	12.201	4.196	3.006	13.76
14.6	12.599	4.131	2.952	13.75
14.7	12.531	4.214	2.999	13.76
14.8	12.780	4.200	3.013	13.75
14.9	12.894	4.223	3.040	13.76
15.0	12.603	4.352	3.144	13.77
15.1	12.933	4.328	3.130	13.76
15.2	12.584	4.459	3.257	13.78
15.3	13.121	4.378	3.193	13.76
15.4	13.226	4.419	3.221	13.77
15.5	13.279	4.451	3.227	13.77
15.6	13.230	4.518	3.292	13.77
15.7	13.187	4.579	3.342	13.78
15.8	13.414	4.579	3.378	13.78
15.9	13.563	4.600	3.370	13.78
16.0	13.145	4.749	3.510	13.79
16.1	13.741	4.672	3.435	13.78
16.2	13.551	4.765	3.524	13.79
16.3	13.861	4.756	3.538	13.78
16.4	13.974	4.787	3.552	13.79
16.5	13.992	4.827	3.581	13.79
16.6	13.863	4.904	3.657	13.79
16.7	14.067	4.915	3.679	13.79
16.8	14.190	4.942	3.701	13.79
16.9	14.244	4.983	3.739	13.80
17.0	14.301	5.018	3.801	13.80
17.1	14.362	5.058	3.831	13.80
17.2	14.348	5.107	3.853	13.80
17.3	14.514	5.141	3.900	13.81
17.4	14.297	5.216	3.955	13.82
17.5	14.573	5.220	3.978	13.81
17.6	14.689	5.254	4.000	13.82
17.7	14.654	5.308	4.056	13.83

**Table 2**  
(Continued)

$M_i (M_\odot)$	$M_f (M_\odot)$	$M_\alpha (M_\odot)$	$M_{CO} (M_\odot)$	$\log(R_f) (\text{cm})$
17.8	14.794	5.338	4.087	13.83
17.9	14.882	5.372	4.135	13.83
18.0	14.936	5.401	4.176	13.83
18.1	15.065	5.441	4.200	13.83
18.2	15.024	5.485	4.223	13.84
18.3	15.156	5.527	4.301	13.84
18.4	15.151	5.566	4.315	13.84
18.5	14.943	5.651	4.385	13.85
18.6	15.247	5.654	4.409	13.84
18.7	15.289	5.684	4.414	13.84
18.8	14.977	5.799	4.522	13.85
18.9	15.042	5.838	4.555	13.86
19.0	15.503	5.804	4.541	13.85
19.1	15.576	5.838	4.584	13.85
19.2	15.545	5.884	4.608	13.86
19.3	15.536	5.929	4.642	13.86
19.4	15.537	5.975	4.715	13.86
19.5	15.670	6.002	4.710	13.86
19.6	15.650	6.051	4.773	13.87
19.7	15.757	6.087	4.817	13.87
19.8	15.851	6.123	4.851	13.87
19.9	15.857	6.169	4.886	13.87
20.0	15.848	6.207	4.970	13.87
20.1	15.900	6.256	4.955	13.87
20.2	15.835	6.292	5.020	13.87
20.3	16.057	6.316	5.035	13.87
20.4	15.935	6.376	5.101	13.88
20.5	16.093	6.402	5.126	13.87
20.6	15.660	6.533	5.243	13.89
20.7	15.941	6.505	5.217	13.89
20.8	16.017	6.539	5.232	13.89
20.9	16.232	6.558	5.288	13.89
21.0	16.119	6.617	5.335	13.89
21.1	16.183	6.651	5.360	13.89
21.2	16.372	6.682	5.373	13.90
21.3	16.306	6.720	5.436	13.90
21.4	16.163	6.772	5.475	13.90
21.5	16.044	6.842	5.537	13.91
21.6	16.331	6.848	5.565	13.90
21.7	16.390	6.880	5.630	13.91
21.8	16.336	6.924	5.629	13.91
21.9	16.514	6.969	5.708	13.91
22.0	16.218	7.026	5.776	13.91
22.1	16.297	7.045	5.786	13.92
22.2	16.520	7.091	5.839	13.92
22.3	16.368	7.142	5.892	13.92
22.4	16.385	7.174	5.932	13.92
22.5	16.364	7.201	5.959	13.93
22.6	16.489	7.252	6.012	13.93
22.7	16.386	7.307	6.066	13.93
22.8	16.260	7.330	6.093	13.94
22.9	16.433	7.385	6.147	13.94
23.0	16.468	7.419	6.174	13.94
23.1	16.464	7.450	6.215	13.94
23.2	16.444	7.497	6.269	13.95
23.3	16.533	7.525	6.282	13.95
23.4	16.475	7.594	6.351	13.95
23.5	16.564	7.626	6.379	13.95
23.6	16.131	7.668	6.420	13.96
23.7	16.274	7.720	6.475	13.96
23.8	16.053	7.788	6.546	13.96
23.9	16.460	7.799	6.573	13.96
24.0	16.062	7.848	6.601	13.96
24.1	16.366	7.853	6.614	13.96

**Table 2**  
(Continued)

$M_i (M_\odot)$	$M_f (M_\odot)$	$M_\alpha (M_\odot)$	$M_{CO} (M_\odot)$	$\log(R_f) (\text{cm})$
24.2	15.236	8.077	6.830	13.98
24.3	16.357	7.951	6.712	13.97
24.4	15.981	8.018	6.769	13.97
24.5	15.988	8.038	6.782	13.97
24.6	15.967	8.101	6.869	13.98
24.7	15.743	8.152	6.897	13.98
24.8	16.215	8.161	6.910	13.98
24.9	16.121	8.165	6.908	13.98
25.0	15.849	8.251	7.011	13.99
25.1	15.827	8.302	7.039	13.99
25.2	15.076	8.414	7.127	13.99
25.3	16.264	8.355	7.080	13.99
25.4	15.621	8.432	7.169	13.99
25.5	15.445	8.460	7.197	13.99
25.6	15.599	8.525	7.256	14.00
25.7	15.867	8.569	7.315	14.00
25.8	15.954	8.572	7.312	14.00
25.9	15.461	8.649	7.387	14.00
26.0	15.462	8.688	7.385	14.00
26.1	15.473	8.723	7.460	14.00
26.2	15.400	8.775	7.489	14.01
26.3	15.276	8.826	7.549	14.00
26.4	15.147	8.886	7.593	14.01
26.5	15.616	8.896	7.638	14.01
26.6	15.317	8.959	7.683	14.01
26.7	15.073	8.988	7.712	14.01
26.8	15.268	9.027	7.757	14.02
26.9	15.449	9.031	7.770	14.01
27.0	15.397	9.159	7.896	14.02
27.1	15.133	9.170	7.909	14.02
27.2	15.281	9.184	7.921	14.02
27.3	15.068	9.238	7.983	14.02
27.4	15.019	9.316	8.029	14.02
27.5	15.008	9.306	8.058	14.02
27.6	14.862	9.392	8.137	14.02
27.7	14.831	9.443	8.183	14.03
27.8	14.846	9.493	8.263	14.03
27.9	15.169	9.441	8.226	14.03
28.0	15.120	9.521	8.289	14.03
28.1	14.747	9.599	8.352	14.03
28.2	14.561	9.655	8.399	14.03
28.3	14.532	9.668	8.412	14.03
28.4	14.235	9.776	8.527	14.03
28.5	14.578	9.697	8.456	14.03
28.6	14.310	9.794	8.535	14.03
28.7	14.363	9.838	8.582	14.03
28.8	14.442	9.908	8.664	14.03
28.9	14.292	9.941	8.694	14.03
29.0	15.087	9.867	8.662	14.03
29.1	14.264	10.013	8.807	14.04
29.2	14.609	10.021	8.802	14.03
29.3	14.181	10.080	8.849	14.03
29.4	14.030	10.138	8.897	14.03
29.5	13.674	10.195	8.963	14.03
29.6	14.094	10.215	8.976	14.03
29.7	14.113	10.264	9.024	14.04
29.8	13.803	10.278	9.036	14.03
29.9	13.882	10.379	8.277	14.03
30.0	13.805	10.359	9.101	14.03
31	13.634	10.821	9.611	14.01
32	13.414	11.270	10.070	13.99
33	13.239	11.599	10.396	13.96
35	13.663	12.561	11.426	12.16
40	15.336	14.682	13.581	11.91

**Table 2**  
(Continued)

$M_i (M_\odot)$	$M_f (M_\odot)$	$M_\alpha (M_\odot)$	$M_{CO} (M_\odot)$	$\log(R_f)$ (cm)
45	13.018	13.018	13.018	10.83
50	9.817	9.817	9.817	11.58
55	9.380	9.380	9.380	11.72
60	7.289	7.289	7.289	10.49
70	6.408	6.408	6.408	10.63
80	6.368	6.368	6.368	10.62
100	6.036	6.036	6.036	10.58
120	6.160	6.160	6.160	11.55

**Note.**  $M_i$  is the ZAMS mass,  $M_f$  is the final pre-SN mass, and  $R_f$  is the corresponding final radius. He and CO core masses have been measured using 20% mass fraction point  $X(\text{H}) \leq 0.2$  for  $M_\alpha$  and  $X(\text{He}) \leq 0.2$  for  $M_{CO}$ .

relativistic corrections, has been detailed in Arcones et al. (2007), and the choice of the boundary conditions for hydrodynamics and transport applied in our present work follows Ugliano et al. (2012) and Ertl et al. (2015). Extending the code used by Ugliano et al. (2012), Ertl et al. (2015) added a simple deleptonization scheme (Liebendörfer 2005) for a fast treatment of the core-collapse phase until shortly after core bounce. They also improved the microphysics treatment in several respects, e.g., by implementing a high-density EOS and consistently coupling the burning network with the low-density EOS and hydrodynamics.

KEPLER does not include neutrino transport, and its EOS becomes unreliable above about  $10^{11} \text{ g cm}^{-3}$ , but it does carry a much larger nuclear reaction network of roughly 1500 isotopes, capable of calculating detailed nucleosynthesis, and includes flux-limited radiative diffusion so that bolometric light curves can be determined. For cases where both codes were used, the procedure that was followed was to first calculate the explosion using P-HOTB, continued to a sufficiently late time to determine the remnant mass, and then to post-process the explosion using KEPLER.

### 3.1. Explosion Simulations with P-HOTB

#### 3.1.1. Modeling Methodology

A detailed discussion of our methodology for neutrino-driven explosions for large sets of progenitor models can be found in Ertl et al. (2015), and more technical information is also given in Ugliano et al. (2012). Here we summarize the essential characteristics.

The calculations with P-HOTB assume spherical symmetry and are 1D. They follow the evolution from the onset of stellar collapse as determined by the KEPLER code, when the collapse speed anywhere in the core first exceeds  $1000 \text{ km s}^{-1}$ , through core bounce and post-bounce accretion to either BH formation or successful explosion. The fallback of matter that does not become gravitationally unbound in the explosion is determined by running the calculation for days to weeks. PNS cooling and neutrino emission are followed for typically 15 s, at which time the shock has crossed  $\sim 10^{10} \text{ cm}$  and is outside of the CO core. By that time the power of the neutrino-driven wind, which pushes the dense ejecta shell enclosed by the expanding SN shock and the wind-termination shock, has decayed to a dynamically insignificant level. The models are then mapped to a grid extending to larger radii, and the inner

boundary is moved from below the neutrinosphere to  $10^9 \text{ cm}$  in order to ease the numerical time-step constraint.

Spherically symmetric, first-principles simulations do not yield explosions by the neutrino-driven mechanism except for low-mass progenitors with oxygen–neon–magnesium cores (Kitaura et al. 2006; Janka et al. 2008) or small iron cores (Melson et al. 2015). These stars are characterized by an extremely dilute circum-core density and small compactness values,  $\xi_M$ , for  $M \geq 1.5$ . Ignoring the beneficial effects of hydrodynamic instabilities in initiating the revival of the stalled bounce shock, explosions require a suitable tuning of the neutrino source to revive the shock by neutrino heating.

In order to do so, we exclude the inner  $1.1 M_\odot$  of the high-density core of the PNS at densities significantly above the neutrinospheric region from the hydrodynamical modeling, and we replace them by an inner grid boundary that is contracted to mimic the shrinking of the core. At this domain boundary, time-dependent neutrino luminosities and mean energies (Scheck et al. 2006; Arcones et al. 2007; Ugliano et al. 2012) are imposed. Outside of this boundary (between neutrino optical depths below  $\sim 10$ , initially, and up to several thousand after seconds of PNS cooling), the lepton-number and energy transport of all species of neutrinos is solved using a fast, analytical, gray transport approximation (Scheck et al. 2006). The time-dependent neutrino emission from PNS accretion, which is determined by the progenitor structure of the collapsing star and by the dynamics of the shock front, is thus included in our models and ensures that corresponding feedback effects are taken into account, at least as far as they can be represented in spherical symmetry.

The excised PNS core is represented as a time-dependent neutrino source using a simple one-zone model whose behavior is determined by applying fundamental physics relations (Ugliano et al. 2012). The free parameters of this core model are calibrated by comparing the results of explosion simulations for suitable progenitor models to observations of well-studied SNe. For this purpose we consider important diagnostic parameters of the explosion, i.e., the explosion energy and the mass of  $^{56}\text{Ni}$  produced, as well as important properties of the PNS as a neutrino source, i.e., the total release of neutrino energy and the timescale of this neutrino emission. For the neutrino properties, the detected neutrino signal from SN 1987A is used as a benchmark, but we also make sure that the neutrino-energy loss of our PNS models is consistent with binding energies of neutron stars based on microphysical EOSs.

Excluding the high-density core of the PNS from direct modeling can be justified by the still incomplete knowledge of the EOS in the supernuclear regime and significant uncertainties in the neutrino opacities in dense, correlated nuclear matter, which overshadow all fully self-consistent modeling. Of course, modeling SN explosions in spherical symmetry can only be an intermediate step, and ultimately three-dimensional (3D) simulations will be needed. Below we will argue that 1D simulations in the case of tuned explosions exhibit some aspects that are more similar to current 3D models than two-dimensional (2D) simulations. According to current multi-dimensional calculations, the onset of the explosion differs between 2D and 3D, with the former favoring earlier explosions because of differences in the behavior of turbulence in the post-shock region (e.g., Hanke et al. 2012; Couch 2013). Moreover, the imposed constraint of axisymmetry in 2D leads

to artificial explosion geometries with pronounced axis features. Also the long-time phase of simultaneous accretion and ejection of neutrino-heated matter seems to differ considerably between 2D and 3D (Müller 2015), which can lead to more energetic explosions in 3D (Melson et al. 2015; Müller 2015).

In the following, we present essential information on how the PNS is described as a neutrino source in our simulations and how the calibration of this neutrino source is done by referring to observational data. Since results of nearly the same set of pre-SN models using P-HOTB have been recently discussed by Ertl et al. (2015), our description here can be terse and focused mainly on newly introduced aspects.

### 3.1.2. The PNS as Neutrino Source

The central  $1.1 M_{\odot}$  core of the PNS resulting from the collapse of each pre-SN star is excised from the computational volume and replaced by a contracting inner grid boundary a few milliseconds after core bounce, shortly after the expanding shock has converted to a stalled accretion shock at an enclosed mass of more than  $1.1 M_{\odot}$ . For the hydrodynamics we apply the conditions that are needed to maintain hydrostatic equilibrium at this Lagrangian grid boundary (Janka & Müller 1996). The shrinking of the cooling and deleptonizing PNS is mimicked by the contraction of the inner grid boundary,  $R_{\text{ib}}$ , which is described by an exponential function (Equation (1) in Arcones et al. 2007) with the parameter values given in Section 2 of Ugliano et al. (2012). In order to avoid too severe timestep restrictions that could hamper the tracking of the combined evolution of PNS and ejecta over more than 20 s, we choose the case of “standard” instead of “rapid” contraction shown in Figure 1 of Scheck et al. (2006). This may lead to an underestimation of the accretion luminosity and of the gradual hardening of the radiated neutrino spectra compared to self-consistent SN simulations, but in our approach this can be well compensated by a corresponding adjustment of the calibration of the inner core as a neutrino source. Since the accretion luminosity computed by the transport adds to core luminosity imposed at the inner grid boundary, the calibration sets constraints to the combined value of these two contributions.

As detailed in Ugliano et al. (2012), we describe the high-density PNS core of mass  $M_c = 1.1 M_{\odot}$  by a simple one-zone model under the constraints of energy conservation and the virial theorem including the effects associated with the growing pressure of the accretion layer, whose accumulation around the PNS core is followed by our hydrodynamic simulations. The one-zone core model provides a time-dependent total core-neutrino luminosity,  $L_{\nu,c}(t)$ , which determines the boundary luminosity imposed at the inner grid boundary (at  $R_{\text{ib}}$ ) of the computational grid, suitably split between  $\nu_e$ ,  $\bar{\nu}_e$ , and heavy-lepton neutrinos (see Ugliano et al. 2012; Scheck et al. 2006). Besides the luminosities of the different neutrino species, also the mean energies (or spectral temperatures) of the inflowing neutrinos are prescribed at  $R_{\text{ib}}$  (see Ugliano et al. 2012).

The total core-neutrino luminosity  $L_{\nu,c}(t)$  is determined by the core mass,  $M_c$ , the core radius,  $R_c(t)$ , the rate of contraction of this radius,  $\dot{R}_c(t)$ , the mass of the PNS accretion mantle around the core,  $m_{\text{acc}}$  (taken to be the mass between the inner grid boundary and a lower density of  $10^{10} \text{ g cm}^{-3}$ ), and the mass accretion rate of the PNS,  $\dot{m}_{\text{acc}}$ , as computed in our hydrodynamical runs. Equation (4) of Ugliano et al. (2012) for

the core luminosity can be rewritten as

$$L_{\nu,c}(t) = \frac{1}{3(\Gamma - 1)} \left[ (3\Gamma - 4)(E_g + S) \frac{\dot{R}_c}{R_c} + S \frac{\dot{m}_{\text{acc}}}{m_{\text{acc}}} \right], \quad (2)$$

with the factors

$$E_g + S = -\frac{2}{5} \frac{GM_c}{R_c} \left( M_c + \frac{5}{2} \zeta m_{\text{acc}} \right), \quad (3)$$

$$S = -\zeta \frac{GM_c m_{\text{acc}}}{R_c}, \quad (4)$$

and with the adiabatic index  $\Gamma$  and coefficient  $\zeta (= \mathcal{O}(1))$  being free parameters of the model. We note that through the  $S$ -dependent terms the PNS core luminosity depends on the structure (e.g., compactness) of the progenitor star, which determines the mass accretion rate  $\dot{m}_{\text{acc}}$  and thus the mass  $m_{\text{acc}}$  of the accretion mantle of the PNS. The core radius as a function of time is prescribed by

$$R_c(t) = R_{c,f} + \frac{R_{c,i} - R_{c,f}}{(1+t)^n}, \quad (5)$$

where the time  $t$  is measured in seconds. The initial PNS core radius,  $R_{c,i}$ , is set equal to the initial radius of the inner boundary of the hydrodynamic grid,  $R_{\text{ib}}^i$ , and the final PNS core radius,  $R_{c,f}$ , and the exponent  $n$  are also free parameters of our model. Note that  $R_c$  should be considered as a representative radius of the high-density core. Since we grossly simplify the radial structure of the PNS core by a one-zone description, the numerical value of  $R_c$  has no exact physical meaning except that it represents a rough measure of the size of the PNS core. However, neither its time evolution nor its final value need to be equal to the inner boundary radius of the hydrodynamic grid or to the radius of the  $1.1 M_{\odot}$  core of a self-consistently computed PNS model using a nuclear EOS. Nevertheless, with a suitably chosen (calibrated) time dependence of  $R_c$ , our model is able to reproduce basic features of the neutrino emission of cooling PNSs, and the choice of  $n$  and  $R_{c,f}$  can be guided by the temporal behavior of  $R_c(t)$  in sophisticated PNS cooling calculations (see below).

Since both of the expressions of Equations (3) and (4) are negative and  $\dot{R}_c < 0$  and  $\dot{m}_{\text{acc}} > 0$  for the contracting and accreting PNS, respectively, the first term in the brackets on the right-hand side of Equation (2) is positive, while the second term is negative. The former term represents the gravitational binding energy release as a consequence of the PNS core settling in the gravitational potential, including the compressional work delivered by the surrounding accretion layer. In contrast, the latter (negative) term accounts for the additional internal energy (and pressure) of the core that is needed for gravitational stability when the overlying mantle grows in mass. This second term thus reduces the energy that can be radiated in neutrinos.

### 3.1.3. Calibration to SN 1987A and SN 1054

The four free parameters of the PNS core model,  $\Gamma$ ,  $\zeta$ ,  $n$ , and  $R_{c,f}$ , determine the core-neutrino emission as given by Equation (2) and thus the solution to a given SN explosion. The observational cases that serve our needs for calibrating these free parameters are SN 1987A for high-mass stars and the

**Table 3**  
PNS Core Model Parameters in P-HOTB

Model	$R_{\text{c,f}}$ (km)	$\Gamma$	$\zeta$	$n$	$E_{51}$	$M(^{56}\text{Ni} + 1/2 \text{Tr})$
Z9.6	7.0	3.0	0.65	1.55	0.16	0.0087
S19.8	6.5	3.0	0.90	2.96	1.30	0.089
W15	6.0	3.0	0.60	3.10	1.41	0.068
W18	6.0	3.0	0.65	3.06	1.25	0.074
W20	6.0	3.0	0.70	2.84	1.24	0.076
N20	6.0	3.0	0.60	3.23	1.49	0.062

Crab SN, SN 1054, for low-mass stars. The progenitors and explosion properties of these SNe are distinctly different and require different values for our model parameters, as we shall argue below. For both SN 1987A and SN 1054 the explosion energy and  $^{56}\text{Ni}$  mass are fairly well determined and reasonably good guesses for the progenitors exist.

For the SN 1987A progenitor, Ertl et al. (2015) considered five different 15–20  $M_{\odot}$  models, W18, N20, S19.8, W15, and W20. The parameter values that were found to approximately reproduce the known explosion energy and  $^{56}\text{Ni}$  production of SN 1987A,  $(1.3\text{--}1.5) \times 10^{51}$  erg and  $0.0723\text{--}0.0772 M_{\odot}$ , respectively (Utrobin 2005; Utrobin & Chugai 2011; Utrobin et al. 2014), are given in Table 3. In the table,  $E_{51}$  is the explosion energy in units of  $10^{51}$  erg = 1 B = 1 bethe, and  $M(^{56}\text{Ni} + 1/2 \text{Tr})$  is the mass of shock-produced  $^{56}\text{Ni}$  plus one-half of the iron-group species in the neutrino-powered wind. Because  $Y_e$  in the wind is not precisely determined, the actual  $^{56}\text{Ni}$  synthesis is between  $M(^{56}\text{Ni})$  and  $M(^{56}\text{Ni} + \text{Tr})$  (Ertl et al. 2015). In practice,  $\Gamma$  and for most cases  $R_{\text{c,f}}$  are held constant ( $\Gamma = 3$  and  $R_{\text{c,f}} = 6.0$  km), while  $n$  and  $\zeta$  are adjusted in an iterative process.

Once the parameter values of the PNS core model are determined for a given SN 1987A progenitor, that same core history is used in all the other pre-SN stars of different masses. In this way a set of SNe calibrated to a given SN 1987A progenitor is generated. This set of explosions is named according to the calibration model, so we have the “W18 series,” the “N20 series,” etc. In this paper we mainly focus on the sets of explosions for the W18 and N20 calibrations.

A problematic point in the results of Ugliano et al. (2012) was an overestimation of the explosion energies for lower-mass SNe. Because of the calibration of the PNS core parameters with SN 1987A models, a high core-neutrino luminosity caused a strong neutrino-driven wind for low-mass neutron stars. This led to explosion energies in excess of 1.5 B for most stars between 10 and 15  $M_{\odot}$ . In particular, for progenitors below  $\sim 12 M_{\odot}$  such high energies are, on the one hand, not compatible with recent self-consistent 2D and 3D models of the explosion, which obtain much lower explosion energies in the range of  $\lesssim 0.1$  B to at most a few 0.1 B for progenitors from  $\sim 8.8 M_{\odot}$  to  $\sim 12 M_{\odot}$  with oxygen-neon-magnesium or iron cores (Kitaura et al. 2006; Janka et al. 2008, 2012; Melson et al. 2015; Müller 2015). Given the relatively dilute layers and steep density gradients that surround the cores of these progenitors, the hydrodynamic explosion models also suggest that it will be very difficult to reach higher energies by the neutrino-driven mechanism and our present knowledge of the involved physics. On the other hand, high explosion energies for low-mass progenitors are also disfavored by observations, which seem to suggest some correlation between the progenitor (or ejecta) mass and the explosion energy (e.g., Poznanski

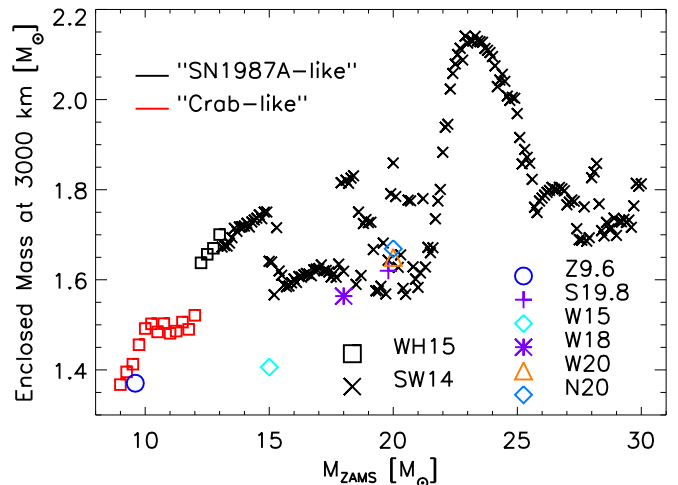


**Figure 5.** Mass inside a radius of 3000 km for all progenitors up to  $30 M_{\odot}$  at the time when the central density reaches the same value of  $3 \times 10^{10} \text{ g cm}^{-3}$ . The black crosses and squares indicate “SN 1987-like” cases; the red squares, “Crab-like” ones. Squares are models similar to Woosley & Heger (2015); crosses, those of the Sukhbold & Woosley (2014) progenitor set. The locations of the calibration models are indicated by colored symbols as indicated in the figure legend. While N20, W20, and S19.8 cluster closely, W15 lies far off because this model has a very small compactness,  $\xi_{1.75}$  (see Ertl et al. 2015).

2013; Chugai & Utrobin 2014), although the correlation appears weakened in light of a more detailed statistical analysis (Pejcha & Prieto 2015).

Ertl et al. (2015) applied a “quick fix” to cure the problem of overenergetic low-mass explosions by using a linear scaling of the compression parameter  $\zeta$  of the PNS core model, coupled to the decreasing compactness  $\xi_{1.75}$  for progenitors with  $M \leq 13.5 M_{\odot}$ . Here we elaborate on the background of this measure and introduce an alternative, similarly effective but physics-wise more transparent approach than the  $\zeta$  modification.

Figure 5 displays the mass inside of a radius of 3000 km for all considered progenitor stars up to  $30 M_{\odot}$  at the onset of core collapse. For most appropriate comparison we evolved all models until they had contracted to the same central density of  $3 \times 10^{10} \text{ g cm}^{-3}$ . The low-mass stars with  $M \leq 12.0 M_{\odot}$  are clearly separated from the more massive progenitors by smaller enclosed masses  $M_{3000} = m(r \leq 3000 \text{ km})$ . Since the Crab remnant is thought to have originated from the explosion of a star in the  $\sim 9\text{--}10 M_{\odot}$  range (e.g., Nomoto et al. 1982; Nomoto 1987; Smith 2013; Tominaga et al. 2013), we call the models with small  $M_{3000}$  “Crab-like,” whereas we consider the progenitors with  $M > 12.0 M_{\odot}$  and considerably larger values of  $M_{3000}$  as “SN 1987A-like.” Our calibration models for SN 1987A possess  $M_{3000}$  cores that join with the SN 1987A-like cases (see in Figure 5 the purple star and blue diamond for the W18 and N20 progenitors, respectively, and the colored symbols for the other calibration models).

Since the value of  $M_{3000}$  provides the mass that is located within 3000 km from the center, it correlates with the mass of the PNS that forms in the collapse of the stellar core. It is important to realize that the contraction behavior and final radius of the innermost  $1.1 M_{\odot}$  (which we describe here by our analytic one-zone model) depend in a microphysical model on the mass of the newly formed NS. This is shown in Figure 6, where we plot the time evolution of the  $1.1 M_{\odot}$  cores for two self-consistent PNS cooling simulations with all relevant microphysics (Mirizzi et al. 2015), carried out with the nuclear

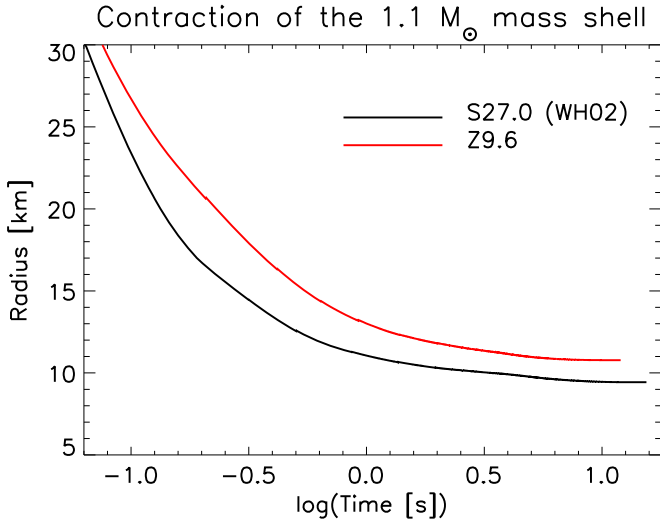


**Figure 6.** Radius of the  $1.1 M_{\odot}$  core as a function of post-bounce time for a low-mass neutron star (baryonic mass  $1.36 M_{\odot}$ ; gravitational mass  $1.25 M_{\odot}$ ) characteristic of the Z9.6 progenitor (red line), and for a high-mass neutron star (baryonic mass  $1.78 M_{\odot}$ ; gravitational mass  $1.59 M_{\odot}$ ) characteristic of a  $27 M_{\odot}$  progenitor (black line). Both cores were evolved in a self-consistent PNS cooling simulation with detailed neutrino transport and the LS220 high-density EOS of Lattimer & Swesty (1991). The same simulations were recently reported by Mirizzi et al. (2015). The different contraction behavior of the high-density cores of low-mass and high-mass PNSs is obvious.

EOS of Lattimer & Swesty (1991). The slower and less extreme contraction in the case of the low-mass PNS compared to the high-mass PNS suggests that less neutrino energy is more gradually released in the low-mass case. This difference needs to be taken into account when modeling the explosions of the low-mass progenitor stars of our “Crab-like” sample in order to avoid the overestimation of the explosion energy in this subset of the progenitors.

Because the simple one-zone core model does not allow us to just adopt the core-radius evolution from a self-consistent simulation, we calibrate the “Crab-like” explosions by reproducing the observationally inferred explosion energy of SN 1054 ( $\sim 0.05$ – $0.15$  B; Smith 2013; Tominaga et al. 2013; Yang & Chevalier 2015) and  $^{56}\text{Ni}$  mass ( $\lesssim 10^{-2} M_{\odot}$ ; Smith 2013; Tominaga et al. 2013) with a suitable progenitor model.

Table 3 lists the parameter values obtained in our Crab calibration of the Z9.6 model. We again use  $\Gamma = 3.0$  and  $\zeta = 0.65$  as in the W18 series, but now employ a reduced value of  $n = 1.55$  and a larger value of  $R_{\text{c,f}} = 7 \text{ km}$ , because these values describe a slower contraction of the PNS core to a larger final radius (see Equation (5)) as found for a low-mass PNS in the self-consistent PNS cooling simulation (Figure 6).

Since model Z9.6 for the Crab progenitor is in the extreme corner of the Crab-like sample in terms of mass and  $M_{3000}$  (see the blue circle in Figure 5) and the PNS masses in this sample vary considerably (see Figures 8 and 9), we determine the values of  $n$  and  $R_{\text{c,f}}$  for the other Crab-like progenitors (with masses  $M$ ) by interpolating as function of  $M_{3000}$  between the Crab model and the SN1987A-like progenitor with the smallest value of  $M_{3000}$ , which is the case at  $15.2 M_{\odot}$  in Figure 5, model SW14-15.2. On the SN 1987A-like side we use here the SN 1987A calibration values of  $n$  and  $R_{\text{c,f}}$  for the W18 series.

Our interpolation functions for  $y \equiv n, R_{\text{c,f}}$  therefore are

$$y(x) = y_0 + \frac{y_1 - y_0}{x_1 - x_0}(x - x_0), \quad (6)$$

with  $x = M_{3000}(M)$ ,  $x_0 = M_{3000}(\text{Z9.6})$ ,  $x_1 = M_{3000}(\text{SW14-15.2})$ ,  $y(x) = X[M_{3000}(M)]$ ,  $y_0 = X[M_{3000}(\text{Z9.6})]$ , and  $y_1 = X[M_{3000}(\text{SW14-15.2})]$ . For all SN 1987A-like progenitors, we still apply the same values of the model parameters as obtained for the SN 1987A calibration of each series and listed in Table 3.

For the  $9.0 M_{\odot}$  progenitor, which has a lower mass  $M_{3000}$  than Z9.6, we use the same values of all core model parameters as for the  $9.6 M_{\odot}$  case. Although we employ Z9.6 as our template case for Crab and can also refer to a recent 3D explosion simulation of this model (Melson et al. 2015) for its parameter calibration, our  $9.0 M_{\odot}$  explosion is equally well compatible with Crab. The computed properties of this explosion (energy around 0.1 B and  $^{56}\text{Ni}$  mass below  $0.01 M_{\odot}$ ; see following section) turn out to be fully consistent with the observational limits for Crab.

### 3.1.4. Explosion Results with P-HOTB

The basic explosion properties of all SN 1987A calibration models considered here can be found in Table 1 of Ertl et al. (2015). Figure 7 shows the evolution toward explosion for our calibration models Z9.6, W18, and N20. The shock radius and characteristic mass trajectories, as well as neutrino luminosities and mean neutrino energies, are given in the upper panels, and the different contributions to the ejecta energy are given in the lower panels.

The expansion of the shock radius in model Z9.6 reproduces the results of multidimensional simulations (Melson et al. 2015) fairly well, and the diagnostic explosion energy also reaches  $\sim 0.1$  B after roughly  $0.5$  s to asymptote to a final energy of about  $0.16$  B after several seconds. This energy is in the upper range of estimates for SN 1054 but still compatible with them (Smith 2013; Tominaga et al. 2013; Yang & Chevalier 2015). Also the luminosities and mean energies of electron neutrinos ( $\nu_e$ ) and antineutrinos ( $\bar{\nu}_e$ ), which are the crucial agents for driving and powering the explosions, are in the ballpark of results of sophisticated transport calculations for this stellar model (see Figure 12 of Mirizzi et al. 2015). In all displayed runs the escaping luminosities (solid lines in the second panel from top) for  $\nu_e$  and  $\bar{\nu}_e$  are enhanced compared to the core luminosities (dashed lines) owing to the neutrino emission produced by the accretion and mantle cooling of the PNS.

While the Z9.6 progenitor explodes relatively quickly (at  $t_{\text{exp}} \sim 0.15$  s after core bounce, defined as the time when the outgoing shock passes  $500 \text{ km}$ ), it takes more than  $0.5$  s for the shocks in W18 and N20 to expand to  $500 \text{ km}$  and to accelerate outward (vertical dashed lines in Figure 7). In all three cases the explosion sets in after the mass shell  $M_4 = m(s = 4)$ , where the progenitor entropy reaches a value of  $4k_{\text{B}}$  per baryon, has fallen through the shock (see also Ertl et al. 2015).

Figures 8 and 9 provide an overview of the explosion and remnant properties of all simulated models for our Z9.6, W18, and N20 series. The general features are similar to the results obtained by Ugliano et al. (2012) for a different progenitor set, and they are identical to those discussed by Ertl et al. (2015) for stars with ZAMS masses  $M$  greater than  $13 M_{\odot}$ . In the mass range  $M \leq 13 M_{\odot}$  our present work not only employs updated

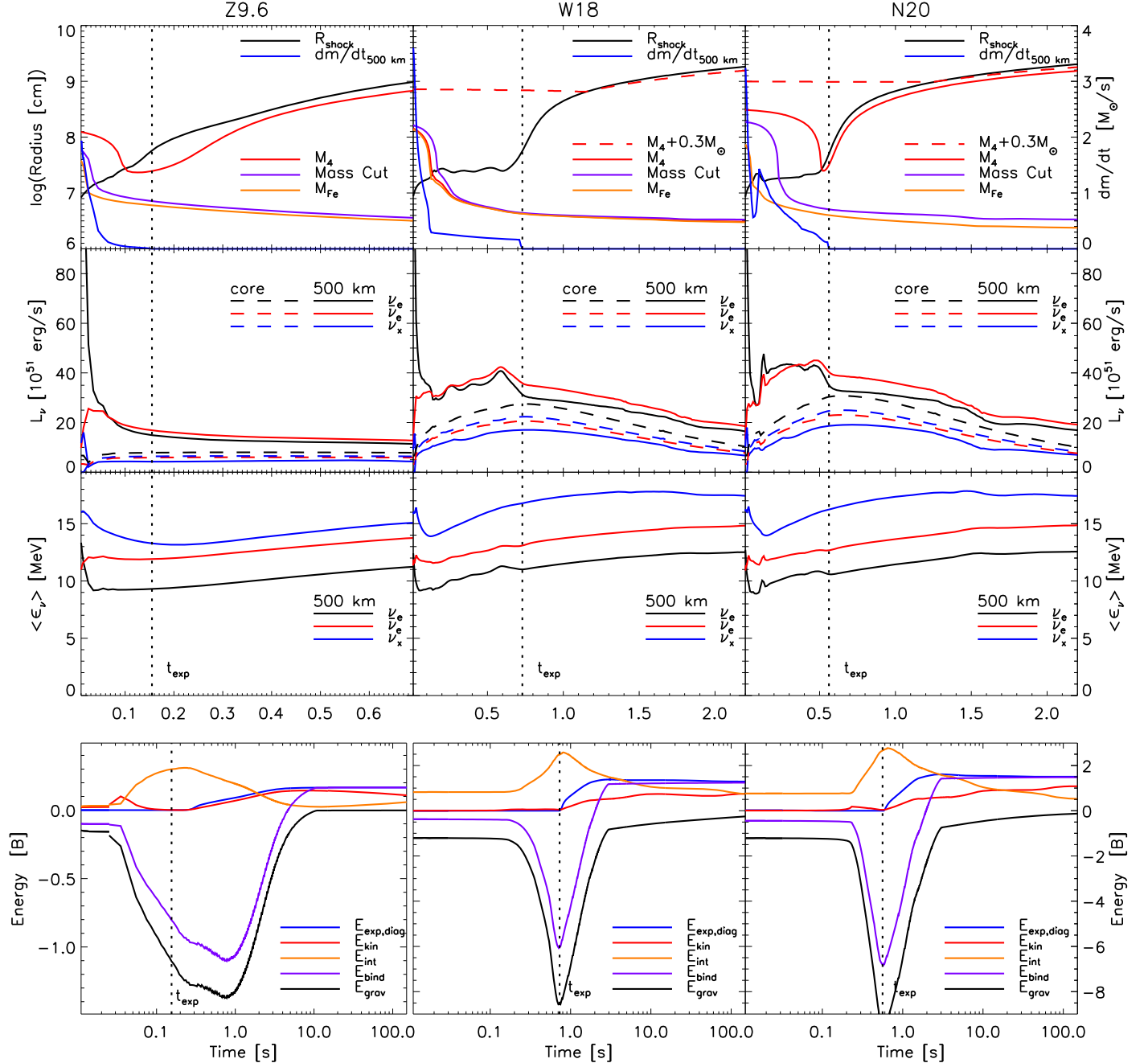


**Figure 7.** Time evolution of the Crab-like calibration model Z9.6 (left) and of the SN 1987A calibration models W18 (middle) and N20 (right). The top panels display as functions of post-bounce time the radius of the outgoing shock (black line), the mass accretion rate measured at 500 km (blue line; scale on the right side), and the radii of iron core (orange),  $M_4 = m(s = 4)$  (red;  $s$  is the entropy per nucleon),  $M_4 + 0.3 M_\odot$  (red dashed), and trajectory of the final mass cut (after completion of fallback; purple). The second panels from top show the luminosities of  $\nu_e$ ,  $\bar{\nu}_e$ , and a single species of heavy-lepton neutrinos  $\nu_x$  as labeled in the plot, measured at 500 km (solid lines) and at the inner grid boundary (dashed lines). The third panels from top show the mean energies of all neutrino species as radiated at 500 km. The vertical dotted lines indicate the onset time of the explosion defined by the moment when the outgoing shock passes the radius of 500 km. The bottom panels display the diagnostic energy of the explosion (integrated energy of all post-shock zones with positive total energy; blue line). Also shown are the kinetic energy (red), gravitational energy (black), and internal energy (orange) as integrals over the whole, final SN ejecta between the final mass cut (after fallback) on the one side and the stellar surface on the other. The total (binding) energy (purple) as the sum of these energies ultimately converges to the diagnostic energy, and both of these energies asymptote to the final explosion energy. While this convergence is essentially reached after  $\sim 10$  s in the case of Z9.6, the convergence of total energy and diagnostic energy takes tens of seconds in the other two cases.

progenitor models, but in contrast to the (seemingly ad hoc)  $\zeta$  reduction applied by Ertl et al. (2015), we also introduced the more elaborate treatment of the Crab-like models (i.e., of cases  $M \leq 12.0 M_\odot$ ) described in Section 3.1.3 to cure the problem of overenergetic low-mass explosions in Ugliano et al. (2012).

Figures 8 and 9 demonstrate that the  $\zeta$  modification used by Ertl et al. (2015) (see Figure 3 there) leads to basically the same overall explosion results as our present Crab-like calibration for the low-mass progenitors. This can be understood by the mathematical structure of the core luminosity as given by Equation (2), where a similar effect on  $L_{\nu,c}$  can be achieved by

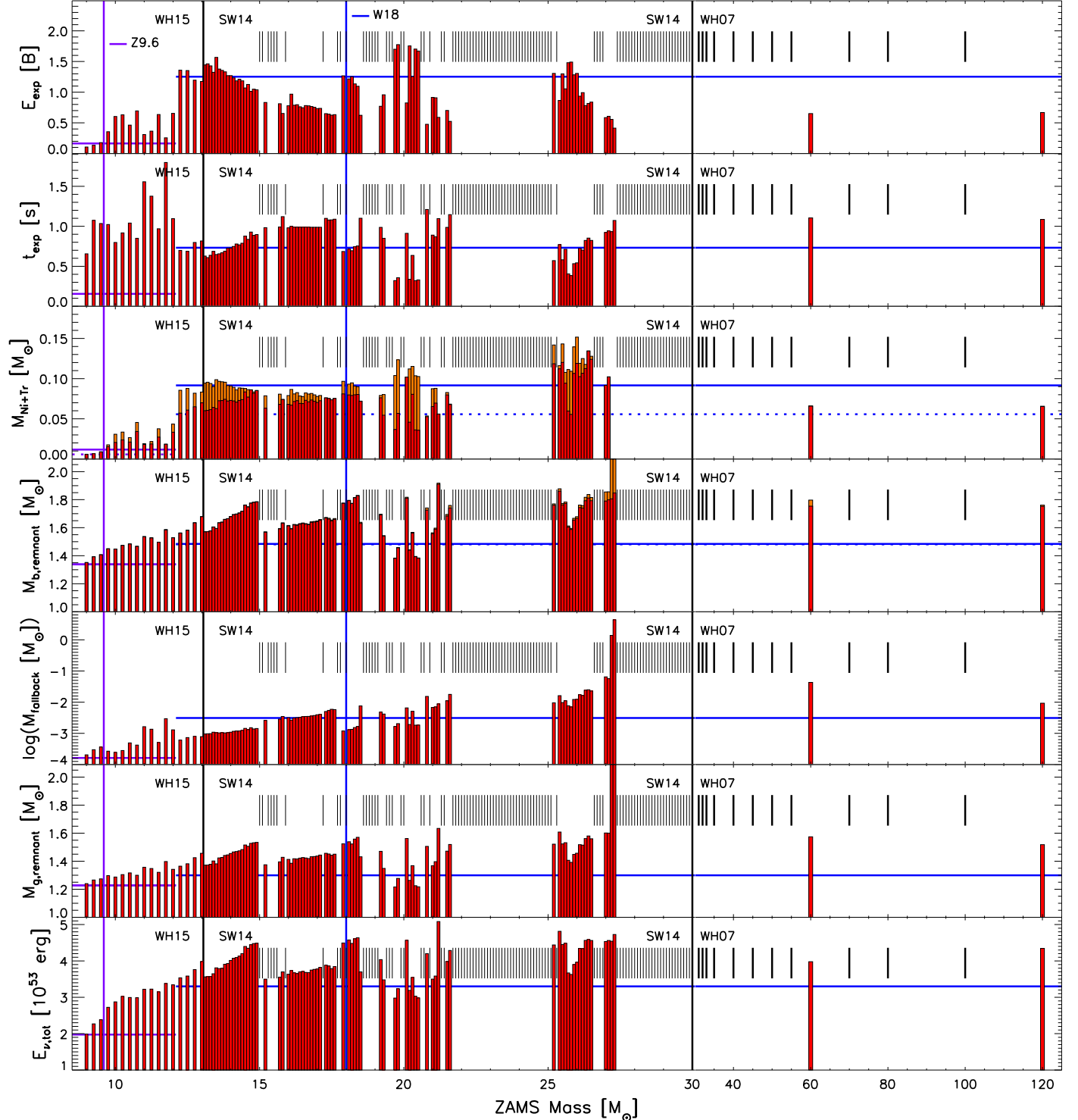


**Figure 8.** Explosion properties for all models exploded with the Z9.6 and W18 calibrations. Black vertical lines mark the boundaries between the different progenitor sets our model sample is composed of. The panels, from top to bottom, show the final explosion energy,  $E$ , in units of  $1 \text{ B} = 1 \text{ bethe} = 10^{51} \text{ erg}$ ; the time of the onset of the explosion,  $t_{\exp}$ ; the mass of finally ejected, explosively produced  $^{56}\text{Ni}$  (red bars) and tracer element (orange bars); the baryonic mass of the compact remnant, with the fallback mass indicated by orange sections on the bars; the gravitational mass of the compact remnant; and the total energy radiated in neutrinos,  $E_{\nu,\text{tot}}$ . The masses of the calibration models are indicated by vertical blue lines, and the corresponding results by horizontal solid or dashed blue lines, which extend over the mass ranges that are considered to have Crab-like or SN 1987A-like progenitor properties, respectively. Nonexploding cases are marked by short vertical black bars in the upper half of each panel.

either a reduction of the absolute value of  $S$  (by decreasing  $\zeta$ ) or an increase of  $R_c$  through a larger value of  $R_{c,f}$ . As discussed in detail by Ertl et al. (2015), the explosions of these stars set in fairly late after an extended phase of accretion, and the

explosion is powered by a relatively massive and energetic neutrino-driven wind. This seems compatible with the recent result of multidimensional simulations by Müller (2015), who found a long-lasting phase of simultaneous accretion and mass

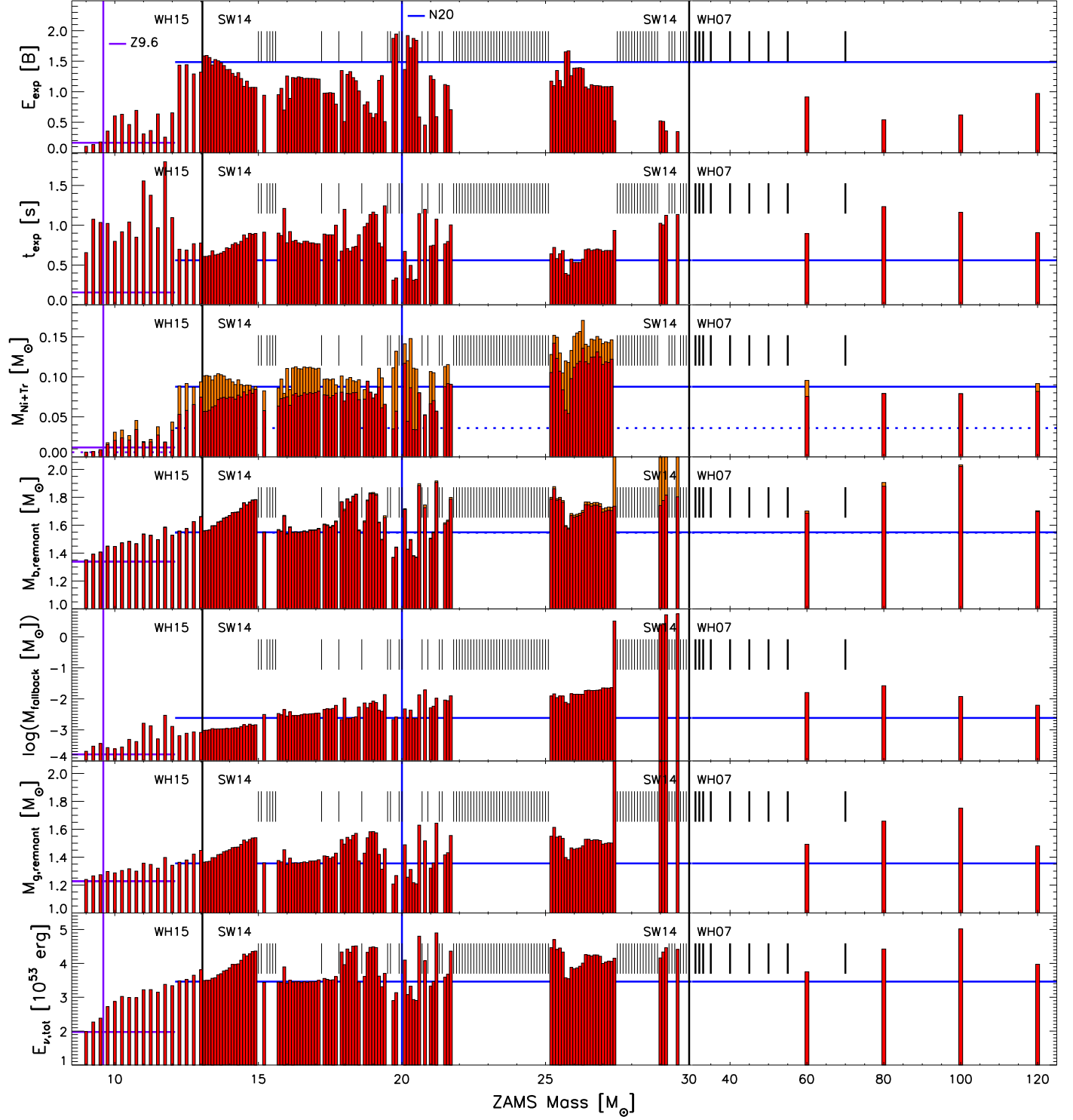


**Figure 9.** Same as Figure 8, but for P-HOTB simulations with the Z9.6 and N20 calibrations.

ejection after the onset of the explosion for stars in the mass range between  $11$  and  $12 M_{\odot}$ .

While SNe near the low-mass end of the investigated mass range tend to explode with the lowest energies and smallest production of  $^{56}\text{Ni}$ , our results exhibit a moderately strong correlation of these explosion parameters with ZAMS mass. Overall, our results appear compatible with the observational data collected by Poznanski (2013), in particular in view of the weakness of the  $M-E_{\text{exp}}$  correlation concluded from a critical

assessment of the observational analysis by Pejcha & Prieto (2015).

Although the remainder of the paper focuses on models based on the W18 and N20 calibrations, some results from P-HOTB are also given for the other three series, W15, W20, and S19.8. Among the SN 1987A models, W15 has both an unusually low compactness parameter (Table 1 in Ertl et al. 2015) and an extremely low value of  $M_{3000}$  (Figure 5), more Crab-like than SN 1987A-like. Nevertheless, we found

that W15, calibrated as an engine as described in Section 3.1.3, was almost as successful a central engine as W18, N20, and S19.8. In contrast, W20 is fairly inconspicuous with respect to compactness and  $M_{3000}$ , but turned out to be the clearly weakest engine with the largest number of failed explosions.

The behavior of W15 can be understood in terms of the two parameters  $M_4$  and  $\mu_4$  that determine neutrino-driven explosions, as discussed by Ertl et al. (2015).  $M_4$  is the stellar mass enclosed by the radius where the entropy per baryon is  $s = 4 k_B$  and  $\mu_4$ , the gradient,  $dM/dr$ , just outside of this location. W15 has much lower values of both  $M_4$  and  $\mu_4$  than all the other engine models. For this reason W15 has a low accretion component of the neutrino luminosity. Exploding SN 1987A with sufficiently high energy using W15 therefore requires that the parameters of the high-density core model provide a sufficiently powerful explosion, on their own, without much assistance from accretion. With this strong core component of the neutrino emission W15 also acts as a strong engine for other progenitor stars.

W20 is weak for other reasons. Its values of  $M_4$  and  $\mu_4$  are actually quite similar to those of N20, which is a considerably stronger engine. The main reason for the different strengths of these two cases is the fact that we tuned the N20 parameters such that SN 1987A exploded with about 1.5 B (Table 3), whereas for W20 we accepted an SN 1987A explosion energy of only 1.24 B (see Table 1 in Ertl et al. 2015). The higher explosion energy for N20 was necessary to obtain enough  $^{56}\text{Ni}$  from this explosion and is responsible for N20 being the more successful engine.

### 3.2. Simulating the Explosion in KEPLER

Linking the successful explosions back into the KEPLER code required care in order to preserve the energetics, remnant masses, and bulk nucleosynthesis determined in the more accurate simulation with neutrino physics. KEPLER is an implicit Lagrangian hydrodynamics code, and thus it can take longer time steps and carry a reaction network of arbitrary size. Since the pre-SN models used for the neutrino transport calculation were calculated using the KEPLER code, it was most natural to make the link at that time. Within the Lagrangian code, one then has two options for simulating the explosion—dumping a prescribed amount of energy in one or several zones, or moving a specified inner boundary, a “piston,” along a specified trajectory (i.e., radius as a function of time).

Here the piston approach was adopted, but considerable experimentation was devoted to determining the optimal trajectory. Major recoding would have been necessary to include neutrino energy transport in KEPLER, so one requirement was that the piston trajectory be located outside of the radius where, even at bounce, neutrino heating and modification of the composition were negligible. On the other hand, the piston needed to be deep enough in the star to give an accurate estimate of the explosion energy and iron synthesis. Experience showed that a piston situated too deep in the star accreted too much matter while waiting for neutrinos to reverse the accretion. The sudden outward motion of the large artificially accreted mass resulted in an overly powerful explosion and too much  $^{56}\text{Ni}$  production. Similarly, a piston situated too far out experienced an inadequate peak temperature to make iron. The density also was too low to acquire enough

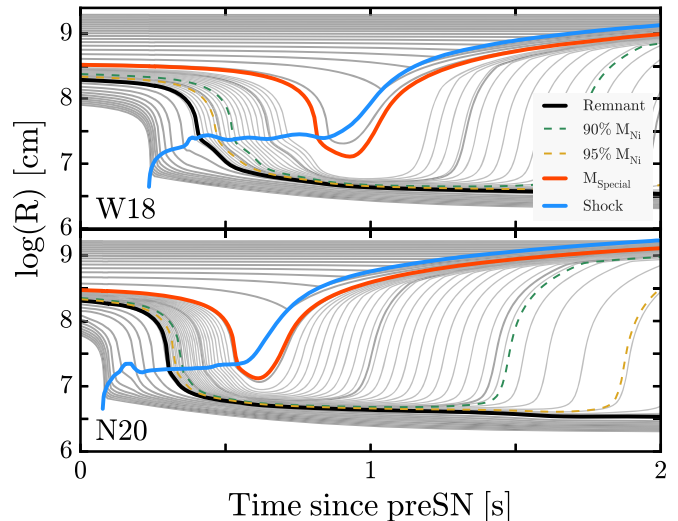


**Figure 10.** Evolution of baryonic mass shells from the explosion of two calibration models, W18 and N20. Thick gray lines are contours of constant enclosed masses in steps of  $0.04 M_\odot$  starting at  $1.1 M_\odot$ . The thin gray lines are mass shells in steps of  $0.004 M_\odot$  resolving the neutrino-driven wind, which is defined as the difference between the PNS mass at the onset of the explosion and its mass after  $\sim 15$  s. The solid blue line shows the shock radius, and the solid black curve shows the mass shell of the final mass cut. The solid red line shows the “special trajectory” used in the KEPLER code. Dashed yellow and green lines show the location of mass shells internal to the initial ejection of 95% and 90%, respectively, of the iron-group elements in the P-HOTB calculations.

momentum to make a strong shock unless the piston was moved for a very long time.

After some experimentation with various trajectories, the “special trajectories” were chosen (Figure 10). These are Lagrangian mass coordinates that, in the neutrino transport calculation, bounce between 80 and 140 km (most between 120 and 140 km). They mark the first mass shell to be accelerated outward when the stalled shock revives. Several such trajectories were followed in KEPLER and gave reasonably good agreement, typically within 20%, with the results from P-HOTB for both SN energy and iron-group synthesis. Better agreement could be obtained, however, if the significant stagnation at small radius for the “special trajectory” used by KEPLER was shortened. The procedure that was eventually adopted used a piston with the following velocity evolution for inward ( $t < t_{\min}$ ) and outward ( $t > t_{\min}$ ) motions, where  $t_{\min}$  is the time when the piston reaches its smallest radius,  $r_{\min}$ :

$$\begin{aligned} v_{\text{in}} &= (r_{\min} - r_z - v_z t_{\min}) t / t_{\min}^2 + v_z \quad \text{for } t < t_{\min} \\ v_{\text{out}} &= \sqrt{\frac{2G\alpha m_z(r_{\max} - r)}{(r_{\max} r)}} \quad \text{for } t > t_{\max} \end{aligned}, \quad (7)$$

where subscript  $z$  denotes the initial piston location in the pre-SN model according to the special trajectory from the P-HOTB calculation, i.e.,  $m_z$ ,  $r_z$ ,  $v_z$  are the initial Lagrangian location of the trajectory, the corresponding initial radius, and collapse velocity, respectively. The inward path of the piston follows a parabola that connects this initial location to  $r_{\min}$  at  $t_{\min}$ . The outward path from  $r_{\min}$  to  $r_{\max}$  (taken as  $10^9$  cm) is determined by the time-dependent velocity that is equal in speed to the free-fall velocity that corresponds to the gravitational potential from the piston mass  $m_z$  times the multiplier  $\alpha$  (Figure 11).

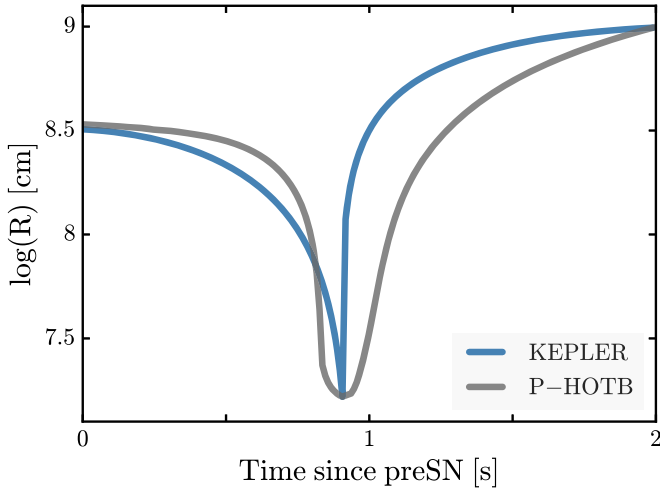


**Figure 11.** Trajectory from the neutrino-driven explosion with P-HOTB (gray) compared with the corresponding trajectory from KEPLER (blue) for the explosion of the W18 engine itself. In all cases, the trajectories from the two codes have a common starting radius and time and the same minimum radius and time.

For the stars that exploded in P-HOTB, the desired kinetic energy at infinity in KEPLER is obtained by iterating on  $\alpha$ . This required an earlier, more rapid motion outward for the adopted piston. By design, the two explosion models thus agreed almost exactly in explosion energy and piston mass. They also agreed to typically better than 10% in the mass of iron-group nuclei that were synthesized (Tables 7 and 8). Here the total iron in P-HOTB calculation is taken as the amount outside the final fallback mass.

To make the agreement in  $^{56}\text{Ni}$  mass even better, first, for a few models the starting location in mass of the special trajectory,  $m_z$ , was slightly varied, usually by  $\sim 0.01 M_{\odot}$ , so that the KEPLER total iron mass lies roughly in between the special and fallback trajectories (Figure 12). Then using the innermost zone abundances, most models were scaled up slightly until the fallback trajectory value, so that the final disagreement of iron-group synthesis was a few percent at most. The full tabulated list of all piston parameters for all explosion calculations is available at the MPA-Garching archive (see footnote 4).

In the remainder of the paper, the baryonic remnant masses, the kinetic energies at infinity of the ejecta, and the total iron-group synthesis are based on the 1D neutrino-powered explosions using P-HOTB. Only the isotopic nucleosynthesis (of all elements including pre-SN mass loss) and the light curves are taken from KEPLER.

#### 4. EXPLOSION PROPERTIES

Inserting the standard “central engines” described in Section 3 in the various pre-SN stars resulted in a wide variety of outcomes depending on the properties of each progenitor, especially its mass and compactness, and the choice of 87A model used for the engine’s calibration (Figure 13). Generally speaking, weaker central engines like W20 gave fewer SNe than stronger engines like N20.

This is an interesting point that warrants elaboration. Not every model for 87A will give equivalent, or even necessarily valid, results when its central engine is inserted in other stars. SN 1987A was a blue supergiant in a galaxy with lower metallicity than the Sun. All pre-SN models considered here,

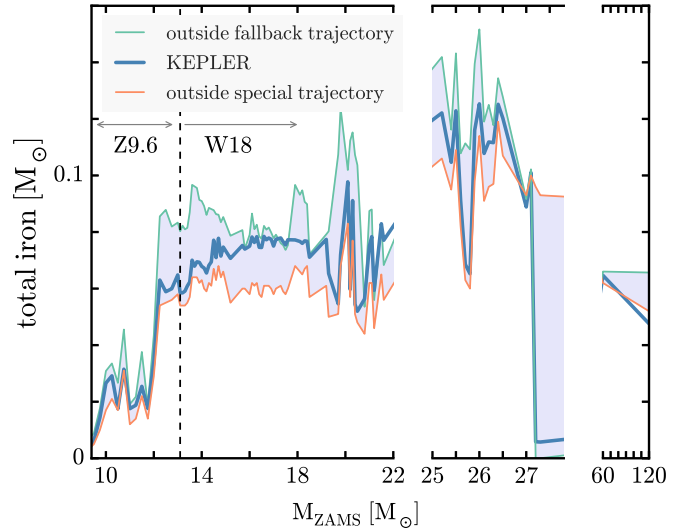


**Figure 12.** Comparison of iron production in the KEPLER and P-HOTB calculations for all models that exploded using the Z9.6 and W18 engines. The shaded gray region is bounded on the bottom by the total iron produced by P-HOTB outside the “special” trajectory (orange), and on the top by the total iron ejected (green). The thick blue curve represents total iron production in the converged KEPLER explosions.

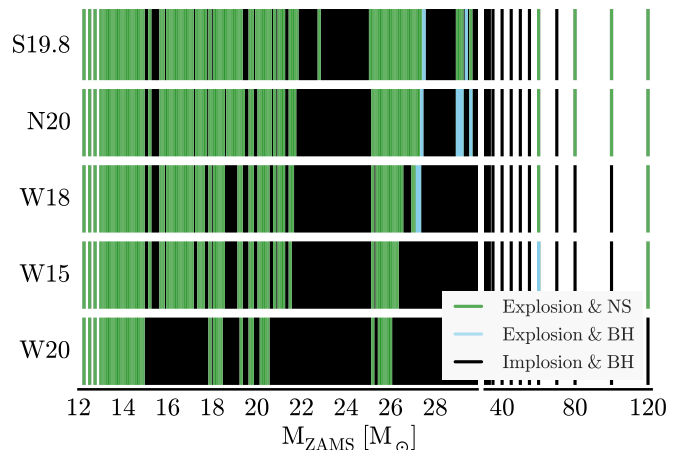


**Figure 13.** Explosion outcomes from the five different central engines for SN 1987A (Tables 1 and 3) shown in comparison. Successful explosions that make neutron stars are green, the explosions that make BHs through fallback are light blue, and the failures, which make BHs, are black lines. The calibrators are listed by the engine strength, weakest at the bottom. Models heavier than  $12.25 M_{\odot}$  were covered by these five engines; all lighter models produced successful explosions by the Z9.6 engine calibrated to Crab SN.

except those that lost their envelopes before exploding, are red supergiants with an initially solar composition. The SN 1987A models, at least those that made blue supergiant progenitors (Table 1), also used a different value for semiconvective mixing that affected the size of the carbon–oxygen core for that mass (made the core smaller). One of the models, W18, included rotation, while the present survey does not. Our calculations are 1D, not 3D. Finally, one expects significant variations in pre-SN core structure even for two stars of very similar initial mass and pre-SN luminosity (Sukhbold & Woosley 2014).

The very similar results for “explodability” for models N20, W18, W15, and S19.8 are thus welcome and suggest a robustness to the answer that might not necessarily have existed. They also justify the neglect of model set W20 in the

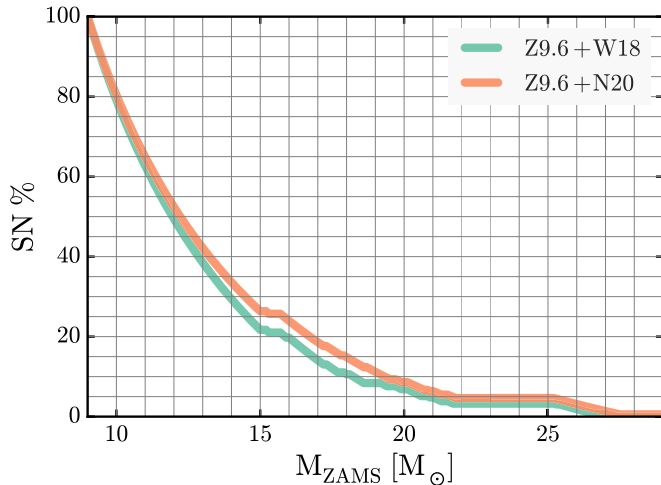


**Figure 14.** Percentage of SNe II above a given main-sequence mass for explosions using the Z9.6 and W18 or N20 engines. A Salpeter IMF has been assumed. Successful explosions above  $30 M_{\odot}$  do not make SNe II.

surveys of nucleosynthesis carried out in Section 6. Use of such a weak engine would grossly underproduce the heavy elements, especially the light *s*-process (Brown & Woosley 2013). A much larger SN rate would be required to make even abundant elements like silicon and oxygen. The results obtained here for solar-metallicity stars are also very similar to those of Pejcha & Thompson (2015, their Figure 12), who used a very different approach. Qualitatively, the outcome seems more influenced by pre-SN structure than details of the central engine, provided that that engine is sufficiently powerful to explode many stars.

Models are normalized to SN 1987A here because it was a well-studied event with precise determinations for its explosion energy and  $^{56}\text{Ni}$  mass, as well as its progenitor properties. One could take a different tack and use an even more powerful central engine than N20 in order to achieve optimal agreement with the solar abundances. That was not done here.

Also given in Figure 14 is the fraction of successful SNe above a certain main-sequence mass, but below  $30 M_{\odot}$ . Since heavier stars either fail to explode or explode after losing their hydrogen envelopes, this would be the fraction of SNe IIP.

#### 4.1. Relation to “Compactness”

The distribution of successful explosions in Figure 13 is not a simply connected set. The compactness parameter as originally defined in O’Connor & Ott (2011) was innovative for its emphasis on the nonmonotonic outcome expected for the deaths of stars of different masses, but is by no means a unique descriptor. Any parameter that samples the density gradient outside the iron core will correlate with explodability. Other measures could be, for example, the free-fall time from a particular mass shell, the mass enclosed by a fiducial radius, binding energy outside a fiducial mass,  $d(\text{BE})/dr$ , the mass where the dimensionless entropy equals 4, etc. Recently, Ertl et al. (2015) have shown that a physically based two-parameter description of “compactness” can predict explodability for the present set of models presented with almost 100% accuracy (see Figure 6 of that paper). No known single-parameter criterion works as well. A less accurate but perhaps more physically intuitive predictor of explosion is the mass derivative of the binding energy at  $\sim 2 M_{\odot}$ , shown in Figure 15.

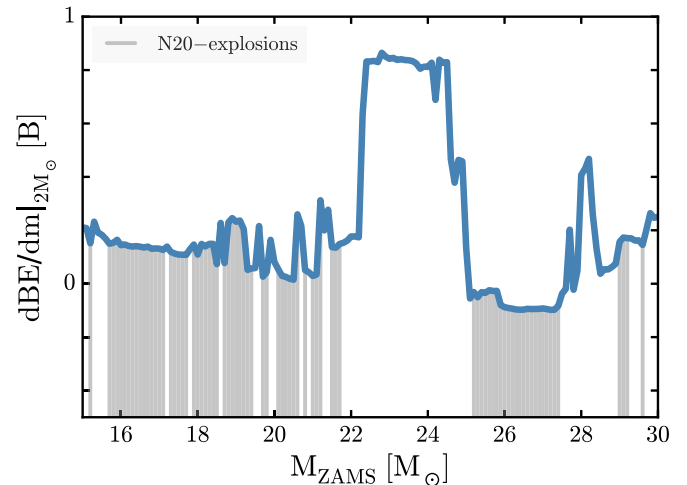


**Figure 15.** Mass derivative of the binding energy ( $1 \text{ bethe} = 10^{51} \text{ erg}$ ) outside  $2 M_{\odot}$  as a function of ZAMS mass compared with the explosion outcome for the N20 engine. The successful explosions are noted with gray vertical lines. Though this does not work as well as the two-parameter method of Ertl et al. (2015), it is one of the better single-parameter criteria for an explosion.

As expected, the successful explosions are, by whatever measure, the outcome of core collapse in stars with steep density gradients around their iron cores. As shown in Figure 1,  $\xi_{2.5}$  has a very small value for stars below  $12.5 M_{\odot}$ , and it slowly increases to about 0.2 until  $15 M_{\odot}$ . All of these small models are particularly easy to explode because they are essentially degenerate cores inside of loosely bound hydrogenic envelopes, especially at the lower-mass end. All versions of the central engine explode stars lighter than this limit. Between  $15$  and  $22 M_{\odot}$  stars become more difficult to explode and the outcome can be highly variable for even small changes in the initial mass, especially near  $20 M_{\odot}$ , where central carbon burning transitions from convective to radiative. From  $22$  to  $25 M_{\odot}$ , very few or no successful explosions were found for all central engines. There then comes an island around  $25$ – $27 M_{\odot}$  that once again explodes. The nonmonotonic nature of compactness is due to the migration of the location of carbon- and oxygen-burning shells with changing mass (Sukhbold & Woosley 2014). From  $30 M_{\odot}$  on up to about  $60 M_{\odot}$ , nothing explodes, except for the strongest engines. Eventually, however, the large mass loss appropriate for such large solar-metallicity stars removes the hydrogen envelope and whittles away at the helium core, making it once again compact and easier to explode, at least for the stronger engines. The results are therefore sensitive to the mass-loss prescription employed.

#### 4.2. Systematics of Explosion Energy and $^{56}\text{Ni}$ Mass

On general principles, one expects correlations to exist among the explosion energy,  $^{56}\text{Ni}$  production, and compactness parameter in successful explosions. The compactness parameter is a surrogate for the density gradient outside of the iron core. The larger  $\xi_{2.5}$  is (Figure 1), the shallower the density gradient and the greater the mass closer to the origin where high temperature is attained in the shock. A frequently used approximation that takes advantage of the fact that, during the epoch of nucleosynthesis, most of the energy behind the shock is in the form of nearly isothermal radiation is (Weaver &

Woosley 1980)

$$E \approx \frac{4}{3} \pi a T_s^4 R_s^3, \quad (8)$$

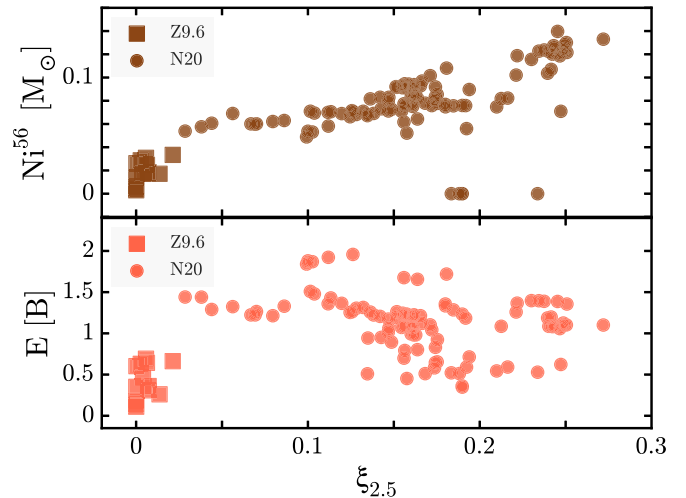
where  $E$  is the total internal energy in the shocked region,  $T_s$  the temperature at the shock, and  $R_s$  its radius. After a short time, this internal energy converts into kinetic energy and becomes nearly equal to the final kinetic energy of the SN. A shock temperature in excess of about  $5 \times 10^9$  K is required for the production of  $^{56}\text{Ni}$ , so for an explosion energy of  $10^{51}$  erg, most of the matter between the final mass cut and a point located at 3600 km in the pre-SN star will end up as  $^{56}\text{Ni}$ . This is provided, of course, that the 3600 km point does not move a lot closer to the origin as the explosion develops, and the final mass cut lies inside of the initial 3600 km mass coordinate. Both assumptions are generally valid, although fallback can occasionally reduce  $^{56}\text{Ni}$  synthesis to zero.

One expects then, for stars of similar initial compactness and final remnant mass, a weak positive correlation between explosion energy and  $^{56}\text{Ni}$  production. A greater explosion energy increases  $R_s(5 \times 10^9 \text{ K})$ , and this larger radius encompasses a greater mass. This correlation can be obscured, or at least rendered ‘noisy’ by variations in the compactness, remnant masses, and explosion energies. In particular, the compactness of pre-SN stars below  $12 M_\odot$  is very small, i.e., the density gradients at the edges of their iron cores are very steep. These stars are also easy to explode and have substantially lower final energies than the heavier stars. The radius that reaches  $5 \times 10^9$  K is small, and the density gradient is also steep there. Thus, as has been known for some time, stars below  $12 M_\odot$  are not prolific sources of iron. These low-mass SNe, in fact, separate rather cleanly, in theory at least, into a separate class with low energy and low  $^{56}\text{Ni}$  yield (see Figures 8 and 9)—and as we shall see in Section 7, shorter, fainter light curves.

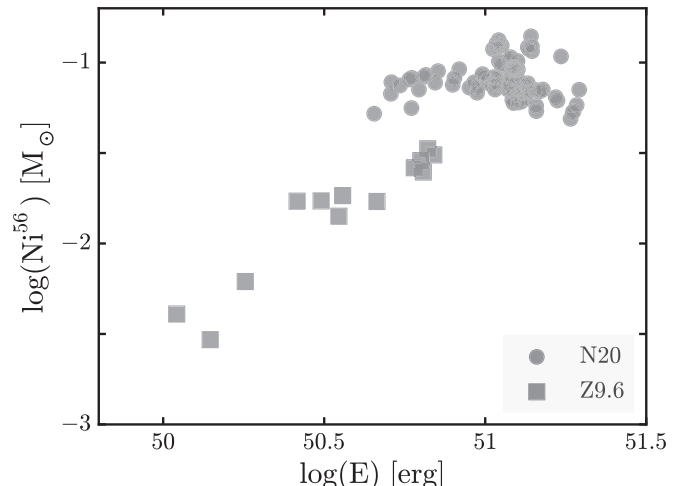
A correlation is also expected between explosion energy and compactness, but which way does it go? Stars with more compact cores (low values of  $\xi_{2.5}$ ) are easier to explode and thus explode with lower energy, but the stars with extended cores (larger values of  $\xi_{2.5}$ ) might also have lower final energy simply because they are harder to explode. The neutrinos have to do more work against infall, and the explosion may be delayed. The mantle has greater binding energy that must be subtracted, but the additional accretion might increase the neutrino luminosity and may give a larger explosion energy.

Figure 16 shows the  $^{56}\text{Ni}$  mass versus compactness parameter for the model series Z9.6 and N20. The clustering of points around  $\xi_{2.5} = 0$  with low  $^{56}\text{Ni}$  and energy is expected, as is a transition region to higher values of both. Over most of the compactness parameter range, however, the explosion energy is roughly constant, with some small variation due to the effects just mentioned. With a constant explosion energy, the  $^{56}\text{Ni}$  synthesis is slightly greater for the stars with shallower density gradients, i.e., larger  $\xi_{2.5}$ .

It is also interesting to compare the correlation between  $^{56}\text{Ni}$  production and the explosion energy, especially since both can potentially be measured. Two classes of events are expected—the stars above  $12 M_\odot$  and stars below  $12 M_\odot$ . A slight positive correlation of  $^{56}\text{Ni}$  with explosion energy is also expected in the more massive stars. Figure 17 supports these expectations, but shows that the variation of  $^{56}\text{Ni}$  production in stars above



**Figure 16.** Amount of nickel and explosion energies resulting from use of the Z9.6 and N20 engines shown as functions of the compactness parameter (Equation (1)). The top panel shows a positive correlation of  $^{56}\text{Ni}$  production with compactness. More matter is heated by the SN shock for models with high  $\xi_{2.5}$ . The explosion energy is low for stars with very small compactness parameter because their thin shells are inefficient at trapping neutrino energy and there is very little luminosity from accreting matter. These effects saturate, however, around  $10^{51}$  erg, since the energy provided by the neutrino source is limited and the binding energy of the overlying shells is harder to overcome. The results for the W18 engine are not plotted, but closely follow the N20 points plotted here.



**Figure 17.** Amount of  $^{56}\text{Ni}$  nucleosynthesis vs. the logarithm of the final kinetic energy of the explosion in units of  $10^{51}$  erg for the Z9.6 (squares) and N20 (circles) series. Models below an initial mass of  $12 M_\odot$  (half of all SNe) explode easily and produce small amounts of nickel that correlate with their explosion energy. Higher-mass models, on the other hand, produce a nearly constant  $0.07 M_\odot$  of nickel, except for a few cases with large fallback. The results for the W18 engine, though not plotted here for clarity, look very similar to those of N20.

$13 M_\odot$  is really quite small. While it may be tempting to draw a straight line through the full data set, this obscures what is really two different sorts of behavior. It is important to note that about half of all observable SNe in the current survey have masses below  $12 M_\odot$  (Table 4).

A similar correlation between  $^{56}\text{Ni}$  and kinetic energy has been discussed by Pejcha & Thompson (2015) and compared with observational data (their Figure 20). The observations (Hamuy 2003; Spiro et al. 2014) show a particularly strong correlation of plateau luminosity with the inferred mass of  $^{56}\text{Ni}$ ,

**Table 4**  
Explosion Results for the Z9.6 Engine

Progenitor	$M_{\text{Ni}} (M_{\odot})$ K. P.	$E_{\text{expl.}} (\text{B})$ K. P.	$M_{\text{remnant}} (M_{\odot})$ P.
9.0	0.004   0.006	0.11   0.11	1.35
9.25	0.003   0.007	0.14   0.14	1.39
9.5	0.006   0.009	0.18   0.18	1.41
9.75	0.014   0.018	0.35   0.35	1.45
10.0	0.027   0.031	0.60   0.60	1.45
10.25	0.029   0.034	0.63   0.63	1.47
10.5	0.018   0.027	0.46   0.46	1.48
10.75	0.031   0.046	0.69   0.69	1.47
11.0	0.018   0.019	0.31   0.31	1.54
11.25	0.019   0.022	0.36   0.36	1.53
11.5	0.025   0.038	0.64   0.64	1.50
11.75	0.018   0.018	0.26   0.26	1.59
12.0	0.034   0.043	0.66   0.66	1.53

**Note.** K. = KEPLER and P. = P-HOTB. The remnant masses are listed only for the P-HOTB calculations since they are almost always identical to those of KEPLER.

extending all the way down to  $10^{-3} M_{\odot}$  for the latter. Our lowest  $^{56}\text{Ni}$  synthesis, in a successful SN that left a neutron star remnant, was  $0.003 M_{\odot}$  for the  $1.4 \times 10^{50}$  erg explosion calculated with KEPLER for the  $9.25 M_{\odot}$  model using the Z9.6 central engine. Table 7 gives a substantially different value for  $^{56}\text{Ni}$  synthesis in the  $9.0$ – $9.5 M_{\odot}$  models using P-HOTB, and the discrepancy highlights some uncertain physics that warrants discussion. Because the shock-produced  $^{56}\text{Ni}$  is very small in these low-mass stars, the neutrino wind contribution is non-negligible. For the  $9.25 M_{\odot}$  model, P-HOTB calculates that  $0.00659 M_{\odot}$  of  $^{56}\text{Ni}$  is ejected, but about half of this is made inside the “special trajectory” (Figure 10) used by KEPLER to represent the mass cut (Section 3.2), and most of this comes from the approximately simulated wind in P-HOTB. In that calculation all iron-group and trans-iron species in the neutrino-powered wind are represented by  $^{56}\text{Ni}$  if neutrino interactions lead to  $Y_e \geq 0.49$ . Otherwise,  $^{56}\text{Ni}$  is replaced by a “tracer nucleus” for neutron-rich species. The network employed does not therefore track the composition in detail.

For heavier stars that make most of the elements, this small difference is negligible, but for these very light stars it is not. The actual  $^{56}\text{Ni}$  synthesis in these very light stars is probably between the KEPLER and P-HOTB values in Table 7. Indeed, KEPLER was taken to be “converged” when its  $^{56}\text{Ni}$  synthesis lay between these two values—the actual ejected value in P-HOTB and the value outside of the “special trajectory.” This means that the very low values of  $^{56}\text{Ni}$  synthesis calculated for the  $9.0$ – $9.5 M_{\odot}$  models by KEPLER are more uncertain than for other masses and possibly a lower bound to the actual value. For nucleosynthesis purposes (Section 6), the KEPLER iron-group synthesis was renormalized to agree exactly with the full P-HOTB value. It is also possible to get still smaller values for  $^{56}\text{Ni}$  in heavier stars that experience appreciable fallback.

We note in passing that the  $^{56}\text{Ni}$  produced by electron-capture SNe is mostly made in their neutrino-powered winds. Wanajo et al. (2011c), using 1D and 2D explosion models that incorporated realistic neutrino transport, obtained about  $0.003 M_{\odot}$  of  $^{56}\text{Ni}$  for an electron-capture SN, which is very similar to

the wind component predicted with P-HOTB for the present explosions of our low-mass progenitors.

On the upper end, one might be tempted to extend this correlation of  $^{56}\text{Ni}$  production and kinetic energy to still more energetic events, including gamma-ray bursts and ultraluminous SNe (Kushnir 2015), but these other events likely have other explosion mechanisms, and the paper here is focused on nonrotating, neutrino-powered models.

## 5. BOUND REMNANTS

### 5.1. Neutron Stars

The P-HOTB calculations continue to sufficiently late times ( $\sim 10^6$  s) to include most fallback and accurately determine the baryonic mass that collapses to a neutron star. They also give an estimate of the gravitational mass based on the neutrino loss of the neutron star cooling model employed in the simulations (see Figures 8 and 9). These results are in very good agreement with a simple, radius-dependent correction (Lattimer & Prakash 2001) that gives the neutron star’s gravitational mass,  $M_g$ , from its calculated baryonic mass,  $M_b$ :

$$\beta = \frac{GM_g}{c^2 12 \text{ km}}, \quad (9)$$

$$\frac{M_b - M_g}{M_g} = 0.6 \frac{\beta}{1 - 0.5\beta}, \quad (10)$$

where  $G$  is the gravitational constant and  $c$  the speed of light.

A distribution of gravitational masses can then be constructed by weighting the occurrence of each of our successful models according to a Salpeter IMF. The resulting frequencies are plotted as a function of neutron star mass in Figure 18 and are seen to be in reasonably good agreement with the observed values compiled by Özel et al. (2012) and F. Özel & P. Freire (2016, in preparation) in terms of overall spread and mean value. Our maximum neutron star mass for the W18 series is  $1.68 M_{\odot}$ , and the minimum is  $1.23 M_{\odot}$ . Use of 10 km for the neutron star radius reduces these numbers to 1.64 and  $1.21 M_{\odot}$  and reduces the average mass by about  $0.02 M_{\odot}$ . Here we note that, owing to the complications of evolutionary effects, we did not build a PDF from the observed measurements that reflects proper weights of different populations. Instead, the aim here is purely to provide a visual guide to the currently known measurements.

Different mass neutron stars, for the most part, come from different ranges of main-sequence mass with lower-mass progenitors producing low-mass neutron stars. There is some overlap, however. Remnants from stars between 15 and 18 solar masses have slightly lower masses than some below 15 solar masses. Stars above  $18 M_{\odot}$  contribute little to the distribution, but do so over a broad range of neutron star masses. This reflects both the variable mass of the very massive stars at death, due to extensive mass loss, and inherent variability in their compactness. While we have not carried out a statistical analysis, Figure 18 does suggest some bimodality in the distribution, with a separate peak around  $1.25 M_{\odot}$  (see also Schwab et al. 2010). It is interesting to note that these low-mass neutron stars are produced without invoking electron-capture SNe (e.g., Schwab et al. 2010), none of which are in our sample. Indeed, heavier stars that experience iron-core-collapse SNe are capable, in principle, of producing lighter neutron stars than electron-capture SNe since the values of  $Y_e$  in the cores of the latter are close to 0.5 at the onset of collapse,

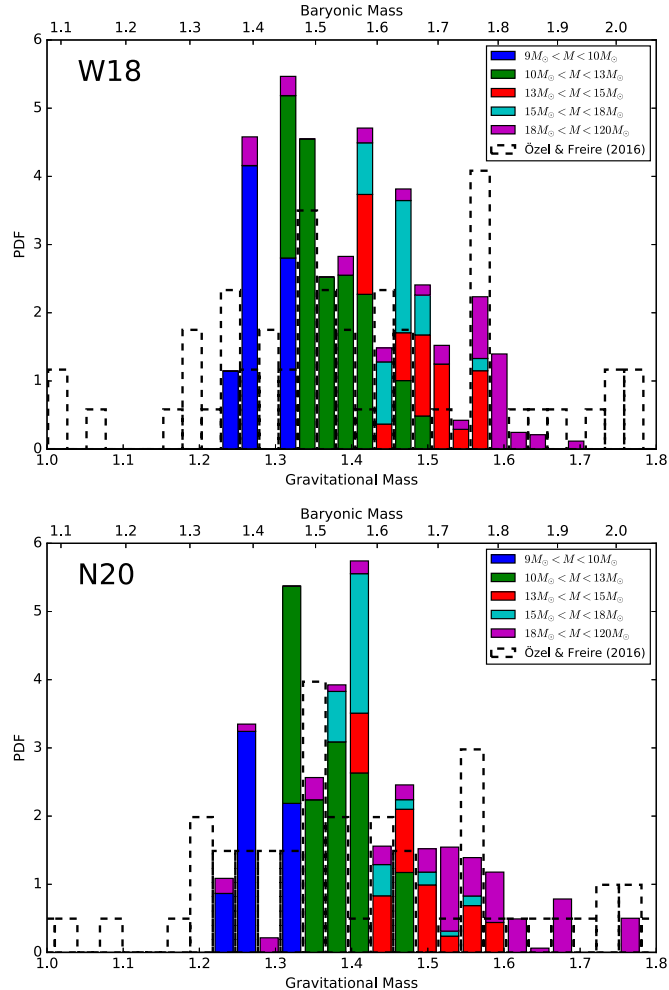


**Figure 18.** Distributions of neutron star masses for the explosions calculated using P-HOTB compared with the observational data from Özel et al. (2012) and F. Özel & P. Freire (2016, in preparation). Several neutron stars with masses greater than the maximum mass plotted here have been observed, and the lightest observational masses have large error bars. In the top panel, the W18 calibration is used, and in the bottom, the N20 calibration. Both distributions show some weak evidence for bimodality around 1.25 and  $1.4 M_{\odot}$ . Results have been color-coded to show the main-sequence masses contributing to each neutron star mass bin. Note that this is not a direct comparison to the observations, as the measured values may already include accretion (i.e., not birth masses) and have not been properly weighted based on their measurement uncertainties and the relative contributions of different classes of neutron stars to the total population.

while they are substantially less after oxygen and silicon burning in the former. In quite heavy stars, this destabilizing effect is more than compensated for by the high entropy and mild degeneracy, but in lighter  $9\text{--}11 M_{\odot}$  stars,  $Y_e$  becomes a major determinant for the onset of core collapse.

An average neutron star mass can also be generated from an IMF-weighted sampling of the successful explosions. The results for four different calibrations of the central engine for SN 1987A, each including the normalization to the Crab for stars below  $13 M_{\odot}$ , are given for a Salpeter IMF in Table 4. These values are not very sensitive to the central engine used for SN 1987A, but are determined more by pre-SN properties. All lie close to the (error-weighted) observational means given by Lattimer (2012) of  $1.368 M_{\odot}$  for X-ray and optical binaries,  $1.402 M_{\odot}$  for neutron star binaries, and  $1.369 M_{\odot}$  for neutron

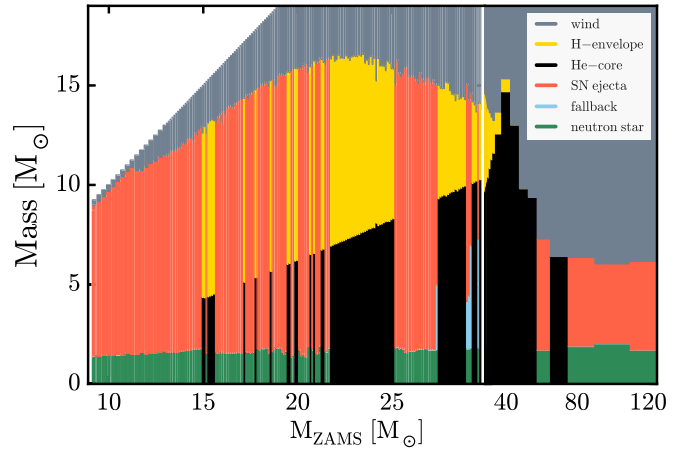


**Figure 19.** Mass ‘budget’ for each star based on results using the Z9.6 and N20 engines. Gray shows mass lost to winds. For the successfully exploded models, the compact remnant mass is shown in green. For a few models that experienced fallback, the fallback mass is shown in blue. Except near  $30 M_{\odot}$ , fallback is negligible. The helium cores and the hydrogen envelopes of the ‘failed’ explosions are shown in black and yellow, respectively. The resulting BH mass from an implosion will most likely include the full pre-SN star (black plus yellow), or just the helium core (black). Results using the W18 engine are qualitatively similar, with fewer explosions and fewer cases with significant fallback.

star—white dwarf binaries. They are not far from the average neutron star mass found by Schwab et al. (2010),  $1.325 \pm 0.056 M_{\odot}$ . These new theoretical values are closer to the observations than the results from Brown & Woosley (2013).

Table 4 also gives the average baryonic mass of the remnants of successful explosions,  $\bar{M}_b$ , the average SN kinetic energy at infinity,  $\bar{E}$ , and the range of average  $^{56}\text{Ni}$  masses, all as calculated in P-HOTB. The lower bound ignores the contribution from the neutrino-powered wind, while the upper bound assumes that all of the wind not in the form of  $\alpha$ -particles is  $^{56}\text{Ni}$ . Based on post-processing with KEPLER, this may be an overestimate of the actual  $^{56}\text{Ni}$  production by 10%–20%. The column labeled SN% is the IMF-weighted fraction of all stars studied that blew up and left neutron star remnants. One minus this fraction is the percentage that became BHs. The last column gives the numerical fraction of all successful explosions that have main-sequence masses above 12, 20, and  $30 M_{\odot}$ . The small value above  $20 M_{\odot}$  compares much better than past surveys with the results of Smartt (2009, 2015), who place an upper limit on observational SNe of about  $18 M_{\odot}$ . The successful explosions above  $30 M_{\odot}$  are all Type Ib or Ic.

## 5.2. Black Holes

Stellar collapses that fail to create a strong outward-moving shock after 3–15 s in P-HOTB (with variations due to the progenitor-dependent mass accretion rate) are assumed to form BHs. In the absence of substantial rotation, it is assumed that the rest of the core of helium and heavy elements collapses into that hole. The fate of the hydrogen envelope is less clear. In the more massive stars, above about  $30 M_{\odot}$ , the envelope will already have been lost to a wind. In the lighter stars, all of which are red supergiants, the envelope is very tenuously bound. Typical net binding energies are  $\sim 10^{47}$  erg. Any small core disturbance prior to explosion (Shiode & Quataert 2014) or envelope instability (Smith & Arnett 2014) could lead to its

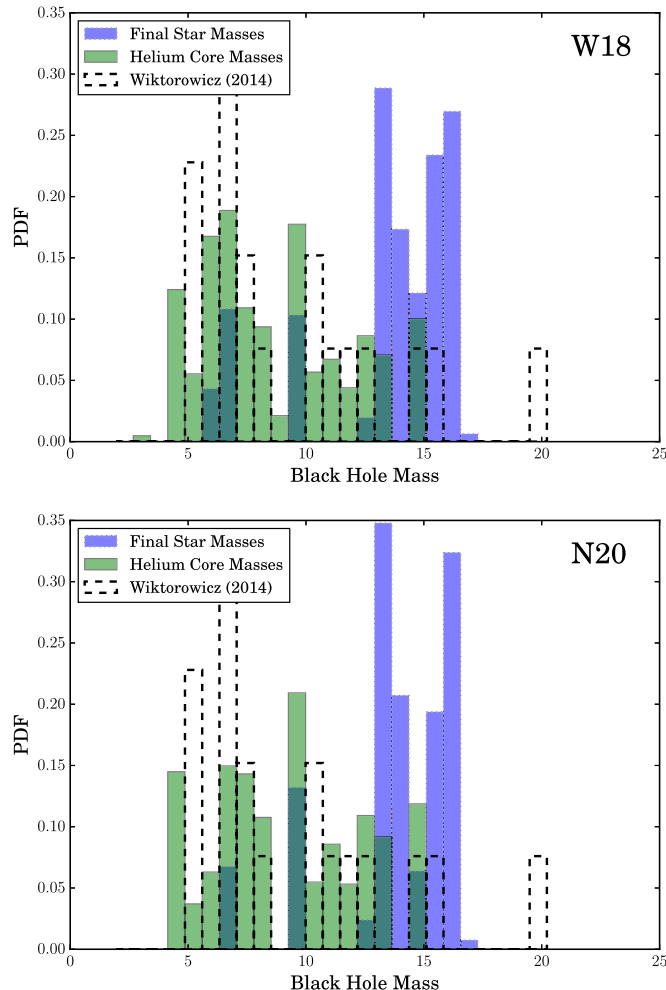


**Figure 20.** Distributions of BH masses for the explosions calculated using P-HOTB compared with the observational data from Wiktorowicz et al. (2014) (see footnote 5) in gray. Theoretical results are shown based on two assumptions: (1) that only the helium core implodes (green), or (2) that the whole pre-SN star implodes (blue). Observations are more consistent with just the helium core imploding. As in Figure 18, this is not a direct comparison to the observations.

ejection in many cases. Even if the envelope is still in place when the iron core collapses, the sudden loss of mass from the core as neutrinos can lead to the unbinding of the envelope (Nadezhin 1980; Lovegrove & Woosley 2013).

Figure 19 shows the masses ejected and neutron star remnant masses for the successful explosions using the Z9.6 and N20 central engines. For those stars that made BHs, the helium core and envelope masses are indicated and, for all stars, the mass loss to winds before star death is indicated. A few stars made BHs by fallback and are also shown. Figure 20 shows the distribution of BH masses under two assumptions: (a) that only the helium core accretes, and (b) that the entire pre-SN star falls into the BH. A distribution of IMF-weighted BH frequency, calculated just as it was for neutron stars, is given in Table 4. No subtraction has been made for the mass lost to neutrinos, that is, the gravitational mass has been taken equal to the baryonic mass. It is expected that a PNS will form in all cases and radiate neutrinos until collapsing inside its event horizon. The amount of emission before trapped surface formation is uncertain, but unlikely to exceed the binding energy of the

maximum-mass neutron star, about  $0.3 M_{\odot}$  (O'Connor & Ott 2011; Steiner et al. 2013).

Assuming the entire collapse of any BH-forming star, including its hydrogen envelope, gives an upper bound to the mass of the BH formed. This limiting case is not in good agreement with the existing measurements (Wiktorowicz et al. 2014),<sup>5</sup> in terms of range and frequency of observed masses. The helium core mass seems a better indicator (Zhang et al. 2008; Kochanek 2014, 2015).

In addition to their production by stars that fail to launch a successful outgoing shock, BHs can also be made in successful explosions that experience a large amount of fallback. Only a few cases of this were found in the present survey, and the resulting BH masses were always significantly less than the helium core mass. They were made in some of the most massive stars that exploded. The weakest central engine, W20, did not produce any BHs by fallback. Cases that might have had large fallback failed to explode in the first place. The W15 series yielded only one BH with a mass of  $4.7 M_{\odot}$  produced in a star that on the main sequence was  $60 M_{\odot}$ . Series W18 produced BHs by fallback at  $27.2$  and  $27.3 M_{\odot}$  with masses of  $3.2$  and  $6.2 M_{\odot}$ . The strongest two engines, S19.8 and N20, gave a few such cases at a slightly higher mass, resulting in BHs in the range  $4.1$ – $7.3 M_{\odot}$ . In all cases, the BH mass was substantially less than the helium core mass, which ranged from  $9.2$  to  $10.2 M_{\odot}$ .

This tendency of neutrino-powered models to either explode robustly or not at all has been noted previously and naturally accounts for a substantial mass gap between the heaviest neutron stars and the typical BH mass (Uglio et al. 2012). In any successful explosion of a quite massive star (i.e., above  $12 M_{\odot}$ ), a few hundredths of a solar mass of photodisintegrated matter reassembles, yielding a lower bound to the explosion energy of a few  $\times 10^{50}$  erg (e.g., Scheck et al. 2006). On the other hand, the ejection of the hydrogen envelope and collapse of the entire helium core require that the final kinetic energy at infinity be less than about  $10^{50}$  erg (E. Lovegrove & S. E. Woosley 2015, in preparation). Given that the observations favor the implosion of the helium core, but not of the entire star (Figure 20), it seems that another mechanism is at work. One natural explanation is that the hydrogen envelope is ejected during the collapse of these massive “failures” by the Nadyozhin–Lovegrove effect (Nadezhin 1980; Lovegrove & Woosley 2013). The loss in binding energy due to neutrino emission of the PNS launches a weak shock that ejects the loosely bound envelope. If so, faint, red SNe may be a diagnostic of typical BH formation in massive stars (Lovegrove & Woosley 2013; Kochanek 2014, E. Lovegrove & S. E. Woosley 2015, in preparation).

## 6. NUCLEOSYNTHESIS

Detailed isotopic nucleosynthesis, from hydrogen to bismuth, was calculated using the KEPLER code for all the models presented in this paper, and they are included in the electronic edition in a tar.gz package. Sample output for two SNe with main-sequence masses  $14.9$  and  $25.2 M_{\odot}$  in Table 9 gives the ejected masses in solar masses in both the pre-SN winds and the explosions using the W18 engine.

Rather than discuss the yields of individual stars, however, this section gives and discusses a summary of the nucleosynthesis for the two main explosion series, N20 and W18, averaged

<sup>5</sup> <http://stellarcollapse.org/bhmasses>; retrieved 2015 September 6.

**Table 5**  
Explosion Results for the N20 and W18 Engines

Progenitor	$M_{\text{Ni}} (M_{\odot})$		$E_{\text{expl.}} (\text{B})$		$M_{\text{remnant}} (M_{\odot})$	
	N20 K P.	W18 K P.	N20 K P.	W18 K P.	N20 P.	W18 P.
12.25	0.055   0.089	0.063   0.086	1.44   1.44	1.36   1.36	1.56	1.56
12.5	0.059   0.092	0.059   0.088	1.44   1.44	1.35   1.35	1.58	1.58
12.75	0.062   0.087	0.060   0.082	1.29   1.29	1.20   1.20	1.63	1.64
13.0	0.070   0.094	0.065   0.083	1.32   1.32	1.18   1.18	1.66	1.68
13.1	0.061   0.086	0.058   0.080	1.22   1.22	1.11   1.11	1.59	1.60
13.2	0.061   0.088	0.058   0.082	1.26   1.26	1.14   1.14	1.59	1.60
13.3	0.061   0.086	0.059   0.081	1.22   1.22	1.12   1.12	1.60	1.61
13.4	0.063   0.086	0.061   0.081	1.21   1.21	1.12   1.12	1.61	1.62
13.5	0.064   0.093	0.062   0.087	1.33   1.33	1.23   1.23	1.61	1.62
13.6	0.073   0.104	0.070   0.097	1.51   1.51	1.38   1.38	1.62	1.64
13.7	0.071   0.103	0.068   0.096	1.48   1.48	1.35   1.35	1.63	1.64
13.8	0.072   0.101	0.069   0.096	1.43   1.43	1.33   1.33	1.65	1.66
13.9	0.071   0.097	0.069   0.091	1.36   1.36	1.27   1.27	1.66	1.67
14.0	0.070   0.097	0.068   0.091	1.36   1.36	1.27   1.27	1.67	1.68
14.1	0.069   0.094	0.067   0.089	1.30   1.30	1.24   1.23	1.69	1.69
14.2	0.067   0.090	0.066   0.086	1.25   1.25	1.20   1.19	1.69	1.70
14.3	0.072   0.096	0.068   0.089	1.31   1.31	1.21   1.21	1.70	1.71
14.4	0.070   0.090	0.069   0.088	1.22   1.22	1.19   1.19	1.72	1.72
14.5	0.077   0.089	0.077   0.088	1.09   1.09	1.07   1.07	1.76	1.76
14.6	0.072   0.090	0.071   0.086	1.17   1.17	1.13   1.13	1.75	1.75
14.7	0.079   0.089	0.078   0.086	1.07   1.07	1.01   1.01	1.77	1.78
14.8	0.072   0.085	0.071   0.083	1.07   1.07	1.05   1.05	1.78	1.78
14.9	0.076   0.088	0.075   0.085	1.07   1.07	1.04   1.04	1.78	1.78
15.2	0.070   0.082	0.071   0.079	0.94   0.94	0.83   0.83	1.55	1.57
15.7	0.075   0.086	0.075   0.081	0.95   0.95	0.81   0.81	1.57	1.59
15.8	0.085   0.097	0.074   0.074	1.06   1.06	0.65   0.65	1.56	1.64
15.9	0.079   0.079		0.70   0.70		1.67	...
16.0	0.094   0.110	0.075   0.079	1.26   1.26	0.78   0.78	1.54	1.62
16.1	0.075   0.084	0.078   0.087	0.89   0.89	0.97   0.97	1.59	1.59
16.2	0.095   0.111	0.076   0.081	1.23   1.23	0.79   0.79	1.55	1.62
16.3	0.097   0.113	0.078   0.083	1.23   1.23	0.80   0.80	1.55	1.62
16.4	0.093   0.110	0.075   0.079	1.24   1.24	0.76   0.76	1.55	1.63
16.5	0.093   0.110	0.075   0.078	1.23   1.23	0.75   0.75	1.55	1.63
16.6	0.097   0.112	0.078   0.082	1.22   1.22	0.78   0.78	1.56	1.63
16.7	0.096   0.111	0.077   0.081	1.23   1.22	0.78   0.78	1.55	1.62
16.8	0.096   0.112	0.078   0.082	1.22   1.22	0.77   0.77	1.57	1.64
16.9	0.095   0.111	0.077   0.080	1.22   1.22	0.75   0.75	1.57	1.64
17.0	0.093   0.110	0.075   0.078	1.21   1.21	0.73   0.73	1.57	1.65
17.1	0.095   0.111	0.077   0.079	1.21   1.21	0.74   0.74	1.58	1.66
17.3	0.089   0.097	0.078   0.076	0.98   0.98	0.65   0.65	1.61	1.67
17.4	0.088   0.097	0.077   0.075	0.98   0.98	0.64   0.64	1.60	1.67
17.5	0.086   0.096	0.075   0.074	0.99   0.99	0.63   0.63	1.59	1.66
17.6	0.088   0.097	0.077   0.075	0.98   0.98	0.63   0.63	1.60	1.67
17.7	0.085   0.090		0.80   0.80		1.63	...
17.9	0.079   0.101	0.077   0.097	1.36   1.35	1.27   1.27	1.77	1.78
18.0	0.081   0.070		0.51   0.51		1.72	...
18.1	0.078   0.097	0.077   0.093	1.28   1.28	1.22   1.22	1.79	1.79
18.2	0.078   0.099	0.076   0.095	1.33   1.33	1.25   1.25	1.77	1.77
18.3	0.079   0.095	0.077   0.091	1.23   1.23	1.14   1.14	1.81	1.82
18.4	0.079   0.094	0.077   0.090	1.19   1.18	1.10   1.10	1.82	1.83
18.5	0.083   0.097	0.071   0.072	1.01   1.01	0.62   0.62	1.57	1.64
18.7	0.078   0.084		0.79   0.79		1.63	...
18.8	0.095   0.095		0.83   0.83		1.78	...
18.9	0.089   0.081		0.65   0.65		1.83	...
19.0	0.084   0.073		0.58   0.58		1.83	...
19.1	0.087   0.078		0.64   0.64		1.82	...
19.2	0.096   0.111	0.077   0.079	1.19   1.19	0.77   0.77	1.62	1.70
19.3	0.075   0.099	0.065   0.080	1.26   1.26	0.96   0.96	1.50	1.54

**Table 5**  
(Continued)

Progenitor	$M_{\text{Ni}} (M_{\odot})$		$E_{\text{expl. (B)}}$		$M_{\text{remnant}} (M_{\odot})$	
	N20 K. P.	W18 K. P.	N20 K. P.	W18 K. P.	N20 P.	W18 P.
19.4	0.071   0.066		0.51   0.51		1.67	...
19.7	0.058   0.117	0.055   0.107	1.88   1.88	1.70   1.70	1.37	1.38
19.8	0.075   0.133	0.072   0.124	1.96   1.95	1.78   1.78	1.44	1.46
20.1	0.122   0.141	0.098   0.102	1.37   1.36	0.82   0.82	1.72	1.82
20.2	0.062   0.121	0.060   0.112	1.92   1.92	1.75   1.75	1.43	1.44
20.3	0.112   0.148	0.091   0.115	1.72   1.72	1.25   1.25	1.50	1.57
20.4	0.057   0.116	0.054   0.107	1.87   1.87	1.70   1.70	1.38	1.40
20.5	0.053   0.113	0.052   0.104	1.84   1.84	1.67   1.67	1.37	1.38
20.6	0.086   0.080		0.59   0.59		1.90	...
20.8	0.056   0.053	0.056   0.054	0.45   0.45	0.48   0.48	1.75	1.74
21.0	0.086   0.107	0.075   0.087	1.26   1.26	0.92   0.92	1.51	1.56
21.1	0.087   0.105	0.078   0.088	1.21   1.20	0.91   0.91	1.55	1.60
21.2	0.060   0.057	0.059   0.056	0.59   0.59	0.59   0.59	1.92	1.92
21.5	0.102   0.113	0.083   0.083	1.12   1.12	0.70   0.70	1.62	1.70
21.6	0.106   0.115	0.077   0.068	1.10   1.10	0.52   0.52	1.64	1.76
21.7	0.094   0.091		0.71   0.71		1.80	...
25.2	0.110   0.128	0.122   0.142	1.19   1.18	1.31   1.31	1.80	1.77
25.3	0.138   0.152		1.10   1.10		1.88	...
25.4	0.127   0.150	0.105   0.116	1.36   1.35	0.86   0.86	1.79	1.88
25.5	0.113   0.130	0.123   0.143	1.20   1.19	1.30   1.30	1.80	1.77
25.6	0.088   0.105	0.091   0.108	1.09   1.08	1.05   1.05	1.78	1.78
25.7	0.071   0.120	0.069   0.111	1.66   1.65	1.49   1.48	1.60	1.61
25.8	0.068   0.118	0.065   0.109	1.68   1.67	1.49   1.49	1.58	1.59
25.9	0.108   0.133	0.116   0.139	1.26   1.26	1.28   1.28	1.68	1.67
26.0	0.122   0.151	0.125   0.152	1.40   1.39	1.32   1.31	1.67	1.68
26.1	0.129   0.155	0.108   0.119	1.40   1.39	0.94   0.94	1.68	1.76
26.2	0.130   0.157	0.112   0.125	1.39   1.39	0.99   0.99	1.69	1.76
26.3	0.146   0.171	0.112   0.118	1.39   1.38	0.78   0.78	1.71	1.82
26.4	0.128   0.141	0.125   0.134	1.09   1.08	0.82   0.82	1.77	1.84
26.5	0.125   0.138	0.120   0.128	1.06   1.05	0.84   0.84	1.77	1.82
26.6	0.131   0.147		1.13   1.12		1.75	...
26.7	0.131   0.146		1.10   1.10		1.76	...
26.8	0.137   0.150		1.10   1.10		1.76	...
26.9	0.135   0.147		1.10   1.10		1.75	...
27.0	0.129   0.141	0.089   0.092	1.09   1.08	0.59   0.59	1.72	1.85
27.1	0.134   0.144	0.101   0.102	1.08   1.08	0.61   0.61	1.73	1.86
27.2	0.127   0.143	0.006   0.000	1.08   1.08	0.57   0.56	1.73	3.19
27.3	0.133   0.146	0.006   0.000	1.09   1.09	0.41   0.41	1.73	6.24
27.4	0.003   0.000		0.53   0.53		4.96	...
29.0	0.005   0.000		0.52   0.52		4.14	...
29.1	0.004   0.000		0.51   0.51		4.43	...
29.2	0.001   0.000		0.36   0.36		6.94	...
29.6	0.001   0.000		0.35   0.35		7.30	...
60	0.079   0.095	0.065   0.066	0.92   0.92	0.65   0.65	1.70	1.80
80	0.078   0.079		0.54   0.54		1.91	...
100	0.074   0.079		0.62   0.62		2.03	...
120	0.079   0.092	0.048   0.066	1.04   1.01	0.67   0.67	1.70	1.76

**Note.** K. = KEPLER and P. = P-HOTB. The remnant masses are listed only for the P-HOTB calculations since they are almost always identical to those of KEPLER.

over an IMF. To give an indication of the variation with mass, separate results are given for three mass ranges: 9–12  $M_{\odot}$ , 12–30  $M_{\odot}$ , and 30–120  $M_{\odot}$ . These ranges are chosen to represent the qualitatively different nature (Section 2.3) of SN progenitors with very compact core structures (first group), SNe that have actually made most of the elements

(second group), and events where mass loss or an uncertain IMF plays a key role (third group). At the end, we also summarize the total nucleosynthesis (9–120  $M_{\odot}$ ) and consider the effect of adding an SN Ia component to pick up deficiencies in iron-group and intermediate-mass element production (Section 6.5).

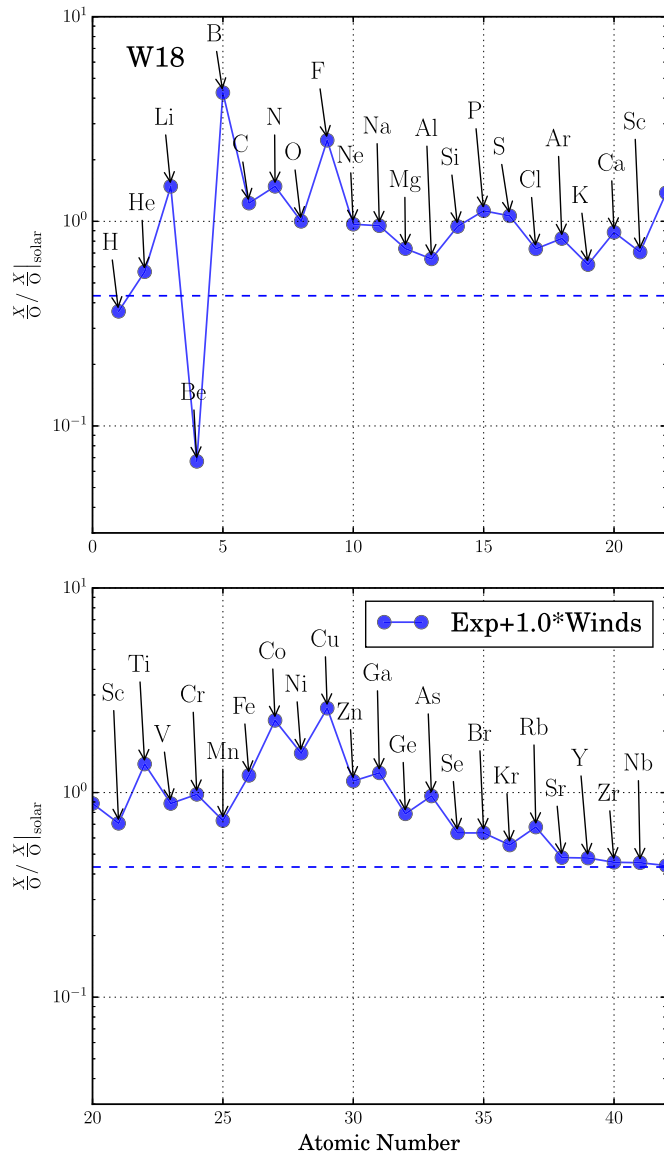


**Figure 21.** Nucleosynthesis in low-mass SNe. The IMF-averaged yields of just the explosions from  $9$  to  $12 M_{\odot}$  are given for the elements from hydrogen through niobium. The calculations actually included elements up to bismuth ( $Z = 83$ ), but no appreciable production occurred for the heavier elements. Production factors (defined in the text) have been normalized to that of  $^{16}\text{O}$ , which is 2.37, by dividing them all by this factor, making the oxygen production unity. The dashed line at  $(2.37)^{-1} = 0.43$  is thus a line of no net change. Elements below the dashed line are destroyed in the star; those above it experience net production. The relatively large yields of iron-group elements, which are nearly solar compared to oxygen, are a consequence of the low oxygen yield in these light SNe and do not characterize heavier stars where more nucleosynthesis happens. The s-process just above the iron group is significantly underproduced. Note, however, the large yields of Li and B produced by the neutrino process. Fluorine is also overproduced by a combination of neutrinos and helium burning. Stellar winds of all models have been included.

To proceed, the yields of each star,  $M_i$ , are separated into two categories: those species produced in the winds of the star during its pre-SN evolution, and those ejected during the SN itself (only wind for the imploded stars). For each star, these yields, in solar masses, are multiplied by the fractional area under a Salpeter (1955) IMF that describes the number of stars in each bin between  $M_i$  and  $M_{i+1}$ . The area has been normalized so that the total area under the IMF curve from  $9$  to  $120 M_{\odot}$  is 1. Summing

the results across a mass range provides the average ejecta, in solar masses per massive star within that range.

A characteristic mass fraction is then computed that is the ratio of the IMF-weighted ejected mass of a given element (or isotope) produced in a mass range divided by the total mass of all species ejected. The computation may or may not include the wind; both cases are considered. The production factor is then the ratio of this mass fraction to the corresponding mass fraction in the Sun (Lodders 2003).

Defined in this way, a production factor of 1 implies no change in the mass fraction of an isotope from the star or mass range considered compared to the pre-SN progenitor. What came in is what goes out. The net production of a given species is proportional to  $1 - P$ . There is also a change in all species since some mass stays behind in the bound remnant and is lost. This is not accounted for in the definition used here for  $P$ . If half of the mass of the star is lost to the remnant, but the mass ejected from the star is all of exactly solar composition, the production factor by our definition is still 1, but the *net* production would be this factor times  $(M_{\text{ZAMS}} - M_{\text{rem}})/M_{\text{rem}} = 1/2$ . Values of remnant masses are given in Tables 7 and 8. As currently designed, the production factor can only be less than 1 if the species is destroyed by nuclear reactions (e.g., deuterium, beryllium).

For purposes of presentation, all production factors are divided by that of  $^{16}\text{O}$  so that the production factor of  $^{16}\text{O}$ , an abundant element known to be produced in massive stars, is 1. To retain information about the unnormalized production factor, a line is given in each figure at the reciprocal of the unnormalized production factor of  $^{16}\text{O}$ . Points lying on this line have no net production, i.e., have an unnormalized production factor of 1.

In order to demonstrate the dependence on uncertain mass-loss rates, especially in the heavier stars, some yields are presented with and without mass loss. The “without-mass-loss results” are an artificial construct because we have not carried out a self-consistent evolution and explosion of constant-mass stars. The explosion of such stars would be quite different. For example, the more massive stars would all make BHs. The less massive ones might explode and eject the same matter the wind would have removed. Here the mass lost in the wind is simply discarded. The effect of removing it shows its importance.

In those calculations that include the wind, the mass loss of all stars has been added, including those that end up making BHs. All stars have winds; only those that explode have SN ejecta. The tricky issue of how to treat the hydrogen envelope of stars that form BHs but are presumed (not calculated) to eject their residual envelopes is deferred to a later section (Section 6.4.5).

Because of the lower bound on the mass,  $9 M_{\odot}$ , no contribution from lighter stars is included here, so it is to be expected that species like the heavy s-process,  $^{13}\text{C}$ ,  $^{14}\text{N}$ , etc., which are known to be efficiently produced in asymptotic giant branch stars, will be underrepresented. Any r-process from merging neutron stars or the neutrino wind is also missing, as are the products of cosmic-ray spallation.

Some interesting statistics relevant to nucleosynthesis are given in Table 5. For the W18 and N20 series, the typical SN mass, based only on those stars that actually exploded, is given along with the fraction of the total ejecta that come from each mass range.

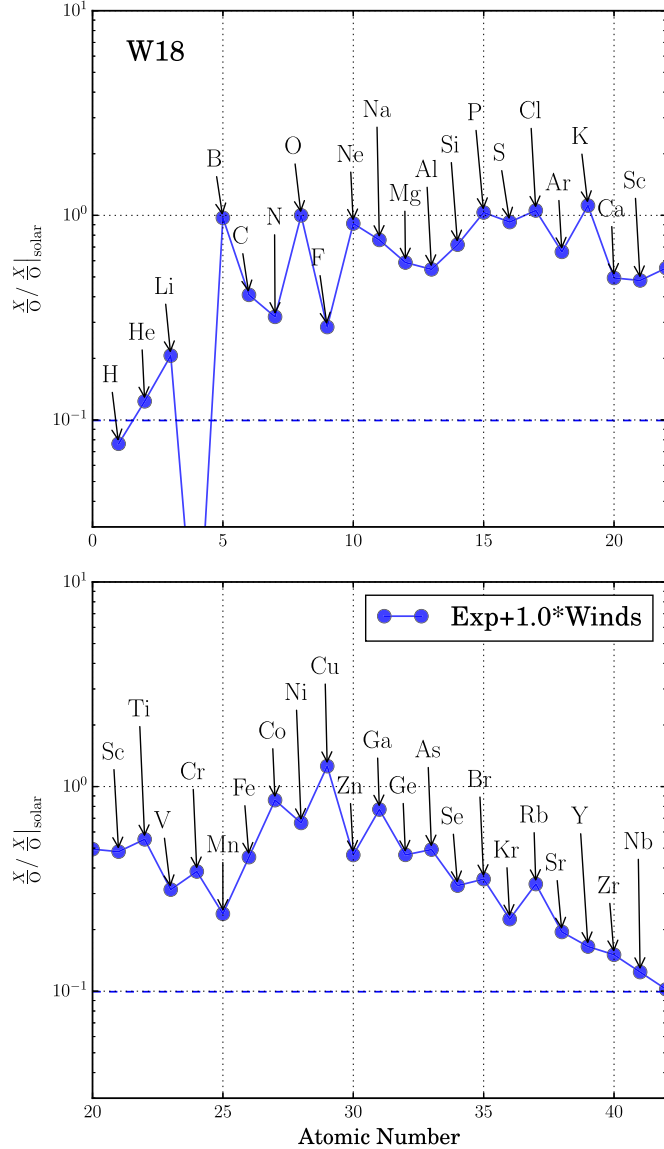


**Figure 22.** Similar to Figure 21, the IMF-averaged production of elements in SNe from  $12$  to  $30 M_{\odot}$  is shown using the W18 calibration for the central engine. This is the range of masses where most SN nucleosynthesis occurs. The production factor of oxygen before normalization was 10. Production factors above the dashed line at 0.10 thus indicate net nucleosynthesis in the stars considered. The production of iron-group elements is substantially lower than in Figure 21, but will be supplemented by SNe Ia. The production of light *s*-process elements is substantially greater, but still inadequate to explain their solar abundances. Production of Li and B by the neutrino process is diminished, but still significant, especially for B. Contributions to nucleosynthesis by the winds of all stars, including those that became BHs, are included.

### 6.1. $9$ – $12 M_{\odot}$

While roughly half of all observed SNe lie within this range (Table 4), their contribution to the overall stellar nucleosynthesis is relatively small. Figure 21 shows reasonably good agreement with solar system elemental abundances for elements heavier than beryllium ( $Z=4$ ) all the way through the iron group, but this can be misleading since a lot of the yield was in the star to begin with in solar proportions. The actual production factor for oxygen, before renormalization, is 2.37, so a value of  $1/2.37 = 0.422$  in the figure indicates no net change in the abundance due to stellar nucleosynthesis. This is apparent for

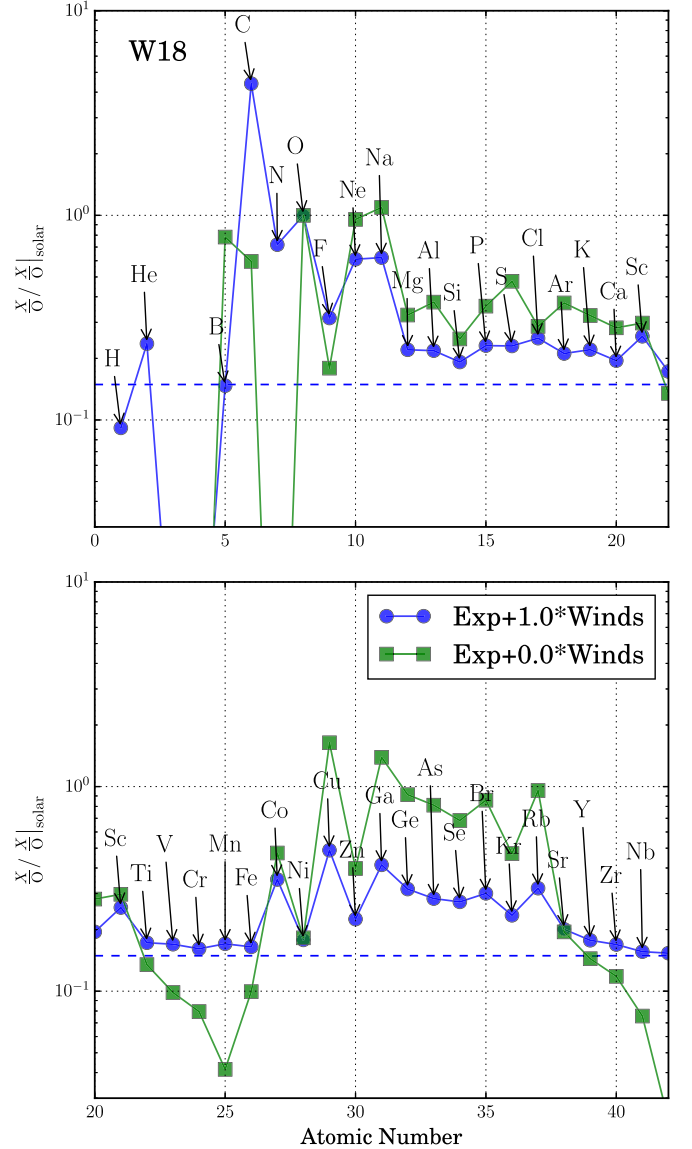


**Figure 23.** Similar to Figure 21, the IMF-averaged production of the elements is shown for stars from  $30$  to  $120 M_{\odot}$ , using the W18 calibration for the central engine. Most, though not all, stars in this very massive range become BHs, so their nucleosynthesis is dominated by the winds that they eject before dying. Production factors are normalized to oxygen. If winds are included, net production of an element occurs in this mass range if its average production factor is above 0.15 (blue dashed line). Also shown are the production factors if the wind is discarded. Since oxygen was being appreciably synthesized in the winds, neglecting them results in an overall renormalization of all production factors. The cutoff for the net production without winds falls to 0.010, off the scale of the plot. Including winds, these stars make so much carbon, nitrogen, and oxygen that they can be responsible for little else.

the heaviest elements plotted, around  $Z=40$ . To the extent that other elements have the same production factor as oxygen, their abundance is also about 2.37 times greater than what the star had, external to its final gravitationally bound remnant, at birth.

Figure 21 reveals some interesting systematics for low-mass SNe, though. First, the abundances *are* roughly solar, even for the iron group. Some elements (Co, Ni, and Cu) are even overproduced. This is surprising given that only a minor fraction of iron-group elements is expected to come from massive stars (e.g., Timmes et al. 1995; Cayrel et al. 2004). More should come from SNe Ia. Their apparent large

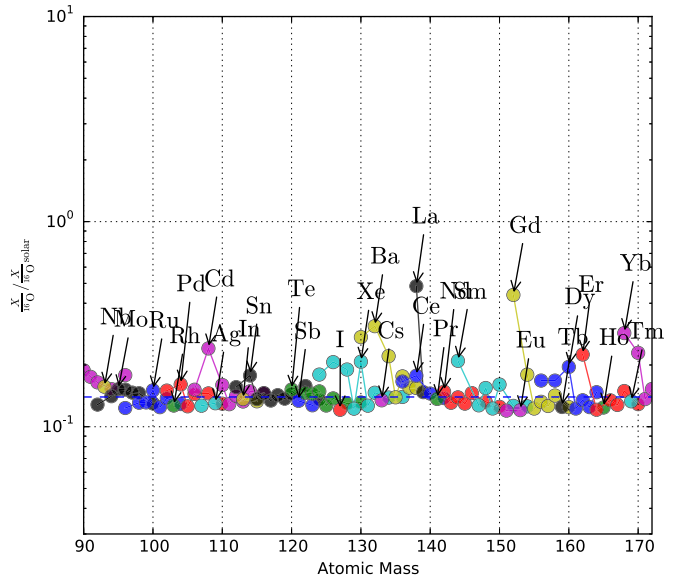
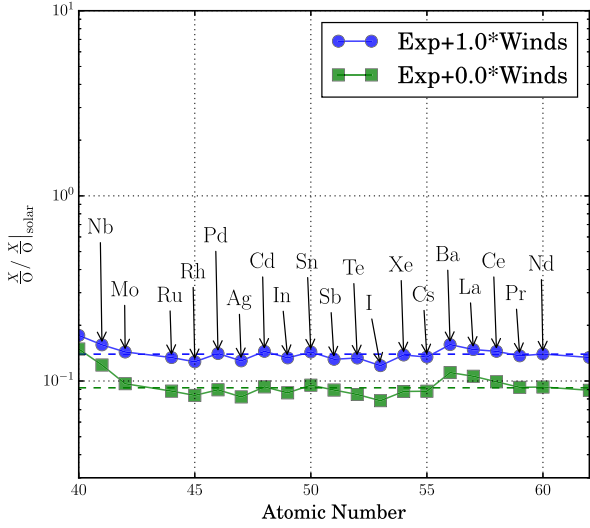
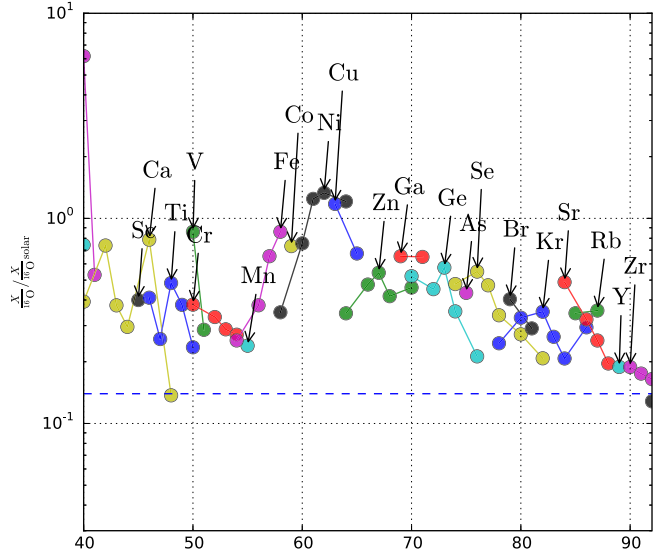
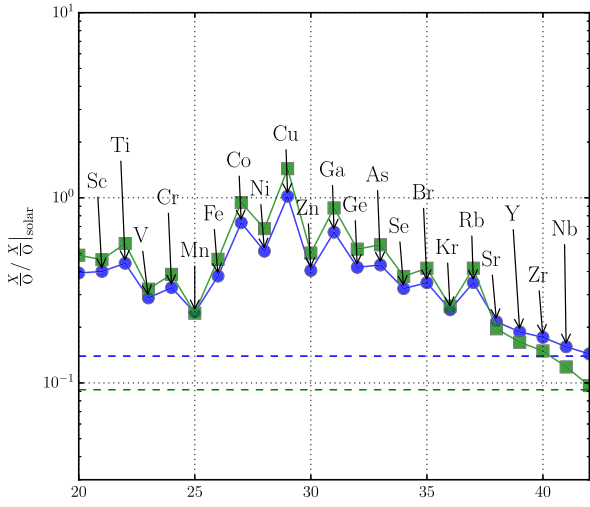
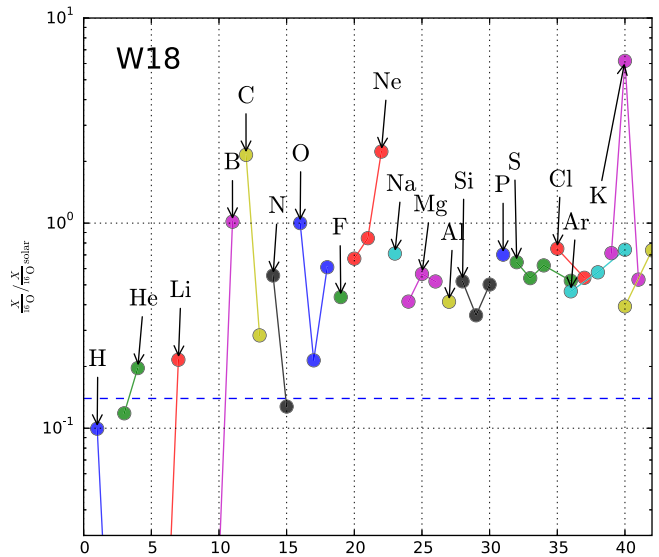
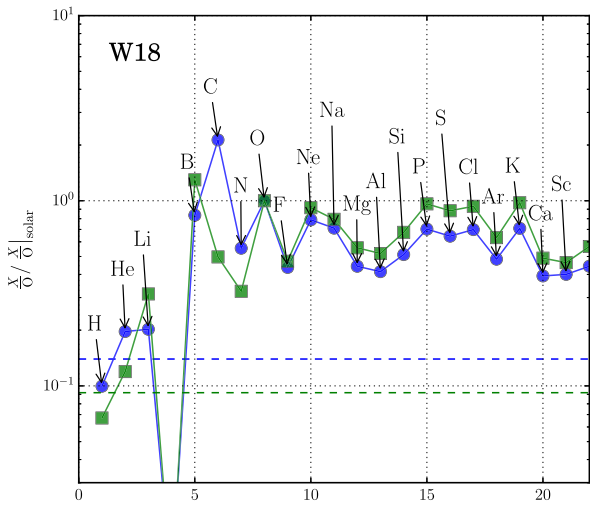


**Figure 24.** Integrated nucleosynthesis of the elements for all stars considered ( $9-120 M_{\odot}$ ) using the W18 central engine. The results have been normalized to oxygen, and the dashed line shows net production occurring for production factors bigger than 0.14 if winds are included, 0.092 if they are not. The displacement of the overall normalization is due to the production of oxygen itself in winds. While individual isotopes may be affected (Figure 25), no net nucleosynthesis occurs for elements above  $Z = 40$ .

**Figure 25.** Same yields as in Figure 24 for the W18 central engine including the wind, but now given for the individual isotopes of each element.

production here really just reflects the fact that these stars make very little oxygen. As we shall see later, massive stars altogether make only about one-quarter of solar iron. Still it is an interesting prediction that iron to oxygen in the remnants of low-mass SN remnants may be roughly solar.

By the same token, the production of carbon and nitrogen is not generally attributed to massive stars, but they do have slightly supersolar proportions to oxygen in this mass range. Nitrogen, which is made in the hydrogen envelope by the CNO cycle operating in a large mass on primordial C and O, seems large here because oxygen, made by helium burning in a relatively thin shell, is small. Overall, we shall find that nitrogen, at least nowadays, is probably not a massive star product, though the component coming from massive stars is appreciable. The case of carbon is less clear and depends on mass-loss rates and the IMF.

Also quite abundant in Figure 21 are lithium, boron, and fluorine.  $^7\text{Li}$  and  $^{11}\text{B}$  are made by the neutrino process (Woosley et al. 1990). The assumed temperature of the  $\mu$  and  $\tau$  neutrinos here was 6 MeV. The large production of  $^{11}\text{B}$  here reflects the large carbon abundance in these lower-mass stars and the proximity of the carbon shell to the collapsing iron core that emits the neutrinos.  $^7\text{Li}$  is made by the spallation of  $^4\text{He}$  by  $\mu$ - and  $\tau$ -neutrinos by the reaction sequence  $^4\text{He}(\nu, \nu'n)^3\text{He}(\alpha, \gamma)^7\text{Be}$ . Its large production (again compared with a small oxygen abundance) reflects the proximity of the helium shell to the core and the importance of the alpha-rich freeze-out in the bottom-most layers ejected. Flourine is made by a combination of the neutrino irradiation of neon and helium burning (Meynet & Arnould 1993), with the former making most of the  $^{19}\text{F}$  above  $15 M_{\odot}$ , but the latter dominating for lower mass supernovae (see also Sieverding et al 2015), and slightly dominant overall. The synthesis of  $^{19}\text{F}$  by neutrinos is primary, however, since the target is  $^{20}\text{Ne}$ , while the synthesis by helium burning depends upon the abundance of  $^{14}\text{N}$  and neutrons and is therefore secondary. The production of fluorine by helium burning will thus be reduced in lower-metallicity stars.

The low production of Be reflects its destruction in massive stars;  $^9\text{Be}$  and  $^{10}\text{B}$  are thought to be produced by cosmic-ray spallation.

## 6.2. $12-30 M_{\odot}$

Stars from 12 to  $30 M_{\odot}$  are responsible for most of the nucleosynthesis that happens in SNe. Figure 22 shows the production factors for this range. The intermediate-mass elements are made in roughly solar relative proportions compared with oxygen, though the low yield of calcium is a concern. That the iron-peak elements are deficient is not surprising. Most of iron comes from SNe Ia. Some species in the iron group, especially Co, Ni, and Cu, are produced here in roughly solar proportions. All are made in the alpha-rich freeze-out:  $^{58}\text{Ni}$  as itself, and  $^{59}\text{Co}$  and  $^{63,65}\text{Cu}$  as  $^{59}\text{Cu}$ ,  $^{63}\text{Ga}$ , and  $^{65}\text{Ge}$ , respectively. Production of these species is sensitive to the treatment of the inner boundary and the neutrino reactions that might go on there, changing the value of  $Y_e$ . The calculated production here is thus more uncertain than for other species.

The production of Li, B, C, N, and F has declined greatly from the large values seen for the lower-mass SNe. This is mostly to do with the larger oxygen production to which these

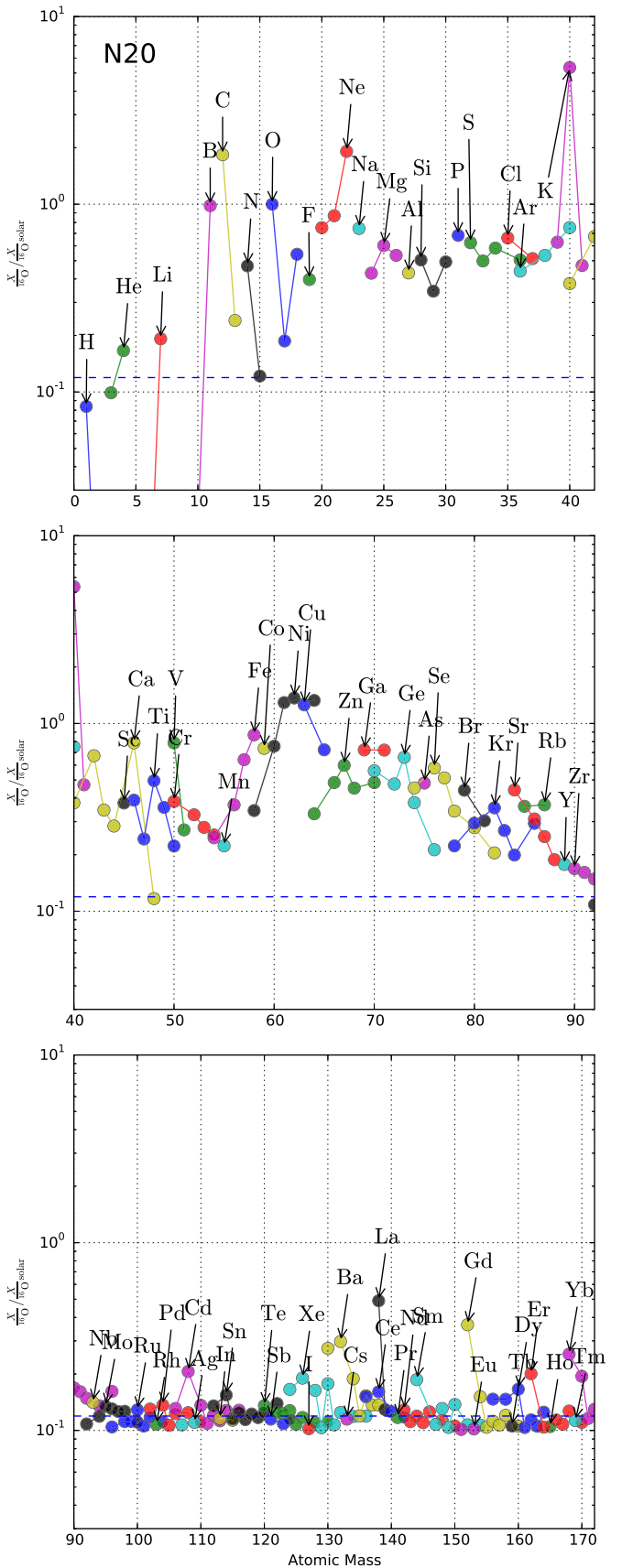


**Figure 26.** Similar to Figure 25, this figure gives results using the N20 central engine instead of W18. There are no significant differences.

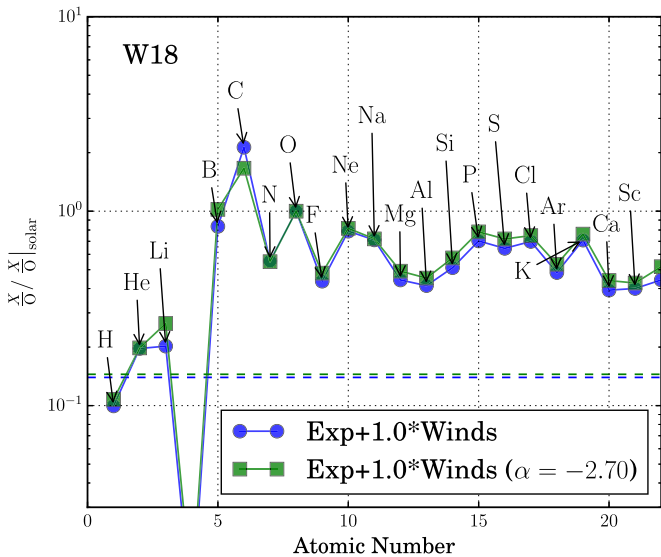


**Figure 27.** Similar to Figure 24, but using a steeper mass dependence for the IMF. Here the results of using a Salpeter IMF with a power-law dependence of  $-2.35$  are compared to those obtained using a slope of  $-2.7$ . The dashed lines here indicate net production for both ensembles at  $0.14$ .

yields are now normalized, but also to the lower carbon abundance and larger radii of the carbon and helium shells.

Of particular note in this mass range is a significant underproduction of *s*-process elements, especially Sc and the elements just above the iron group. This problem will persist in the final integrated nucleosynthesis from all masses and is a challenge for the present models and approach. Part of this deficiency may be due to an uncertain reaction rate for  $^{22}\text{Ne}(\alpha, n)^{25}\text{Mg}$  (Section 6.4.4).

### 6.3. $30\text{--}120 M_{\odot}$

Most stars above  $30 M_{\odot}$  in the present study become BHs, and their remnants absorb most of the core-processed elements. Their winds will escape prior to collapse, however, and contribute to nucleosynthesis, especially of the lighter elements like CNO. For the assumed mass-loss rates, some of the heaviest stars in this range (i.e., from  $60 M_{\odot}$  upward) also explode, but only because winds have stripped the core of the star down to a manageable size. Such stars, having carbon–oxygen cores comparable to stars in the  $12\text{--}39 M_{\odot}$  range, will contribute similar nucleosynthesis, but more enhanced in the products of helium burning.

Figure 23 shows that the winds contain excesses of  $^4\text{He}$ , both from the envelopes of these massive stars that have been enriched by hydrogen burning and convective dredge-up and from the winds of Wolf–Rayet stars that have lost their envelopes altogether. This production significantly augments the primordial helium in the original star from the big bang and previous generations of stars. The nuclei  $^{12,13}\text{C}$ ,  $^{14}\text{N}$ , and  $^{16,18}\text{O}$  are also significantly enriched, but  $^{15}\text{N}$  and  $^{17}\text{O}$  are not.  $^{22}\text{Ne}$  is greatly enhanced owing to Wolf–Rayet winds. This nucleus comes from two alpha captures on  $^{14}\text{N}$  and is abundant in the helium shell from convective helium burning. The *s*-process up to Rb is also produced in the winds of these very massive stars, but its production is still inadequate to explain its abundance in the Sun when the lighter stars are folded in. Intermediate-mass elements are underproduced compared with the large oxygen synthesis in the winds.

### 6.4. Integrated Yields from Massive Stars $9\text{--}120 M_{\odot}$

The integrated production factors from massive stars of all masses above  $9 M_{\odot}$  are shown in Figure 24 summed over isotopes. The individual isotopic abundances are given in Figure 25. The integrated production factor is calculated from a combined weighting of the three mass ranges just discussed. If  $P_{\text{low}}$  is the production factor for stars  $9\text{--}12 M_{\odot}$ ,  $P_{\text{mid}}$  is for stars  $12\text{--}30 M_{\odot}$ , and  $P_{\text{high}}$  is for stars  $30\text{--}120 M_{\odot}$ , the total production factor,  $P_{\text{tot}}$ , is

$$P_{\text{tot}} = f_1 P_{\text{low}} + f_2 P_{\text{mid}} + f_3 P_{\text{high}}, \quad (11)$$

where  $f_i$  is given in Table 5. Because  $P_{\text{low}}$  is generally low and  $P_{\text{high}}$  is low except for species produced in the winds like CNO, the total production for most elements is dominated by  $P_{\text{mid}}$ .

The probable nucleosynthetic sites for producing the various isotopes heavier than lithium have been summarized in Table 3 of Woosley et al. (2002), and our discussion follows that general delineation and omits references given there. We also include the full integrated yield of the N20 series in Figure 26. The primary difference is that the N20 model produces a bit more  $^{16}\text{O}$ , which can be seen by comparing the baseline solar abundance of the heavy isotopes.

Additionally, one could vary the power of the IMF. Lowering the power from that of a Salpeter IMF of  $-2.35$  to a value as low as  $-2.7$  affects the results in a similar way to a reduction in the contributions of mass-loss rates. The value of  $-2.7$  was chosen as being a low value within the known uncertainties (e.g., Scalo 1986; Chabrier 2003). The results in Figure 27 show that a steeper IMF acts in the same way as reducing the contributions from the winds of very heavy stars, but with a smaller effect.

#### 6.4.1. Light Elements—Lithium through Aluminum

While perhaps not widely recognized, massive stars can make an important, though not dominant, contribution to the abundance of  $^7\text{Li}$  (though not  $^6\text{Li}$ ). The  $^7\text{Li}$  is made mostly by the neutrino process, which spalls helium in the deeper layers to make  $^3\text{He}$ , which combines with  $^4\text{He}$  to make  $^7\text{Li}$  (after a decay). Some  $^3\text{He}$  is also made in the hydrogenic envelope. The total contribution to each is about 20% of their solar value.  $^6\text{Li}$ ,  $^9\text{Be}$ , and  $^{10}\text{B}$  must be made elsewhere, perhaps by cosmic-ray spallation.

$^{11}\text{B}$ , on the other hand, is abundantly produced by the neutrino process. Spallation of carbon by  $\mu$ - and  $\tau$ -neutrinos produces the isotope in the carbon shell. Without neutrinos,  $^{11}\text{B}$  would be greatly underproduced. Its abundance in the Sun thus provides a useful thermometer for measuring the typical temperature of the neutrinos (though their spectrum varies significantly from thermal). The assumed temperature of the neutrinos here was 6 MeV. A slightly smaller value would have sufficed, but larger values are ruled out.

Carbon, perhaps surprisingly, is adequately produced in massive stars, but the yield is very sensitive to the treatment of mass loss and, to a lesser extent, the IMF (Figure 27). Too much carbon is made for the mass-loss rates assumed here (see also Maeder 1992), but a mass-loss rate half as large is certainly allowed and would produce carbon nicely. In the unrealistic case of no mass loss, only about one-third of carbon would be made in massive stars. Care should be taken though because folding the yields from a population of solar-metallicity stars with an IMF is very approximate compared

**Table 6**  
Integrated Statistics (see Section 6.4 for Descriptions; All Masses in  $M_{\odot}$ )

Cal.	$\bar{E}$ (erg)	$\bar{M}_b$	$\bar{M}_g$	Lower $\bar{M}_{\text{BH}}$	Upper $\bar{M}_{\text{BH}}$	$\bar{M}_{\text{Ni}, l}$	$\bar{M}_{\text{Ni}, u}$	SN%	(>12)	(>20)	(>30)
W15.0	0.68	1.55	1.40	8.40	13.3	0.040	0.049	66	47	8	2
W18.0	0.72	1.56	1.40	9.05	13.6	0.043	0.053	67	48	9	2
W20.0	0.65	1.54	1.38	7.69	13.2	0.036	0.044	55	37	3	0
N20.0	0.81	1.56	1.41	9.23	13.8	0.047	0.062	74	52	13	5

with a full model for galactic chemical evolution. Lower-metallicity massive stars would presumably have diminished winds and would make less carbon. The isotope  $^{13}\text{C}$  is always underproduced in massive stars and is presumably made in the winds and planetary nebulae of lower-mass stars.

Nitrogen too is underproduced and needs to be mostly made elsewhere. Presumably  $^{14}\text{N}$  is made by the CNO cycle in lower-mass stars and  $^{15}\text{N}$  is made in classical novae by the hot CNO cycle.

Oxygen is the normalization point, and both  $^{16}\text{O}$  and  $^{18}\text{O}$  are copiously produced, both by helium burning. The yield of  $^{18}\text{O}$  is sensitive to the metallicity, but that of  $^{16}\text{O}$  is not directly, though it is sensitive by way of the mass loss.  $^{17}\text{O}$  is not made owing to its efficient destruction by  $^{17}\text{O}(p, \alpha)^{14}\text{N}$ . Perhaps it too is made in classical novae.

Fluorine is somewhat underproduced in the overall ensemble, despite having a very substantial production by the neutrino process and helium burning in low-mass stars.

The abundance of neon is uncertain in the Sun, but  $^{20}\text{Ne}$  and  $^{21}\text{Ne}$  are well produced and  $^{22}\text{Ne}$  is overproduced. The synthesis of  $^{22}\text{Ne}$  depends on the initial metallicity of the star, however, since CNO is converted into  $^{22}\text{Ne}$  during helium burning. Lower-metallicity stars would make less, and the abundance of  $^{22}\text{Ne}$  might come down in a full study of galactic chemical evolution. The yield of  $^{22}\text{Ne}$  is also sensitive to mass loss, more so than  $^{20}\text{Ne}$  and  $^{21}\text{Ne}$ , and lower metallicity would imply lower mass loss.

All isotopes of sodium, magnesium, and aluminum are produced reasonably well by carbon and neon burning. Magnesium and aluminum are a little deficient, however, and this is the beginning of a trend that persists through the intermediate-mass elements. It could reflect a systematic underestimate of the CO core size due to the neglect of rotation or inadequate overshoot mixing, since these isotopes will be produced in greater abundances in larger CO cores, but increasing the core size might make the stars harder to blow up. Or it may indicate an incompleteness in the present approach. Many of the stars that made BHs here would have contributed to the intermediate-mass elements. Perhaps rotation or other multidimensional effects on the explosion play a role?

#### 6.4.2. Intermediate-mass Elements—Silicon through Scandium

The major isotopes of the intermediate-mass elements from silicon through calcium are consistently co-produced in solar proportions. The total mass of these, however, is about 12% of that of  $^{16}\text{O}$ , which is only half the solar value of 22%. A similar underproduction was seen by Woosley & Heger (2007) (their Figure 8), so it is not solely a consequence of the new approach. Part of the difference might be picked up by SNe Ia, which, aside from being prolific sources of iron, can also produce a significant amount of intermediate-mass elements (Iwamoto et al. 1999, and Section 6.5). Still, the systematic

underproduction of so many species generally attributed to massive stars is troubling. Better agreement between intermediate-mass element and oxygen productions existed in earlier studies (Timmes et al. 1995; Woosley et al. 2002), which used a larger solar abundance for  $^{16}\text{O}$ .

Several isotopes with particularly anomalous production in this mass range warrant mention.  $^{40}\text{K}$  is greatly overproduced compared even with the abundance in the zero-age sun. The difference presumably reflects the lengthy time in which decay occurred between the last typical SN and the Sun's birth.  $^{44}\text{Ca}$  is underproduced in massive stars. Presumably it is made by sub-Chandrasekhar mass models for SNe Ia (Section 6.5).  $^{48}\text{Ca}$ , along with several neutron-rich iron-group nuclei like  $^{50}\text{Ti}$  and  $^{54}\text{Cr}$ , is presumably made in a neutron-rich nuclear statistic equilibrium as might exist in a rare variety of SNe Ia igniting at high density.  $^{45}\text{Sc}$  is due to the *s*-process, and its underproduction is a portent of problems to come (Section 6.4.4).

#### 6.4.3. The Iron Group

The iron yields here were calibrated to be the maximum calculated in P-HOTB (Tables 7 and 8), where it was assumed that the neutrino wind makes an appreciable contribution. This was one of the agreements forced on the KEPLER recalculation (Figure 12).

As expected, even taking this upper bound, the iron group is severely underproduced in massive stars, since most of the iron in the Sun has been made by SNe Ia. In the next section, we shall consider the consequences of combining both varieties of SNe. The ratio of the mass of new iron made here as  $^{56}\text{Ni}$  to new oxygen (neglecting the initial iron and oxygen in the star because it had solar metallicity) is proportional to the ratio of  $(P - 1)$  for the two species, where  $P$  here is the unnormalized production factor (Section 6). When normalized to the solar mass fractions, the fraction of solar iron made in core-collapse SNe is

$$F_{\text{Fe}} = \frac{P_{\text{Fe}} - 1}{P_{\text{Ox}} - 1}. \quad (12)$$

For the series W18  $P_{\text{Fe}} = 2.17$  and  $P_{\text{Ox}} = 7.16$ ; for the N20 series  $P_{\text{Fe}} = 3.09$  and  $P_{\text{Ox}} = 8.38$ . Both sets of numbers include the low-mass contributions from the Z9.6 series. In both cases the implied iron production is 28%. Given the way this was calculated, using yields normalized to the maximum production in Table 4, this is probably an upper bound, though not by much.

While SNe Ia make most of the iron, it is noteworthy that massive stars do contribute appreciably to many species in the iron group.  $^{50}\text{V}$  is well produced by carbon burning and  $^{58}\text{Fe}$  by the *s*-process. Cobalt, copper, and the nickel isotopes are well produced and in the case of  $^{62}\text{Ni}$  actually overproduced. All three elements are made mostly by the  $\alpha$ -rich freeze-out (as

$^{58}\text{Ni}$ ,  $^{59}\text{Cu}$ , and  $^{60,61,62}\text{Zn}$ ) and are thus most sensitive to the treatment of the inner boundary in KEPLER and the explosion itself of P-HOTB. The abundances of  $^{58}\text{Ni}$  and  $^{62}\text{Zn}$ , which makes  $^{62}\text{Ni}$ , are sensitive to the neutron excess in the innermost zones. In KEPLER, appreciable electron capture occurs as these zones fall to very high density and are heated to high temperature by the shock. In P-HOTB the neutron excess in these deepest zones can be changed by the neutrinos flowing through, but this has been treated approximately. As a result, the composition of the neutrino-powered wind has not been accurately determined in either code. A higher value of  $Y_e$  in those zones would reduce the synthesis of both  $^{58}\text{Ni}$  and  $^{62}\text{Ni}$ , so their production here must be regarded as uncertain. An appreciable, though lesser, contribution to  $^{62}\text{Ni}$  also comes from the *s*-process in the helium shell.

Also noteworthy is the underproduction of  $^{55}\text{Mn}$  in massive stars. This species is made mostly as  $^{55}\text{Co}$  in a normal ( $\alpha$ -deficient) freeze-out from nuclear statistical equilibrium, and its synthesis is not so uncertain as that of nickel, which is made deeper in.

#### 6.4.4. Heavier Elements

In contrast to previous studies (e.g., Woosley & Heger 2007), the production of species above the iron group falls off rapidly. This is problematic given that the synthesis of *s*-process isotopes up to about  $A = 90$  is often attributed to massive stars (Käppeler et al. 2011). The problem is exacerbated by the fact that these are secondary elements and so are expected to be even more underproduced in stars of lower metallicity. If anything, one would like to produce an excess of isotopes in this metallicity range compared with solar values.

Figure 24 shows that production in the mass range  $A = 65\text{--}90$  is 20%–50% of what is needed. Previous studies (Woosley et al. 2002; Woosley & Heger 2007) using the same code and stellar and nuclear physics showed a slight overproduction in the same mass range. The change is a direct consequence of fewer massive stars exploding (Brown & Woosley 2013). A larger value for the  $^{22}\text{Ne}(\alpha, n)^{25}\text{Mg}$  reaction rate might help here. For calibration, the present study used reaction rates at  $3 \times 10^8 \text{ K}$  of  $2.58 \times 10^{-11} \text{ mole}^{-1} \text{ s}^{-1}$  for  $^{22}\text{Ne}(\alpha, n)^{25}\text{Mg}$  and  $8.13 \times 10^{-12} \text{ mole}^{-1} \text{ s}^{-1}$  for  $^{22}\text{Ne}(\alpha, \gamma)^{26}\text{Mg}$ , the same as used for the past 15 yr. Longland et al. (2012) recently suggested a best value of  $3.36 \times 10^{-11} \text{ mole}^{-1} \text{ s}^{-1}$  (range  $(2.74\text{--}4.15) \times 10^{-11}$ ) for  $^{22}\text{Ne}(\alpha, n)^{25}\text{Mg}$  and  $1.13 \times 10^{-11} \text{ mole}^{-1} \text{ s}^{-1}$  (range  $(0.932\text{--}1.38) \times 10^{-11}$ ) for  $^{22}\text{Ne}(\alpha, \gamma)^{26}\text{Mg}$ . Use of more modern rates would thus improve the agreement slightly, but would probably not eliminate the discrepancy. An improved treatment of overshoot mixing might also make a difference (Costa et al. 2006). Future studies to further study this discrepancy are planned. For the time being, we take the deficient production of the light *s*-process as the strongest indicator yet that something may be awry in our present 1D modeling. The possibility that a substantial fraction of heavy-element production occurs in stars that blow up because of rotation or other multidimensional effects must be considered.

Accompanying the underproduction of light *s*-process elements is a notable underproduction of the heavy *p*-process, again compared with past results. Some have suggested that the light *p*-process could also be made in the neutrino-powered

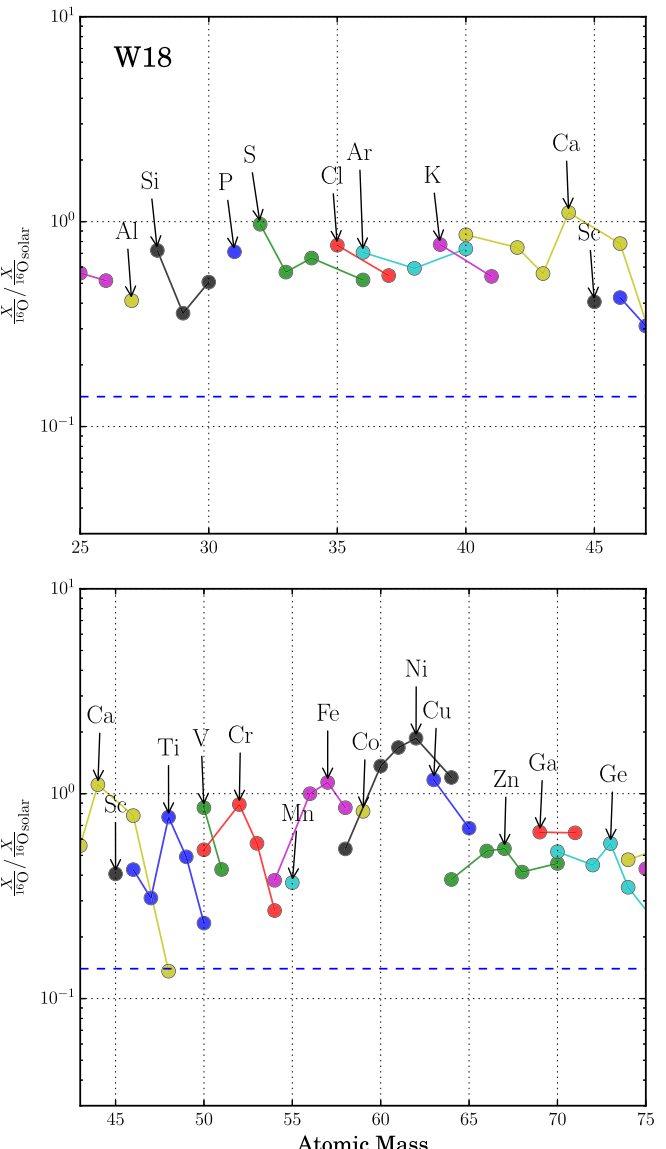


**Figure 28.** Similar to Figure 25, this figure includes contributions from all  $9\text{--}120 M_\odot$  SNe and their winds, but also an additional component from SNe Ia. Added to the average yield in Figure 25 is that of a typical sub-Chandrasekhar mass SN Ia (Woosley & Kasen 2011) with a sufficient quantity of iron to make its solar abundance relative to oxygen. This variety of SN Ia not only makes iron but also raises the production of  $^{44}\text{Ca}$  to its full solar value and increases the abundances of Si, S, Ar, and Ca so that they are closer to solar. Note, however, the underproduction of Mn/Fe. The dashed line for net production here is at 0.14.

wind (Hoffman et al. 1996; Fröhlich et al. 2006; Wanajo et al. 2011a, 2011b).

#### 6.4.5. $^{26}\text{Al}$ and $^{60}\text{Fe}$

The synthesis processes and sites of the long-lived radioactivities  $^{26}\text{Al}$  and  $^{60}\text{Fe}$  and their importance to gamma-line astronomy have been extensively discussed in the literature (Timmes et al. 1995; Limongi & Chieffi 2006a, 2006b). Here, using the W18 calibration, the IMF-averaged ejection masses for  $^{26}\text{Al}$  and  $^{60}\text{Fe}$  are, respectively,  $2.80 \times 10^{-5}$  and  $2.70 \times 10^{-5}$  solar masses per typical massive star. Using the N20 calibration instead gives  $3.63 \times 10^{-5}$  and  $3.20 \times 10^{-5}$

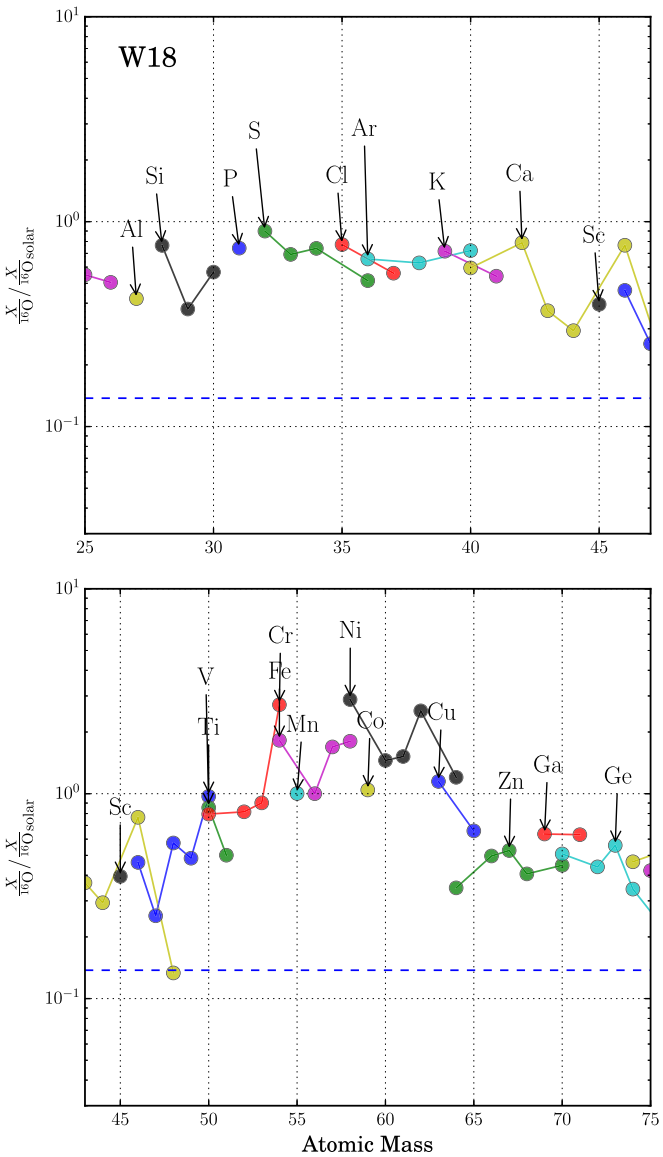


**Figure 29.** Similar to Figure 28, but including the yields of a Chandrasekhar mass model for SNe Ia (Nomoto’s W7) rather than the sub-Chandrasekhar mass model. The dashed line for net production here is at 0.14. Manganese is much improved, but  $^{44}\text{Ca}$  is lost.

solar masses per star. Gamma-ray line observations (Wang et al. 2007) imply a number ratio of  $^{60}\text{Fe}$  to  $^{26}\text{Al}$  in the interstellar medium of 0.148, which implies a mass ratio of 0.34. The ratios of 0.97 and 0.88 from our two calibrations thus exceed observations almost by a factor of three. Still, this is an improvement from Woosley & Heger (2007), where the ratio, using the same nuclear physics as here, was 1.8. This factor-of-two decrease reflects both the trapping of substantial  $^{60}\text{Fe}$  in stars that no longer explode and weaker typical explosion energies. Limongi & Chieffi (2006a) have discussed other uncertainties that might bring the models and observations into better agreement, including a modified IMF, mass loss, modified cross sections, and overshoot mixing.

As in Woosley & Heger (2007), we also note that alternate, equally justifiable choices for key nuclear reaction rates, especially for  $^{26}\text{Al}(n, p)^{26}\text{Mg}$ ,  $^{26}\text{Al}(n, \alpha)^{23}\text{Na}$ , and  $^{59,60}\text{Fe}(n, \gamma)^{60,61}\text{Fe}$ , might bring this ratio in our models down by an

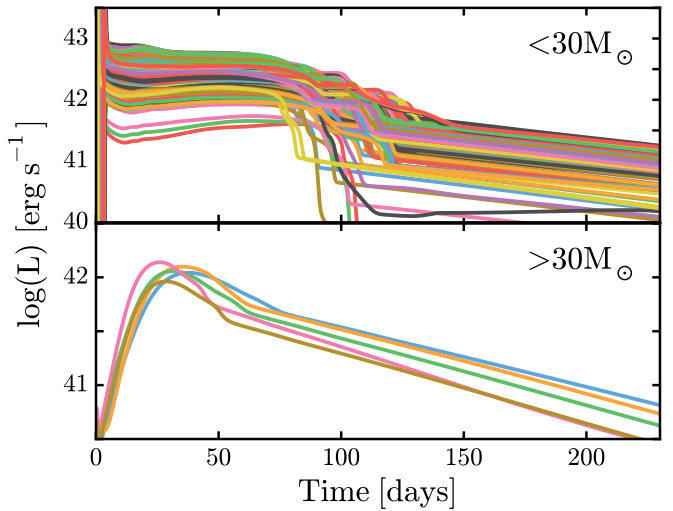


**Figure 30.** For each successful explosion calculation, the bolometric light curve was followed for 230 days. Lighter models (top) that retained a good fraction of their envelopes were SNe IIp, while heavier models (bottom) that lost most or all of their envelopes were SNe Ib or Ic. Both panels show all models that were successfully exploded by Z9.6, W18, and N20 calibrators.

additional factor of two, hence within observational errors. This possibility will be explored in a future work. Interestingly, the production ratio for  $^{60}\text{Fe}$  to  $^{26}\text{Al}$  is sensitive to stellar mass. Averaging over just the explosions from  $9$  to  $12 M_{\odot}$ , the ratio of masses ejected is close to 2.6 for both the W18 and N20 calibrations, while for heavier stars it is 0.65 (Table 6).

We have also examined the potential effect of ejecting the  $^{26}\text{Al}$  that resides in the envelopes of the stars that implode to become BHs. While not lost to winds, even weak explosions may eject these loosely bound envelopes while allowing the helium core to collapse to a singularity (Nadezhin 1980; Lovegrove & Woosley 2013). For these, we summed the total mass of  $^{26}\text{Al}$  still in the hydrogen envelopes of the stars that collapsed and added these to the yields of the stars prior to the integration. We find only a very minor improvement to the total integrated yield of aluminum, of about 7%. This helps to reduce the underproduction of  $^{26}\text{Al}$ , but not appreciably.

Additional information on  $^{60}\text{Fe}$  production is available from the  $^{60}\text{Fe}/^{56}\text{Fe}$  ratio observed in cosmic rays (Israel et al. 2015). There the ratio is thought to reflect chiefly the synthesis of both species in massive stars, diluted with some fraction of unprocessed material prior to acceleration. Observations of cosmic rays near the earth give a mass ratio that, when propagated back to the source, is  $^{60}\text{Fe}/^{56}\text{Fe} = (0.80 \pm 0.30) \times 10^{-4}$  by mass. Our IMF average of the mass ratio for  $^{60}\text{Fe}/^{56}\text{Fe}$  ejected in both sets of explosions and winds is near  $7 \times 10^{-4}$ . Assuming a standard dilution factor of 4 to one for normal ISM to massive star ejecta (Higdon & Lingenfelter 2003; Israel et al. 2015) gives an expected ratio in the local cosmic rays of  $1.4 \times 10^{-4}$ , in reasonable agreement with the observations. Again, though, a reduction of a factor of about 2 in  $^{60}\text{Fe}$  would be desirable. This ratio too is sensitive to the mass range of SNe that are sampled (Table 6) and is larger in lower-mass stars and somewhat smaller in heavier ones. Note that the iron in Table 6 is expressed in solar masses per massive star death, while that in Table 4 is per SN.

**Table 7**  
Yields in  $M_{\odot}$  from the  $14.9 M_{\odot}$  and  $25.2 M_{\odot}$  Models Using the W18 Engine

Isotope	Ejecta	Winds	Ejecta	Winds
$^1\text{H}$	5.65E+00	1.42E+00	3.42E+00	6.69E+00
$^2\text{H}$	8.25E-09	8.40E-08	7.80E-09	1.97E-07
$^3\text{He}$	3.13E-04	1.11E-04	8.94E-05	4.92E-04
$^4\text{He}$	4.03E+00	5.61E-01	4.43E+00	3.29E+00
$^6\text{Li}$	1.56E-11	5.81E-11	1.33E-11	9.74E-11
$^7\text{Li}$	3.24E-07	1.68E-09	2.54E-07	2.74E-09
$^9\text{Be}$	4.53E-11	6.14E-11	2.19E-11	9.59E-11
$^{10}\text{B}$	2.19E-09	6.02E-10	1.63E-09	1.80E-09
$^{11}\text{B}$	8.36E-07	2.38E-09	1.61E-06	5.87E-09
$^{12}\text{C}$	1.53E-01	4.12E-03	3.71E-01	1.91E-02
$^{13}\text{C}$	8.09E-04	1.93E-04	4.98E-04	7.46E-04
$^{14}\text{N}$	3.22E-02	2.66E-03	4.04E-02	2.23E-02
$^{15}\text{N}$	1.53E-04	3.94E-06	1.02E-04	1.83E-05
$^{16}\text{O}$	7.78E-01	1.30E-02	3.53E+00	5.78E-02
$^{17}\text{O}$	7.30E-05	6.61E-06	6.28E-05	2.93E-05
$^{18}\text{O}$	1.83E-03	2.72E-05	6.96E-04	1.20E-04
$^{19}\text{F}$	2.28E-05	9.15E-07	2.38E-05	3.94E-06
$^{20}\text{Ne}$	1.14E-01	2.35E-03	3.21E-01	1.18E-02
$^{21}\text{Ne}$	5.80E-04	6.34E-06	9.90E-04	4.31E-05
$^{22}\text{Ne}$	8.42E-03	1.84E-04	2.53E-02	8.07E-04
$^{23}\text{Na}$	1.82E-03	8.37E-05	1.14E-02	5.60E-04
$^{24}\text{Mg}$	4.38E-02	1.13E-03	6.83E-02	5.72E-03
$^{25}\text{Mg}$	6.85E-03	1.48E-04	1.60E-02	6.68E-04
$^{26}\text{Mg}$	6.02E-03	1.74E-04	1.53E-02	9.50E-04
$^{27}\text{Al}$	4.31E-03	1.33E-04	1.15E-02	6.78E-04
$^{28}\text{Si}$	5.71E-02	1.52E-03	4.19E-01	7.64E-03
$^{29}\text{Si}$	2.46E-03	7.97E-05	7.03E-03	4.02E-04
$^{30}\text{Si}$	2.99E-03	5.44E-05	7.53E-03	2.74E-04
$^{31}\text{P}$	7.25E-04	1.52E-05	6.72E-03	7.69E-05
$^{32}\text{S}$	3.09E-02	7.95E-04	2.51E-01	4.01E-03
$^{33}\text{S}$	1.39E-04	6.46E-06	2.55E-03	3.26E-05
$^{34}\text{S}$	1.27E-03	3.73E-05	2.23E-02	1.88E-04
$^{36}\text{S}$	4.05E-06	1.61E-07	2.25E-05	8.10E-07
$^{35}\text{Cl}$	1.17E-04	8.15E-06	6.91E-03	4.11E-05
$^{37}\text{Cl}$	5.56E-05	2.75E-06	5.22E-04	1.39E-05
$^{36}\text{Ar}$	4.79E-03	1.83E-04	3.53E-02	9.24E-04
$^{38}\text{Ar}$	5.56E-04	3.51E-05	1.59E-02	1.77E-04
$^{40}\text{Ar}$	2.40E-06	5.64E-08	8.22E-06	2.85E-07
$^{39}\text{K}$	8.84E-05	7.89E-06	4.45E-03	3.98E-05
$^{40}\text{K}$	7.78E-07	1.25E-08	4.67E-05	6.35E-08
$^{41}\text{K}$	7.28E-06	5.98E-07	1.31E-04	3.02E-06
$^{40}\text{Ca}$	3.78E-03	1.43E-04	1.27E-02	7.22E-04
$^{42}\text{Ca}$	1.52E-05	1.00E-06	6.38E-04	5.06E-06
$^{43}\text{Ca}$	3.27E-06	2.15E-07	3.10E-05	1.08E-06
$^{44}\text{Ca}$	5.69E-05	3.39E-06	1.00E-04	1.71E-05
$^{46}\text{Ca}$	3.87E-07	6.75E-09	4.33E-07	3.40E-08
$^{48}\text{Ca}$	1.75E-06	3.33E-07	1.71E-06	1.68E-06
$^{45}\text{Sc}$	1.67E-06	9.03E-08	1.09E-05	4.56E-07
$^{46}\text{Ti}$	7.73E-06	5.40E-07	9.35E-05	2.72E-06
$^{47}\text{Ti}$	6.22E-06	4.96E-07	1.98E-05	2.50E-06
$^{48}\text{Ti}$	1.79E-04	5.04E-06	2.87E-04	2.54E-05
$^{49}\text{Ti}$	9.97E-06	3.77E-07	2.09E-05	1.90E-06
$^{50}\text{Ti}$	4.23E-06	3.69E-07	1.12E-05	1.86E-06
$^{50}\text{V}$	8.82E-08	2.11E-09	1.01E-06	1.06E-08
$^{51}\text{V}$	1.79E-05	8.61E-07	3.45E-05	4.34E-06
$^{50}\text{Cr}$	4.95E-05	1.64E-06	1.13E-04	8.27E-06
$^{52}\text{Cr}$	9.99E-04	3.29E-05	1.46E-03	1.66E-04
$^{53}\text{Cr}$	1.00E-04	3.79E-06	1.55E-04	1.91E-05
$^{54}\text{Cr}$	1.36E-05	9.63E-07	3.22E-05	4.86E-06
$^{55}\text{Mn}$	4.98E-04	2.95E-05	7.05E-04	1.49E-04
$^{54}\text{Fe}$	3.21E-03	1.55E-04	5.21E-03	7.83E-04
$^{56}\text{Fe}$	8.34E-02	2.53E-03	1.23E-01	1.28E-02
$^{57}\text{Fe}$	3.12E-03	5.94E-05	4.65E-03	3.00E-04
$^{58}\text{Fe}$	4.54E-04	8.03E-06	1.32E-03	4.05E-05
$^{59}\text{Co}$	4.04E-04	8.05E-06	9.19E-04	4.06E-05

**Table 7**  
(Continued)

Isotope	Ejecta	Winds	Ejecta	Winds
$^{58}\text{Ni}$	2.51E-03	1.11E-04	3.81E-03	5.59E-04
$^{60}\text{Ni}$	2.70E-03	4.42E-05	5.29E-03	2.23E-04
$^{61}\text{Ni}$	1.79E-04	1.95E-06	5.05E-04	9.84E-06
$^{62}\text{Ni}$	6.44E-04	6.32E-06	1.66E-03	3.19E-05
$^{64}\text{Ni}$	8.78E-05	1.66E-06	3.99E-04	8.37E-06
$^{63}\text{Cu}$	9.24E-05	1.35E-06	3.12E-04	6.81E-06
$^{65}\text{Cu}$	2.35E-05	6.20E-07	1.31E-04	3.13E-06
$^{64}\text{Zn}$	7.53E-05	2.25E-06	1.38E-04	1.13E-05
$^{66}\text{Zn}$	3.34E-05	1.33E-06	2.31E-04	6.68E-06
$^{67}\text{Zn}$	5.55E-06	1.98E-07	2.61E-05	9.98E-07
$^{68}\text{Zn}$	1.74E-05	9.17E-07	1.21E-04	4.63E-06
$^{70}\text{Zn}$	1.44E-06	3.13E-08	6.45E-07	1.58E-07
$^{69}\text{Ga}$	2.52E-06	8.75E-08	2.17E-05	4.41E-07
$^{71}\text{Ga}$	1.70E-06	5.98E-08	1.25E-05	3.02E-07
$^{70}\text{Ge}$	1.64E-06	1.05E-07	3.18E-05	5.31E-07
$^{72}\text{Ge}$	2.22E-06	1.41E-07	2.93E-05	7.12E-07
$^{73}\text{Ge}$	9.87E-07	3.99E-08	5.44E-06	2.01E-07
$^{74}\text{Ge}$	2.83E-06	1.88E-07	1.60E-05	9.49E-07
$^{76}\text{Ge}$	6.65E-07	4.01E-08	3.43E-07	2.02E-07
$^{75}\text{As}$	7.39E-07	2.69E-08	3.82E-06	1.36E-07
$^{74}\text{Se}$	4.96E-08	2.53E-09	1.21E-06	1.28E-08
$^{76}\text{Se}$	4.21E-07	2.75E-08	1.03E-05	1.39E-07
$^{77}\text{Se}$	4.69E-07	2.27E-08	2.99E-06	1.14E-07
$^{78}\text{Se}$	7.18E-07	7.17E-08	9.32E-06	3.62E-07
$^{80}\text{Se}$	1.53E-06	1.53E-07	8.07E-06	7.74E-07
$^{82}\text{Se}$	3.94E-07	2.77E-08	1.64E-07	1.40E-07
$^{79}\text{Br}$	3.94E-07	2.67E-08	2.65E-06	1.35E-07
$^{81}\text{Br}$	3.56E-07	2.65E-08	2.22E-06	1.34E-07
$^{78}\text{Kr}$	6.25E-09	9.15E-10	1.05E-07	4.62E-09
$^{80}\text{Kr}$	6.16E-08	6.00E-09	1.66E-06	3.03E-08
$^{82}\text{Kr}$	2.76E-07	3.09E-08	5.69E-06	1.56E-07
$^{83}\text{Kr}$	3.33E-07	3.11E-08	1.64E-06	1.57E-07
$^{84}\text{Kr}$	1.11E-06	1.55E-07	5.85E-06	7.81E-07
$^{86}\text{Kr}$	7.23E-07	4.80E-08	1.38E-06	2.42E-07
$^{85}\text{Rb}$	3.57E-07	2.37E-08	1.52E-06	1.20E-07
$^{87}\text{Rb}$	1.27E-07	9.96E-09	1.00E-06	5.02E-08
$^{84}\text{Sr}$	3.95E-09	6.46E-10	1.60E-07	3.26E-09
$^{86}\text{Sr}$	8.84E-08	1.17E-08	2.12E-06	5.91E-08
$^{87}\text{Sr}$	5.67E-08	8.29E-09	8.19E-07	4.18E-08
$^{88}\text{Sr}$	8.10E-07	1.00E-07	4.34E-06	5.06E-07
$^{89}\text{Y}$	1.80E-07	2.41E-08	1.02E-06	1.21E-07
$^{90}\text{Zr}$	1.95E-07	3.07E-08	2.03E-06	1.55E-07
$^{91}\text{Zr}$	4.83E-08	6.81E-09	1.33E-07	3.43E-08
$^{92}\text{Zr}$	7.05E-08	1.05E-08	1.42E-07	5.30E-08
$^{94}\text{Zr}$	6.99E-08	1.09E-08	1.04E-07	5.48E-08
$^{96}\text{Zr}$	1.64E-08	1.79E-09	1.48E-08	9.01E-09
$^{93}\text{Nb}$	2.74E-08	4.11E-09	4.34E-08	2.08E-08
$^{92}\text{Mo}$	1.06E-08	2.09E-09	1.82E-08	1.05E-08
$^{94}\text{Mo}$	6.94E-09	1.33E-09	1.10E-08	6.70E-09
$^{95}\text{Mo}$	1.51E-08	2.31E-09	1.81E-08	1.16E-08
$^{96}\text{Mo}$	1.30E-08	2.45E-09	2.25E-08	1.23E-08
$^{97}\text{Mo}$	8.35E-09	1.42E-09	9.51E-09	7.15E-09
$^{98}\text{Mo}$	1.98E-08	3.61E-09	2.59E-08	1.82E-08
$^{100}\text{Mo}$	7.82E-09	1.47E-09	6.79E-09	7.43E-09
$^{96}\text{Ru}$	3.04E-09	5.94E-10	3.68E-09	3.00E-09
$^{98}\text{Ru}$	1.17E-09	2.05E-10	4.63E-09	1.03E-09
$^{99}\text{Ru}$	7.09E-09	1.41E-09	7.88E-09	7.10E-09
$^{100}\text{Ru}$	7.60E-09	1.40E-09	1.31E-08	7.08E-09
$^{101}\text{Ru}$	9.32E-09	1.92E-09	8.46E-09	9.69E-09
$^{102}\text{Ru}$	1.90E-08	3.59E-09	2.04E-08	1.81E-08
$^{104}\text{Ru}$	1.17E-08	2.17E-09	1.04E-08	1.09E-08
$^{103}\text{Rh}$	1.10E-08	2.25E-09	1.12E-08	1.13E-08
$^{102}\text{Pd}$	8.01E-10	8.75E-11	5.29E-09	4.41E-10
$^{104}\text{Pd}$	5.43E-09	9.78E-10	1.05E-08	4.93E-09

**Table 7**  
(Continued)

Isotope	Ejecta	Winds	Ejecta	Winds
<sup>105</sup> Pd	9.59E-09	1.97E-09	8.67E-09	9.95E-09
<sup>106</sup> Pd	1.32E-08	2.45E-09	1.54E-08	1.23E-08
<sup>108</sup> Pd	1.30E-08	2.41E-09	1.46E-08	1.21E-08
<sup>110</sup> Pd	6.15E-09	1.08E-09	5.15E-09	5.47E-09
<sup>107</sup> Ag	7.80E-09	1.60E-09	7.49E-09	8.07E-09
<sup>109</sup> Ag	7.44E-09	1.51E-09	7.59E-09	7.63E-09
<sup>106</sup> Cd	1.28E-09	1.23E-10	4.65E-09	6.22E-10
<sup>108</sup> Cd	9.70E-10	8.93E-11	8.48E-09	4.51E-10
<sup>110</sup> Cd	7.27E-09	1.28E-09	1.32E-08	6.45E-09
<sup>111</sup> Cd	6.51E-09	1.32E-09	6.31E-09	6.67E-09
<sup>112</sup> Cd	1.33E-08	2.51E-09	1.47E-08	1.27E-08
<sup>113</sup> Cd	6.41E-09	1.29E-09	6.03E-09	6.49E-09
<sup>114</sup> Cd	1.72E-08	3.05E-09	2.00E-08	1.54E-08
<sup>116</sup> Cd	5.93E-09	8.11E-10	5.99E-09	4.09E-09
<sup>113</sup> In	3.02E-10	5.18E-11	2.42E-09	2.61E-10
<sup>115</sup> In	5.94E-09	1.17E-09	6.06E-09	5.89E-09
<sup>112</sup> Sn	2.42E-09	2.39E-10	1.78E-08	1.21E-09
<sup>114</sup> Sn	1.47E-09	1.65E-10	3.01E-08	8.30E-10
<sup>115</sup> Sn	4.30E-10	8.53E-11	2.87E-09	4.30E-10
<sup>116</sup> Sn	1.94E-08	3.69E-09	3.13E-08	1.86E-08
<sup>117</sup> Sn	9.96E-09	1.97E-09	1.04E-08	9.92E-09
<sup>118</sup> Sn	3.42E-08	6.26E-09	4.23E-08	3.16E-08
<sup>119</sup> Sn	1.18E-08	2.25E-09	1.25E-08	1.13E-08
<sup>120</sup> Sn	5.02E-08	8.57E-09	6.10E-08	4.32E-08
<sup>122</sup> Sn	1.10E-08	1.24E-09	9.69E-09	6.25E-09
<sup>124</sup> Sn	8.90E-09	1.57E-09	6.68E-09	7.94E-09
<sup>121</sup> Sb	7.34E-09	1.34E-09	7.83E-09	6.74E-09
<sup>123</sup> Sb	5.43E-09	1.02E-09	4.75E-09	5.13E-09
<sup>120</sup> Te	3.24E-10	3.23E-11	1.62E-09	1.63E-10
<sup>122</sup> Te	4.93E-09	8.97E-10	7.30E-09	4.53E-09
<sup>123</sup> Te	1.69E-09	3.15E-10	2.15E-09	1.59E-09
<sup>124</sup> Te	9.12E-09	1.69E-09	1.27E-08	8.52E-09
<sup>125</sup> Te	1.27E-08	2.53E-09	1.26E-08	1.28E-08
<sup>126</sup> Te	3.53E-08	6.75E-09	3.78E-08	3.40E-08
<sup>128</sup> Te	5.80E-08	1.15E-08	4.82E-08	5.78E-08
<sup>130</sup> Te	6.30E-08	1.24E-08	5.08E-08	6.27E-08
<sup>127</sup> I	3.51E-08	7.43E-09	2.98E-08	3.75E-08
<sup>124</sup> Xe	7.74E-10	5.06E-11	6.79E-09	2.55E-10
<sup>126</sup> Xe	6.53E-10	4.46E-11	1.11E-08	2.25E-10
<sup>128</sup> Xe	6.68E-09	9.01E-10	1.52E-08	4.55E-09
<sup>129</sup> Xe	5.35E-08	1.12E-08	4.44E-08	5.65E-08
<sup>130</sup> Xe	1.20E-08	1.80E-09	1.85E-08	9.09E-09
<sup>131</sup> Xe	4.41E-08	9.03E-09	4.06E-08	4.56E-08
<sup>132</sup> Xe	5.93E-08	1.10E-08	6.25E-08	5.56E-08
<sup>134</sup> Xe	2.54E-08	4.09E-09	2.08E-08	2.07E-08
<sup>136</sup> Xe	1.91E-08	3.39E-09	1.76E-08	1.71E-08
<sup>133</sup> Cs	1.52E-08	2.87E-09	1.68E-08	1.45E-08
<sup>130</sup> Ba	1.07E-09	3.51E-11	1.28E-08	1.77E-10
<sup>132</sup> Ba	7.81E-10	3.41E-11	1.30E-08	1.72E-10
<sup>134</sup> Ba	5.59E-09	8.27E-10	1.37E-08	4.17E-09
<sup>135</sup> Ba	1.28E-08	2.27E-09	1.42E-08	1.14E-08
<sup>136</sup> Ba	1.68E-08	2.73E-09	3.08E-08	1.38E-08
<sup>137</sup> Ba	2.53E-08	3.93E-09	3.43E-08	1.98E-08
<sup>138</sup> Ba	1.65E-07	2.53E-08	2.63E-07	1.28E-07
<sup>138</sup> La	1.40E-10	3.25E-12	3.16E-10	1.64E-11
<sup>139</sup> La	2.21E-08	3.59E-09	3.23E-08	1.81E-08
<sup>136</sup> Ce	1.81E-10	1.73E-11	2.50E-09	8.74E-11
<sup>138</sup> Ce	2.27E-10	2.37E-11	2.11E-09	1.20E-10
<sup>140</sup> Ce	4.91E-08	8.49E-09	6.99E-08	4.28E-08
<sup>142</sup> Ce	5.89E-09	1.08E-09	5.74E-09	5.46E-09
<sup>141</sup> Pr	7.68E-09	1.44E-09	1.11E-08	7.25E-09
<sup>142</sup> Nd	1.06E-08	1.89E-09	2.16E-08	9.54E-09
<sup>143</sup> Nd	4.39E-09	8.45E-10	4.73E-09	4.26E-09
<sup>144</sup> Nd	9.14E-09	1.68E-09	9.91E-09	8.48E-09

**Table 7**  
(Continued)

Isotope	Ejecta	Winds	Ejecta	Winds
<sup>145</sup> Nd	2.96E-09	5.90E-10	3.32E-09	2.98E-09
<sup>146</sup> Nd	6.90E-09	1.23E-09	7.54E-09	6.20E-09
<sup>148</sup> Nd	2.21E-09	4.18E-10	2.08E-09	2.11E-09
<sup>150</sup> Nd	2.09E-09	4.14E-10	1.62E-09	2.09E-09
<sup>144</sup> Sm	8.52E-10	6.60E-11	1.81E-08	3.33E-10
<sup>147</sup> Sm	1.76E-09	3.39E-10	1.58E-09	1.71E-09
<sup>148</sup> Sm	1.34E-09	2.49E-10	1.54E-09	1.26E-09
<sup>149</sup> Sm	1.49E-09	3.07E-10	1.25E-09	1.55E-09
<sup>150</sup> Sm	9.40E-10	1.66E-10	1.17E-09	8.36E-10
<sup>152</sup> Sm	3.16E-09	6.06E-10	2.71E-09	3.06E-09
<sup>154</sup> Sm	2.70E-09	5.22E-10	2.27E-09	2.63E-09
<sup>151</sup> Eu	1.95E-09	4.04E-10	1.56E-09	2.03E-09
<sup>153</sup> Eu	2.11E-09	4.46E-10	1.76E-09	2.25E-09
<sup>152</sup> Gd	7.06E-11	5.98E-12	6.21E-11	3.05E-11
<sup>154</sup> Gd	4.20E-10	6.54E-11	4.24E-10	3.31E-10
<sup>155</sup> Gd	2.17E-09	4.48E-10	1.89E-09	2.26E-09
<sup>156</sup> Gd	3.20E-09	6.22E-10	2.83E-09	3.14E-09
<sup>157</sup> Gd	2.34E-09	4.80E-10	2.09E-09	2.42E-09
<sup>158</sup> Gd	4.05E-09	7.65E-10	3.90E-09	3.86E-09
<sup>160</sup> Gd	3.35E-09	6.82E-10	2.80E-09	3.44E-09
<sup>159</sup> Tb	2.64E-09	5.52E-10	2.33E-09	2.78E-09
<sup>156</sup> Dy	1.32E-11	1.98E-12	8.72E-11	9.97E-12
<sup>158</sup> Dy	2.41E-11	3.43E-12	9.67E-11	1.73E-11
<sup>160</sup> Dy	5.52E-10	8.49E-11	8.83E-10	4.29E-10
<sup>161</sup> Dy	3.28E-09	6.91E-10	2.80E-09	3.48E-09
<sup>162</sup> Dy	4.79E-09	9.37E-10	4.23E-09	4.73E-09
<sup>163</sup> Dy	4.39E-09	9.21E-10	3.75E-09	4.65E-09
<sup>164</sup> Dy	5.58E-09	1.05E-09	5.44E-09	5.29E-09
<sup>165</sup> Ho	4.16E-09	8.71E-10	3.51E-09	4.39E-09
<sup>162</sup> Er	3.88E-11	3.33E-12	1.95E-10	1.68E-11
<sup>164</sup> Er	2.27E-10	3.95E-11	2.83E-10	1.99E-10
<sup>166</sup> Er	4.30E-09	8.37E-10	3.89E-09	4.22E-09
<sup>167</sup> Er	2.81E-09	5.74E-10	2.49E-09	2.90E-09
<sup>168</sup> Er	3.77E-09	6.74E-10	3.51E-09	3.40E-09
<sup>170</sup> Er	2.00E-09	3.81E-10	1.78E-09	1.92E-09
<sup>169</sup> Tm	1.88E-09	3.67E-10	1.79E-09	1.85E-09
<sup>168</sup> Yb	4.62E-11	3.19E-12	2.17E-10	1.61E-11
<sup>170</sup> Yb	5.70E-10	7.53E-11	7.91E-10	3.80E-10
<sup>171</sup> Yb	1.85E-09	3.55E-10	1.78E-09	1.79E-09
<sup>172</sup> Yb	3.09E-09	5.48E-10	3.13E-09	2.76E-09
<sup>173</sup> Yb	2.06E-09	4.07E-10	1.96E-09	2.06E-09
<sup>174</sup> Hf	6.61E-11	2.81E-12	1.44E-10	1.42E-11
<sup>176</sup> Hf	8.19E-10	9.13E-11	9.09E-10	4.61E-10
<sup>177</sup> Hf	1.68E-09	3.29E-10	1.47E-09	1.66E-09
<sup>178</sup> Hf	2.95E-09	4.84E-10	2.71E-09	2.44E-09
<sup>179</sup> Hf	1.27E-09	2.43E-10	1.22E-09	1.23E-09
<sup>180</sup> Hf	3.52E-09	6.30E-10	3.64E-09	3.18E-09
<sup>180</sup> Ta	3.53E-12	2.65E-14	4.71E-12	1.34E-13
<sup>181</sup> Ta	1.20E-09	2.23E-10	1.39E-09	1.12E-09
<sup>180</sup> W	6.68E-11	1.62E-12	1.07E-10	8.15E-12
<sup>182</sup> W	2.27E-09	3.61E-10	2.49E-09	1.82E-09
<sup>183</sup> W	1.11E-09	1.96E-10	1.20E-09	9.90E-10
<sup>184</sup> W	2.47E-09	4.23E-10	2.41E-09	2.14E-09
<sup>186</sup> W	2.09E-09	3.95E-10	2.11E-09	1.99E-09
<sup>185</sup> Re	1.09E-09	2.13E-10	1.05E-09	1.07E-09
<sup>187</sup> Re	1.87E-09	3.89E-10	1.60E-09	1.96E-09
<sup>184</sup> Os	4.24E-11	1.44E-12	1.03E-10	7.25E-12
<sup>186</sup> Os	6.89E-10	1.17E-10	7.45E-10	5.90E-10
<sup>187</sup> Os	4.72E-10	9.38E-11	4.34E-10	4.73E-10
<sup>188</sup> Os	5.07E-09	9.88E-10	4.57E-09	4.98E-09

**Table 7**  
(Continued)

Isotope	Ejecta	Winds	Ejecta	Winds
$^{189}\text{Os}$	5.66E-09	1.21E-09	4.47E-09	6.10E-09
$^{190}\text{Os}$	9.99E-09	1.98E-09	8.41E-09	9.98E-09
$^{192}\text{Os}$	1.49E-08	3.11E-09	1.17E-08	1.57E-08
$^{191}\text{Ir}$	1.25E-08	2.69E-09	9.72E-09	1.36E-08
$^{193}\text{Ir}$	2.15E-08	4.58E-09	1.70E-08	2.31E-08
$^{190}\text{Pt}$	2.12E-11	2.07E-12	4.20E-11	1.04E-11
$^{192}\text{Pt}$	1.10E-09	1.20E-10	1.25E-09	6.05E-10
$^{194}\text{Pt}$	2.56E-08	5.10E-09	2.16E-08	2.57E-08
$^{195}\text{Pt}$	2.50E-08	5.26E-09	2.08E-08	2.65E-08
$^{196}\text{Pt}$	2.09E-08	3.93E-09	1.90E-08	1.98E-08
$^{198}\text{Pt}$	5.99E-09	1.13E-09	4.79E-09	5.70E-09
$^{197}\text{Au}$	1.18E-08	2.27E-09	1.47E-08	1.14E-08
$^{196}\text{Hg}$	2.71E-09	7.25E-12	1.78E-08	3.65E-11
$^{198}\text{Hg}$	3.53E-09	4.78E-10	1.13E-08	2.41E-09
$^{199}\text{Hg}$	4.64E-09	8.15E-10	5.38E-09	4.11E-09
$^{200}\text{Hg}$	7.62E-09	1.12E-09	1.01E-08	5.64E-09
$^{201}\text{Hg}$	3.72E-09	6.42E-10	4.37E-09	3.24E-09
$^{202}\text{Hg}$	9.96E-09	1.46E-09	1.23E-08	7.37E-09
$^{204}\text{Hg}$	2.83E-09	3.39E-10	3.12E-09	1.71E-09
$^{203}\text{Tl}$	4.39E-09	6.50E-10	6.48E-09	3.28E-09
$^{205}\text{Tl}$	1.01E-08	1.56E-09	1.23E-08	7.89E-09
$^{204}\text{Pb}$	5.08E-09	7.73E-10	8.38E-09	3.90E-09
$^{206}\text{Pb}$	4.54E-08	7.27E-09	6.53E-08	3.67E-08
$^{207}\text{Pb}$	4.84E-08	8.09E-09	7.06E-08	4.08E-08
$^{208}\text{Pb}$	1.31E-07	2.33E-08	1.59E-07	1.17E-07
$^{209}\text{Bi}$	9.32E-09	1.70E-09	1.02E-08	8.59E-09
$^{232}\text{Th}$	7.19E-17	0.00E+00	0.00E+00	0.00E+00
$^{235}\text{U}$	1.04E-18	0.00E+00	0.00E+00	0.00E+00
$^{238}\text{U}$	0.00E+00	0.00E+00	0.00E+00	0.00E+00
$^{26}\text{Al}$	3.16E-05	2.66E-09	7.78E-05	2.41E-06
$^{60}\text{Fe}$	4.70E-05	0.00E+00	3.58E-05	1.09E-16

## 6.5. A Type Ia SN Contribution

### 6.5.1. Nucleosynthesis

The correct model or models for SNe Ia are currently under much debate. In terms of nucleosynthesis, however, the models segregate into two general categories: explosions near the Chandrasekhar mass by a combination of deflagration and detonation, and prompt detonations in sub-Chandrasekhar mass white dwarfs. The requirement that any successful model makes  $\sim 0.6 M_{\odot}$  of  $^{56}\text{Ni}$  in order to explain the light curve and  $\sim 0.2 M_{\odot}$  of intermediate-mass elements to explain the spectrum determines the acceptable bulk nucleosynthesis, so that the models differ only in detail. Here, as a representative example of the Chandrasekhar mass model, we use the nucleosynthesis from Nomoto's highly successful "W7" model (Iwamoto et al. 1999). For the sub-Chandrasekhar mass model we use model 10HC of Woosley & Kasen (2011). This detonation of a  $1.0 M_{\odot}$  carbon–oxygen white dwarf capped by  $0.0445 M_{\odot}$  of accreted helium produced  $0.636 M_{\odot}$  of  $^{56}\text{Ni}$  in an explosion with final kinetic energy  $1.2 \times 10^{51}$  erg. The contribution from each SN Ia model was normalized so as to produce a solar proportion of  $^{56}\text{Fe}/^{16}\text{O}$  when combined with the integrated yield of massive stars from 9 to  $120 M_{\odot}$ .

The combined nucleosynthesis is given in Figure 28 for a sub-Chandrasekhar white dwarf and in Figure 29 for the Chandrasekhar mass model. Most of the intermediate-mass elements are unchanged, though some of these isotopes do

change. Not surprisingly, the introduction of SNe Ia improves the overall fit especially for the iron group. The sub-Chandrasekhar mass model greatly improves the production of  $^{44}\text{Ca}$  (made by helium detonation as  $^{44}\text{Ti}$ ) and seems to be required if only because of that unique contribution. The Chandrasekhar mass model, on the other hand, does a much better job of producing manganese, suggesting that this component may also be needed (see also Seitenzahl et al. 2013a; Yamaguchi et al. 2015). The Chandrasekhar mass model overproduces nickel, however. This is a known deficiency of model W7 having to do with excess electron capture at high density. It might be circumvented in more modern multidimensional models (e.g., Seitenzahl et al. 2013b) especially if the white dwarf expands appreciably during the deflagration stage prior to detonating.

### 6.5.2. Implications for SN Rates

As noted previously (Section 6.4.3), our massive star models are responsible for producing about 28% of the iron in the Sun. The average SN Ia makes very nearly  $0.6 M_{\odot}$ . That being the case, and assuming that the typical successful core-collapse SN (mostly SNe IIp in the present study) makes  $0.04\text{--}0.05 M_{\odot}$  of new iron (Table 4), the implied ratio of SN Ia event rates to SN IIp is 1/6 to 1/5. If core-collapse SNe made a little less iron, as seems likely, then the SN Ia rate would need to be a bit bigger. This ratio is consistent with observations for spiral galaxies similar to the Milky Way (Li et al. 2011).

We can also use these abundances, particularly the fact that each massive star above  $9 M_{\odot}$  produces an average of  $0.57 M_{\odot}$  of  $^{16}\text{O}$ , to infer a rate of SNe II (assuming that stars below  $9 M_{\odot}$  produce little oxygen in their evolution). From the solar abundance of  $^{16}\text{O}$  of  $6.6 \times 10^{-3}$  (Lodders 2003), we find that there must have been 0.012 massive stars per solar mass of Population I material. Assuming that 66% of these stars become SNe, as we found in our models, we find that integrated over galactic time, there must be 0.0076 core-collapse SNe (visible or invisible) per solar mass of Population I material in order to explain the present solar abundance. This seems a reasonable, albeit very approximate, number, especially if the SN rate was different in the past.

## 7. LIGHT CURVES

The KEPLER code incorporates flux-limited radiative diffusion and thus is capable of calculating approximate bolometric light curves for SNe of all types. The light-curve calculation includes contributions both from the diffusion of energy deposited by the shock wave and from the decay of radioactive  $^{56}\text{Ni}$  and  $^{56}\text{Co}$ . Light curves were calculated as described in Woosley & Heger (2007) using a full Saha solver for 19 elements, hydrogen to nickel, to obtain the electron density, and adopting a lower bound to the opacity of  $10^{-5} \text{ cm}^2 \text{ g}^{-1}$ . The full model set corresponding to the successful explosions using the central engines Z9.6, W18, and N20 was post-processed to obtain the luminosity evolution until about 230 days, which was well past the plateau and peak for all models. For the mass-loss prescription used, explosions below  $40 M_{\odot}$ , i.e., most successful explosions, produced SNe IIp with a distinct plateau phase. The heavier stars gave rise to SNe Ib or Ic. Figure 30 illustrates the diversity of outcomes from the full model set. In this section, we discuss the systematics of these results and how they compare with simple analytic scalings in

**Table 8**  
SN Mass Statistics

Mass Range	Engine(s)	$\bar{M}_{\text{SN}}$	$f(\text{No Wind})$
$\leq 12$	Z9.6+W18	10.25	0.19 (0.40)
12–30	...	14.5	0.37 (0.54)
30–120	...	60.0	0.44 (0.010)
9–120	...	12.0	1
$\leq 12$	Z9.6+N20	10.25	0.18 (0.40)
12–30	...	15.2	0.39 (0.58)
30–120	...	80.0	0.43 (0.026)
9–120	...	12.25	1

the literature. Some scalings of particular interest to observers are summarized in Section 4.2. All of our light-curve data are included in the electronic edition in a tar.gz package.

Since the light-curve results from W18 and N20 engines are qualitatively similar, in the following analysis only the N20 series is considered, supplemented by Z9.6 below  $12 M_{\odot}$ .

### 7.1. Type IIp

Since all of the models that retained their hydrogen envelope were, at death, red supergiants, most of the SNe modeled here were of Type IIp. A wide diversity of durations and luminosities on the plateau is expected observationally (Arcavi et al. 2012), and was found owing to the variable pre-SN radius, explosion energy, envelope mass,  $^{56}\text{Ni}$  ejected, and mixing. Luminosities on the plateau ranged across at least a decade in luminosity ( $10^{41.5}\text{--}10^{43}$  erg s $^{-1}$ ), with the most luminous events coming from the energetic explosions of stars with exceptionally large radii, touching  $10^{14}$  cm. Tables 7 and 8 also show a variable amount of  $^{56}\text{Ni}$  ranging from 0.003 to 0.15  $M_{\odot}$ . The envelope masses ( $M_{\text{i}}\text{--}M_{\text{o}}$ ) and radii of the exploding models can be inferred from Table 2 and, for common events, are typically  $7\text{--}10 M_{\odot}$  and  $3\text{--}8 \times 10^{13}$  cm. The explosion energy varied from 0.1 to  $2 \times 10^{51}$  erg (see Figure 16), with a typical value around  $0.7 \times 10^{51}$  erg (Table 4).

Approximate analytic scaling rules have been derived for both the luminosity on the plateau and its duration by Popov (1993) and Kasen & Woosley (2009). An important issue is how to measure these quantities, both observationally and for the models. A variety of definitions are used in the literature. The luminosity is not really constant on the “plateau,” and the plateau’s onset might be counted as beginning at shock breakout, the cooling and recombination of hydrogen in the outermost zone, or the time when the effective temperature first falls below some value. Even more uncertain, the end of the plateau might be measured as when the envelope first combines, when the whole ejecta first becomes optically transparent, or the beginning of the radioactive tail, if there is one. Here it is assumed that the bolometric luminosity is evaluated 50 days after shock breakout and that shock breakout defines the beginning of the plateau. This is clearly a lower bound to the actual commencement. For most models, recombination begins about 3 days later, which is short compared with the approximate 100-day duration of the plateau. All SN IIp light-curve plateaus were substantially longer than 50 days.

Two measures are used to bracket the end of the plateau. One is when the photospheric radius recedes to less than one-half of its maximum value. Empirically, this corresponds

roughly to when the recombination front reaches the base of the hydrogen envelope (or the density increase associated with that former boundary, if the composition has been mixed). This is an operational lower bound to the duration of the plateau. Later, after the internal energy of the helium and heavy-element core has diffused out, the whole star recombines and the photosphere shrinks inside  $10^{14}$  cm. It is at this point that any radioactive contribution reaches steady state with the SN luminosity and the “tail” of the light curve begins. For the observer, these two limits thus correspond to the first strong downward inflection of the light curve and the onset of the characteristic exponential decay on the tail.

All of our models are artificially mixed after explosive nucleosynthesis has ended, in order to account empirically for both the turbulent convection that goes on behind the shock during the explosion and the Rayleigh–Taylor mixing following the reverse shock. The mixing is calibrated, crudely, to SN 1987A (Woosley 1988; Kasen & Woosley 2009). Because most of our models experienced little fallback, mixing is not very important to the nucleosynthesis calculated here.

#### 7.1.1. Analytic Scalings

The scalings of Popov (1993), to which our luminosities and plateau durations are compared, are

$$\begin{aligned} L &\propto E^{5/6} M^{-1/2} R^{2/3} \kappa^{-1/3} T_i^{4/3}, \\ t &\propto E^{-1/6} M^{1/2} R^{1/6} \kappa^{1/6} T_i^{-2/3}, \end{aligned} \quad (13)$$

where  $E$  is the explosion energy,  $M$  the envelope mass,  $R$  the progenitor radius,  $\kappa$  the opacity, and  $T_i$  the ionization temperature, which is the effective emission temperature divided by  $2^{1/4}$ . Adopting, from our models on the plateau, a typical effective temperature of 6300 K (Popov used 6000 K) and retaining his opacity of  $0.34 \text{ cm}^2 \text{ g}^{-1}$ , one has the analytic results

$$\begin{aligned} L_{50} &= C_L E_{51}^{5/6} M_{10}^{-1/2} R_{0,500}^{2/3} \text{ erg s}^{-1}, \\ t_{p,0} &= C_t E_{51}^{-1/6} M_{10}^{1/2} R_{0,500}^{1/6} \text{ days}, \end{aligned} \quad (14)$$

where  $C_L$  and  $C_t$  are  $1.82 \times 10^{42}$  erg s $^{-1}$  and 96 days, respectively.  $L_{50}$  is the bolometric luminosity 50 days after shock breakout,  $t_{p,0}$  is the plateau duration without any radioactive contribution,  $E_{51}$  is the final kinetic energy of the explosion in  $10^{51}$  erg units,  $R_{0,500}$  is the radius of the pre-SN star in units of  $500 R_{\odot}$ , and  $M_{10}$  is the mass of the pre-SN hydrogen envelope in units of  $10 M_{\odot}$ .

For the bolometric luminosity, calibrated to our entire set of 181 Type IIp models, 50 days after core collapse we find

$$L_{50} = 1.85 \times 10^{42} E_{51}^{5/6} M_{10}^{-1/2} R_{0,500}^{2/3} \text{ erg s}^{-1}. \quad (15)$$

This agrees extremely well with Popov’s predicted scaling and is our recommended value for this survey. The agreement with all the SN models is excellent, as shown in Figure 31.

Kasen & Woosley (2009) gave similar scalings to Equation (14) and calibrated them to a small set of numerical models that used similar physics to the present work:

$$\begin{aligned} L_{50} &= 1.26 \times 10^{42} E_{51}^{5/6} M_{10}^{-1/2} R_{0,500}^{2/3} X_{\text{He},0.33}^1 \text{ erg s}^{-1}, \\ t_{p,0} &= 122 E_{51}^{-1/4} M_{10}^{1/2} R_{0,500}^{1/6} X_{\text{He},0.33}^{-1/2} \text{ days}, \end{aligned} \quad (16)$$

where  $X_{\text{He}}$  is the helium mass fraction in the envelope. Two typographical errors in Equation (11) of Kasen & Woosley (2009) are fixed here: (1)  $X_{\text{He}}$  is normalized to 0.33, and (2)  $t_{\text{p},0} \propto X_{\text{He},0.33}^{-1/2}$ . In comparison to Equations (13) and (14), this formula assumes scaling with  $X_{\text{He}}$ , which ranged from 0.30 to 0.53 in the models. Given that the helium mass fraction is typically greater than 0.33, Kasen & Woosley's formula for the luminosity is similar to Popov's, though slightly fainter. Their formula for the plateau duration has been empirically adjusted to models (hence  $E^{-1/4}$  instead of  $E^{-1/6}$ ) and is a bit longer, possibly owing to differing definitions of what constitutes the plateau.

### 7.1.2. Plateau Duration and Recombination Timescale

As alluded to earlier, the duration of the plateau is more ambiguously defined than the luminosity on a particular day. It is also more sensitive to corrections for mixing and radioactivity. The original scalings of Popov (1993) accounted for neither. To compare with Equation (14) and determine our own estimate of  $t_{\text{p},0}$ , the plateau duration without radioactivity, the light curves of 26 models from the Z9.6 and N20 series with masses from 9 to  $27 M_{\odot}$  were recalculated by assuming that no  $^{56}\text{Ni}$  was produced in the explosion. Two possible durations of the plateau were estimated for each corresponding to the time between shock breakout and when the photospheric radius shrinks to (a) 50% of its maximum and (b)  $10^{14}$  cm. The top panel of Figure 32 compares this range from the models with Popov's expression—Equation (14).

The range between upper and lower bounds (shaded gray) is mostly due to the energy that continues to diffuse out of the helium core before the whole star recombines. Compared to this range, Equation (14) overestimates the duration by about 10%. Reducing the normalization constant,  $C_f$ , in Equation (14) to 88 days gives a better fit to our models. Thus, for light curves with no radioactive contribution, we recommend

$$t_{\text{p},0} = 88E_{51}^{-1/6}M_{10}^{1/2}R_{0,500}^{1/6} \text{ days.} \quad (17)$$

As pointed out by Kasen & Woosley (2009), the presence of radioactivity does not substantially influence the luminosity during most of the plateau because the diffusion time out of the core is long compared with the recombination time. There are exceptions if the star makes more than about  $0.1 M_{\odot}$  of  $^{56}\text{Ni}$ , or if the progenitor is not a red supergiant (e.g., SN 1987A). The duration of the plateau is another matter, however. Even  $0.01 M_{\odot}$  of  $^{56}\text{Ni}$  can appreciably lengthen it. Radioactivity affects  $t_{\text{p}}$  both by contributing to the energy budget and by keeping the gas ionized longer so that its opacity and diffusion time remain high.

Figure 33 shows light curves due to various amounts of nickel masses for the lightest SN studied,  $9 M_{\odot}$ , and a more “typical” model of  $15.2 M_{\odot}$ . For the lower-mass model,  $^{56}\text{Ni}$  masses over  $0.01 M_{\odot}$  are not physical, and the results shown are purely for comparison. For a realistic amount of  $^{56}\text{Ni}$ , the plateau of the  $9.0 M_{\odot}$  is not appreciably lengthened, but the  $15.2 M_{\odot}$  model is. Note also a bump at the end of the plateau for both zero  $^{56}\text{Ni}$  models, but especially for the higher-mass star. This is the energy diffusing out of the helium core after the hydrogen envelope has recombined. This effect is weaker in the smaller model since the helium core is much smaller.

Following Kasen & Woosley (2009), we adopt a correction factor to the internal energy due to the decay of  $^{56}\text{Co}$ :

$$f_{\text{rad}} = 1 + 24 \frac{M_{\text{Ni}}}{E_{51}} \frac{t_{\text{Co}}}{t_e} \quad (18)$$

where  $M_{\text{Ni}}$  is the mass of  $^{56}\text{Ni}$  produced in the explosion in units of  $M_{\odot}$ ;  $t_{\text{Co}}$  is the mean life of  $^{56}\text{Co}$ , 113 days; and  $t_e$  is a characteristic expansion time given by the initial radius of the star divided by a typical speed,  $v = (2E/M_{\text{env}})^{1/2}$ . Two things worth noting in the derivation are (1) that the decay of  $^{56}\text{Ni}$  itself has no effect on  $t_{\text{p}}$  (this just increases the expansion kinetic energy by a small amount and is neglected), only  $^{56}\text{Co}$  does; and (2) that the derivation implicitly assumes complete mixing, that is, the  $^{56}\text{Co}$  is distributed homogeneously in the star.

In the derivation of the scaling shown in Equation (17) two energies appear that are taken, within a constant multiplier, to be the same, the internal thermal energy,  $E_T$ , and the kinetic energy,  $E_K$ . The scaling actually depends on  $(E_T/E_K^2)^{1/6}$  or  $E^{-1/6}$  if, e.g.,  $E_T = E_K = E$ . Since  $f_{\text{rad}}$  is assumed to only multiply the internal energy, the correction factor enters in as the positive one-sixth power. That is,

$$\begin{aligned} t_{\text{p}} &= t_{\text{p},0} \times f_{\text{rad}}^{1/6} \\ &= t_{\text{p},0} \times (1 + C_f M_{\text{Ni}} E_{51}^{-1/2} M_{10}^{-1/2} R_{0,500}^{-1})^{1/6} \end{aligned} \quad (19)$$

where  $C_f \sim 21$ . This is similar to Equation (13) of Kasen & Woosley (2009), but corrects two typographical errors: (1) the constant  $C_f \approx 21$  and (2)  $M$  is raised to the  $-1/2$  power.

The bottom panel of Figure 32 shows the effect of this correction factor on the plateau duration of models with radioactivity. The same set of 26 models as used in the zero radioactivity case were compared with those in which the calculated amount of radioactivity was turned on. Additional models multiplied the energy generation from radioactivity by two. For progenitor masses above about  $12 M_{\odot}$ , the model results agree well with Equation (19), though there are substantial differences at lower masses. Better agreement with our models is obtained if  $C_f \sim 50$ , and that is our suggested value.

The breakdown below  $12 M_{\odot}$  is not particularly surprising. These low-mass SNe have low energy ( $\sim 10^{50}$  erg), but also low  $^{56}\text{Ni}$  mass ( $< 0.01 M_{\odot}$ ). The combination  $M_{\text{Ni}} E^{-1/2}$  is still appreciable even though the mass of radioactivity itself is very small. If the mass fraction of  $^{56}\text{Ni}$  in a given zone, after mixing, is less than about 0.001, the decay energy,  $6.4 \times 10^{16}$  erg g $^{-1}$ , of  $^{56}\text{Co}$  will, after time  $t_{\text{Co}}$ , be only a small fraction of the internal energy at recombination,  $\sim 10^{15} E_{51}$  erg g $^{-1}$ , and recombination will not be greatly affected. For the very low mass explosions and mixing prescription assumed, the cobalt abundance is below this limiting value in all zones except at the very base of the hydrogen envelope. In any case the correction factor is small, less than 10%, in these low-energy explosions.

Combining our best fit to the no-radioactivity models with this best-fit correction factor results in good agreement with the full set of models with radioactivity included (Figure 34). As expected, most of the large deviations are for the lightest and heaviest stars. For small stars, the scaling relation overestimates the plateau duration because the correction term,  $f_{\text{rad}}$ , is too big. At high mass, there are cases with a large amount of fallback (Figure 13) and therefore no  $^{56}\text{Ni}$  production. Indeed, such

**Table 9**  
Selected Isotopes Production in  $M_{\odot}$

Mass Range	Engine(s)	$^{26}\text{Al}/10^{-5}$	$^{60}\text{Fe}/10^{-5}$	$^{56}\text{Fe}$
9–120	Z9.6+W18	2.80	2.70	0.038
9–120	Z9.6+N20	3.63	3.20	0.052
$\leq 12$	Z9.6	1.36	2.73	0.026
$> 12$	W18	3.17	2.66	0.053
$> 12$	N20	4.22	3.28	0.066

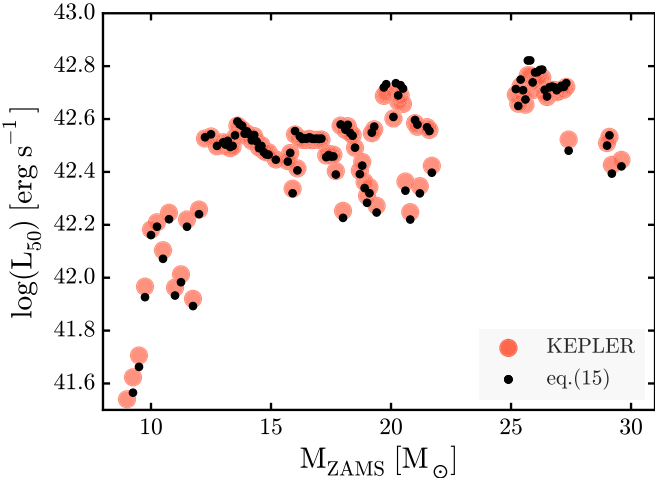


**Figure 31.** Plateau luminosities 50 days post-breakout for the successfully exploded models of the Z9.6 and N20 series (red circles) are compared with Equation (15) (black circles). The agreement is striking. Results for the W18 series are not shown, but are very similar to those of N20.

short plateaus in massive stars with normal luminosities (Figure 31) may be an observable signature of BH formation.

#### 7.1.3. Systematics

Given the generally good agreement of our SNe IIP model characteristics with analytic expressions, it is worth exploring whether these systematics can be exploited to obtain insights into the masses and energies of observed events. Another interesting question is whether SNe IIP, or some subset, can be used as standard candles.

Neglecting the radioactive correction, Equation (19), the luminosity and plateau duration are proportional to powers of the explosion energy, pre-SN radius, and envelope mass. These are not independent variables. The radius of the pre-SN star increases monotonically with its main-sequence mass,  $M_{\text{ZAMS}}$ , and to good approximation in the mass range where most SNe IIP occur ( $9–20 M_{\odot}$ ),  $R_0 \propto M_{\text{ZAMS}}^{3/4}$  (Figure 35). Above  $20 M_{\odot}$ , the hydrogen envelope mass of the pre-SN star declines with  $M_{\text{ZAMS}}$  owing to mass loss, but below  $20 M_{\odot}$ , it too has a monotonic scaling,  $M_{\text{env}} \propto M_{\text{ZAMS}}^{2/3}$ . The explosion energy also tends to increase with mass because of the greater efficiency of neutrino absorption in heavier stars and the larger neutrino luminosity from accretion, but owing to the nonmonotonic behavior of compactness, this is not as well-defined a correlation. The compactness parameter does generally increase with mass, though, especially at low mass (Figure 1), and the explosion energy there is correlated with compactness (Figure 16). Given these correlations, one can

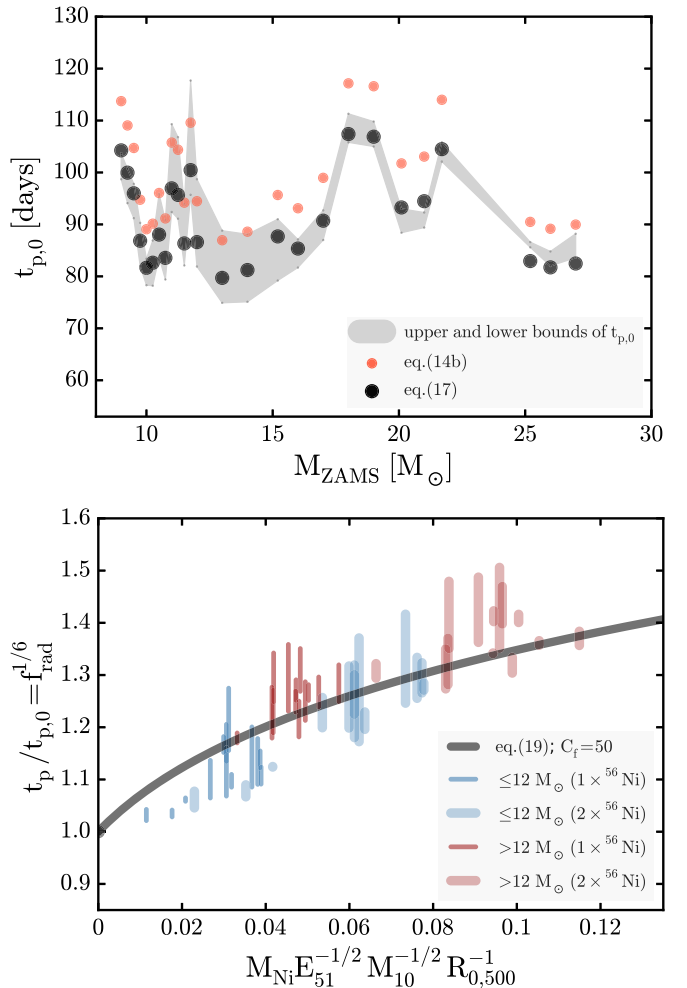


**Figure 32.** Top: plateau durations from a set of 26 models calculated assuming no radioactive decay shown in comparison with Popov's unmodified scaling law (Equation (14)) and a renormalized version. The upper and lower bounds on  $t_{p,0}$  from the models (see text) give the gray shaded region. Equation (14) with  $C_f = 96$  days systematically overestimates the measured durations by about to 10%. The same scaling normalized to  $C_f = 88$  days produces better agreement. Bottom: effect of radioactivity on the plateau duration shown from the same set of models that included no radioactivity ( $t_{p,0}$ ), with the default calculated yields of  $^{56}\text{Ni}$  ( $t_p$ ) and twice that value ( $t_p$ ). Models from progenitors with initial mass larger than about  $12 M_{\odot}$  follow the correction term derived in Equation (19) reasonably well, but smaller models are overestimated. The fit is improved when the constant in the brackets of Equation (19),  $C_f$ , is 50, i.e., the black curve is  $(1 + 50M_{\text{Ni}}E_{51}^{-1/2}M_{10}^{-1/2}R_{0,500}^{-1})^{1/6}$ .

derive some simple relations among the luminosity, energy, duration, and main-sequence mass.

First, consider the width-luminosity relation for SNe IIP. Figure 36 shows  $L_{50}$  versus  $t_p$  with  $t_p$  measured from breakout until the onset of the radioactive tail. The results have been segregated by mass groups, and the explosions used the Z9.6 and N20 central engines. The scaling relations (Equation (14)) predict  $L_{50}t_p^3 \propto E_{51}^{1/3}M_{10}R_{0,500}^{7/6}$ . From  $12.25$  to  $20 M_{\odot}$ , roughly half of all SNe, the energy and envelope mass change only a little and the radius increases by only 30%, so crudely one expects  $L_{50} \propto t_p^{-3}$ , which is approximately what the figure shows. For stars with  $t_p$  near 110 days, most SNe have a standard bolometric luminosity between  $\log L = 42.45$  and 42.58.

Unfortunately, the low-mass SNe, with their unusually low energy explosions, contaminate an otherwise nice relation.

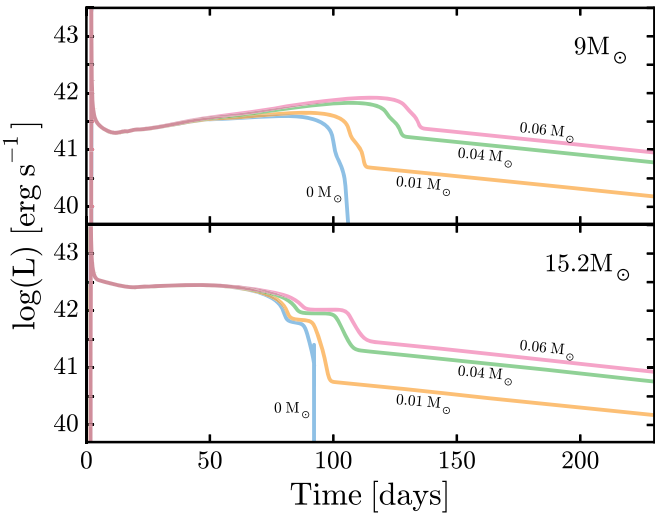


**Figure 33.** Light curves due to various amounts of nickel masses are shown for the  $9.0 M_{\odot}$  model of the Z9.6 series (top) and the  $15.2 M_{\odot}$  model from the N20 series. The KEPLER model gave  $0.004 M_{\odot}$  nickel for the  $9.0 M_{\odot}$  model and  $0.070 M_{\odot}$  for the  $15.2 M_{\odot}$  model. Energy generation from the decay of these masses was multiplied by a constant to simulate the production of various amounts of  $^{56}\text{Ni}$ , and the resulting curves are shown.  $^{56}\text{Ni}$  masses of more than  $0.01 M_{\odot}$  for the  $9.0 M_{\odot}$  model are unlikely, but shown for comparison.

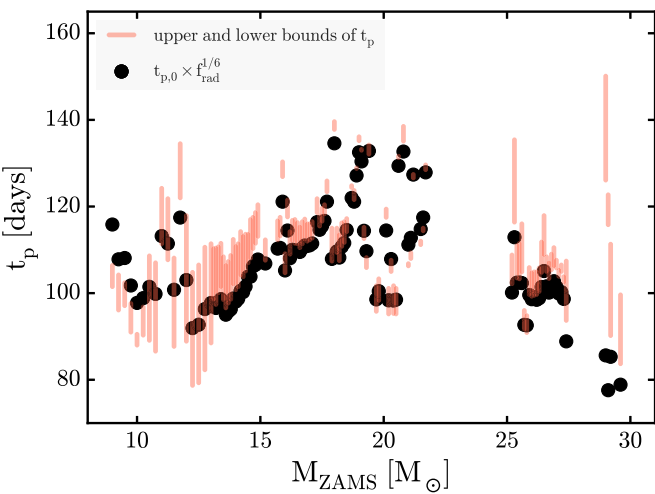


**Figure 34.** The scaling laws that showed good agreement in Figure 32 are now compared against the standard explosion models with their  $^{56}\text{Ni}$  included. The models used are from the Z9.6 and N20 series. A red vertical bar represents a range of possible plateau durations calculated from the models assuming that (1) the photospheric radius had receded to 50% of its maximum value (lower bound) or (2) the whole star had recombined (upper bound). Black points result from multiplying Equation (14) with  $C_t = 88$  by the correction term, Equation (19), with  $C_f = 50$ .

These might be selected against on the basis of their low photospheric speeds or even by their colors, but that lies beyond the scope of the present work. Our large model set will be available (see footnote 4) and represents a resource from which information on dilution factors and spectral velocities, for example, could be extracted. These could be useful for the expanding photosphere method for distance determination (e.g., Eastman et al. 1996; Vinkó et al. 2012).

Next, consider the kinetic energy of the explosion. Can it be determined just from observations of the light curve? Figure 35 shows a well-defined relation between the bolometric luminosity

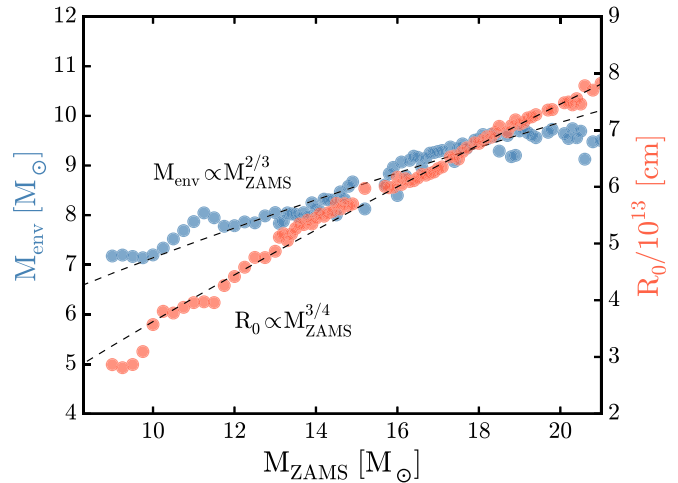


**Figure 35.** Scaling of the envelope mass and radius with the initial mass for progenitors below  $21 M_{\odot}$ . The radius scales as  $M_{\text{ZAMS}}^{3/4}$ , while the envelope mass scales approximately as  $M_{\text{ZAMS}}^{2/3}$ . The envelope mass peaks near  $20 M_{\odot}$  and begins to decline at higher mass owing to mass loss, so these scalings cannot be used outside the range shown. Additional progenitor information is given in Table 2.

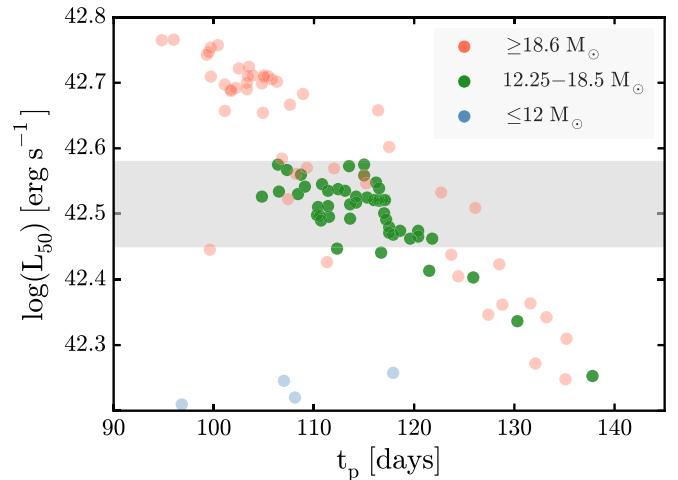


**Figure 36.** Correlation between the plateau luminosities and durations shown for the exploded models based on the Z9.6 and N20 engines. The plateau duration here is an upper bound, the starting time of the radioactive tail when the full star has recombined. Green points, which represent 35% of all SNe, show a strong clustering. Above  $\log L_{50} = 42.3 \text{ erg s}^{-1}$ , the luminosity is clearly anticorrelated with the plateau duration. The low-mass models from series Z9.6 all have luminosities well below the gray box, and some of them have  $\log L_{50}$  below  $42.2 \text{ erg s}^{-1}$  and fall on the plotted grid.

on day 50 (after shock breakout) and the kinetic energy of the SN. This is expected on the basis of Equation (15), which shows the luminosity scaling as  $E_{51}^{5/6} M_{10}^{-1/2} R_{0.500}^{2/3}$ . From 9 to  $20 M_{\odot}$ , which includes about 95% of successful SN IIp explosions, the hydrogen envelope mass varies between  $7$  and  $10 M_{\odot}$  and is usually  $8$  or  $9 M_{\odot}$ . The radius varies by about a factor of 3, but enters as a  $2/3$  power. Moreover, the radius scales as  $R \propto M^{3/4}$ , and higher-mass stars tend to have bigger explosion energies. Thus, the fact that the luminosity scales roughly as the explosion energy is not surprising.

The figure shows, though, that just by measuring the bolometric luminosity on the plateau, one gets a good estimate of the total explosion energy. Models above  $22 M_{\odot}$  lie off the

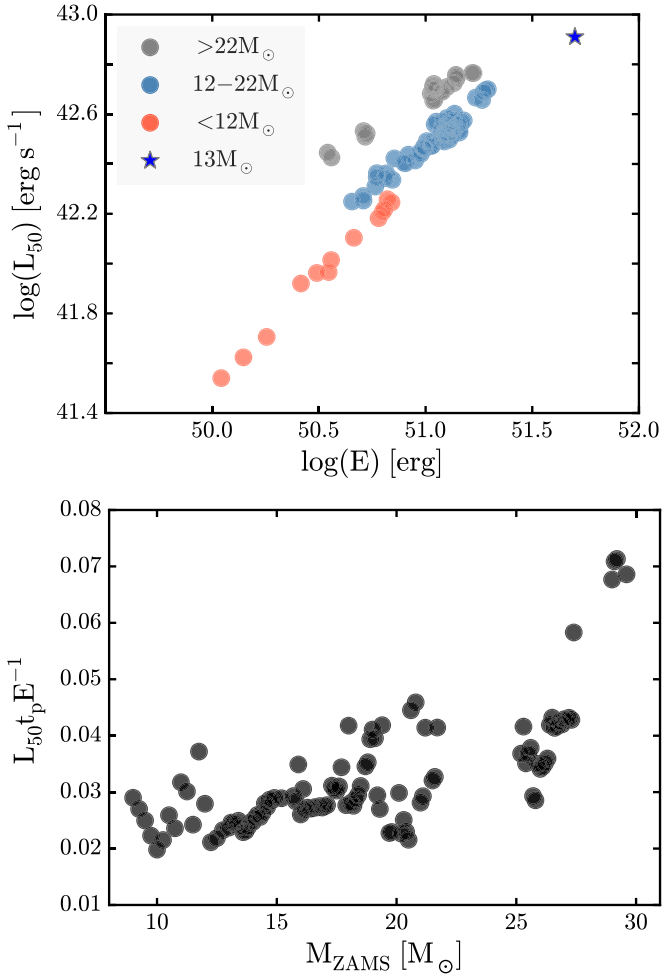


**Figure 37.** Top: correlation between plateau luminosities at 50 days and the explosion energies for Z9.6 and N20 engines. The  $13 M_\odot$  model from the N20 engine has been recalculated with the explosion energy scaled up to  $5 \times 10^{51}$  erg and is plotted as a single blue star. Explosions from stars smaller than  $22 M_\odot$ , which are most SNe, show a strong positive correlation of luminosity with energy. Bottom: ratio of  $L_{50} t_p$  and explosion energy shown as a function of initial progenitor mass. Integration of the light curve shows that  $L_{50} t_p$  is an accurate proxy for the total radiated energy. The typical SN IIP radiates 2%–4% of its explosion energy as light.

main curve, but there are very few such explosions. These plots include only the contributions of radioactivity and a point explosion, and not any contribution from a magnetar or circumstellar interaction. An inferred explosion energy above  $2 \times 10^{51}$  erg would be suggestive of a breakdown in this assumption.

Also shown in Figure 37 is the quantity  $L_{50} t_p / E$  versus progenitor initial mass. This is the ratio of the total power emitted by the SN on its plateau to the kinetic energy of the explosion and is expected to scale as  $E_{51}^{-1/3} R_{0.500}^{5/6}$ . Since  $E_{51}$  generally increases with mass and therefore with radius, the figure shows that  $L_{50} t_p / E$  is roughly constant. The total radiated energy in light for most neutrino-powered SNe is roughly 1/35 of the kinetic energy of the explosion. The full range of this ratio between 9 and  $20 M_\odot$  is 0.02–0.04. This gives another way of estimating the energy of a neutrino-powered SN from observables,  $L_{50}$  and  $t_p$ .

Finally, we consider whether the mass of the ZAMS star can be determined from the SN light curve. Figure 38 shows

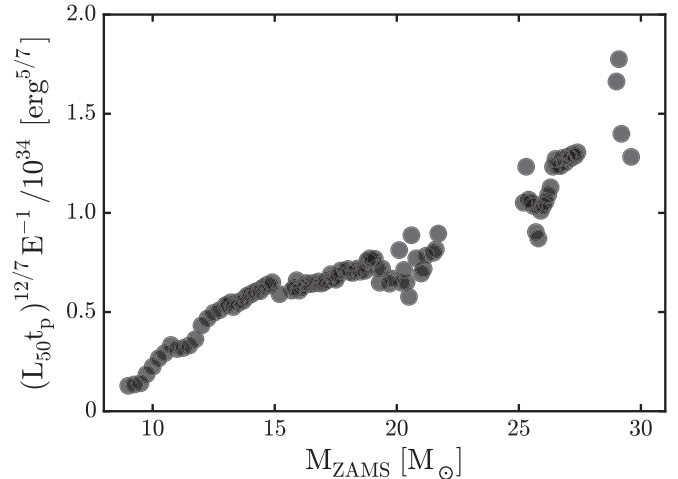


**Figure 38.** Quantity  $(L_{50} t_p)^{12/7} E^{-1}$  plotted against the ZAMS mass of the progenitor shown for all exploded models of Z9.6 and N20 engines. This correlation allows an approximate determination of the progenitor mass given measurements of plateau luminosity and duration along with an explosion energy estimated from Figure 37.

quantity  $(L_{50} t_p)^{12/7} / E$ , which should scale as  $R^{10/7}$ , plotted against  $M_{\text{ZAMS}}$ . Since  $R \propto M_{\text{ZAMS}}^{3/4}$ , this implies that  $(L_{50} t_p)^{12/7} / E$  should scale as  $M_{\text{ZAMS}}^{15/14}$ , which is consistent with Figure 38. If one observes  $L_{50}$  and  $t_p$  and determines the explosion energy from Figure 37, the ZAMS mass of an SN in our data set is roughly determined.

## 7.2. Type Ib/c

With the adopted mass-loss prescription, stars with initial mass greater than about  $35 M_\odot$  lose all of their hydrogen envelope before dying. Successful explosions will then produce SNe of Type Ib and Ic. Models heavier than  $\geq 45 M_\odot$  have lost most of their helium envelope and all have surface  ${}^4\text{He}$  mass fractions less than 0.2 (Table 2); however, the exact distinction between Ib and Ic is as much dependent on mixing as on mass loss (Dessart et al. 2011), and we shall not attempt to separate the two classes in this work. Use of the N20 engine resulted in the explosion of the  $60, 80, 100, 120 M_\odot$  progenitors, while the W18 engine exploded only the  $60$  and  $120 M_\odot$  progenitors. The resulting light curves are shown in the bottom panel of Figure 30.

These are not common SNe Ib or SNe Ic. Their light curves are too broad and faint. Presumably common SNe Ib and Ic come from mass-exchanging binary star systems and lower-mass progenitors (Dessart et al. 2011; Eldridge et al. 2013). The SNe here are bigger and more slowly expanding, but should exist in nature and might be sought as a separate subclass of Type Ibc. Since the neutrino mechanism appears inadequate to produce an explosion energy greater than about  $2 \times 10^{51}$  erg (Ugliano et al. 2012; Ertl et al. 2015), these would be fainter and broader than, e.g., SN 2009ff (Valenti et al. 2011). Conversely, events with much greater energy than  $2 \times 10^{51}$  erg would not be powered exclusively by neutrinos.

These Type Ibc light curves have peak luminosities larger than predicted by “Arnett’s rule” (Arnett 1982), which states that  $L_{\text{peak}} = L_{\text{decay}}(t_{\text{peak}})$ . Consequently, the nickel mass content cannot be accurately inferred in the same way as for SNe Ia. Dessart et al. (2015) studied similar light curves and found that the energy-conservation-based arguments of Katz

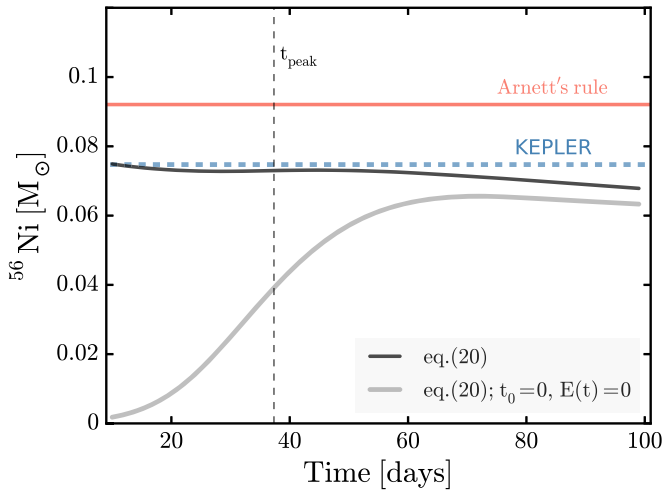


**Figure 39.** Estimates of the  $^{56}\text{Ni}$  mass for the  $80 M_{\odot}$  progenitor exploded using the N20 engine. The KEPLER calculation synthesized  $0.074 M_{\odot}$  of  $^{56}\text{Ni}$ . The energy conservation argument described in Equation (20) closely agrees with this value until late times when the leakage of gamma rays becomes significant. The special case of this argument presented in Katz et al. (2013) for Type Ia light curves underestimates the nickel mass, but works better than Arnett’s rule.

et al. (2013) gave better agreement. Their argument follows from the first law of thermodynamics and the assumption that the ejecta are freely coasting, radiation dominated, and powered only by radioactivity. Then

$$tE(t) - t_0E(t_0) = \int_{t_0}^t t'L_{\text{dec.}}(t')dt' - \int_{t_0}^t t'L_{\text{rad.}}(t')dt' \quad (20)$$

where  $L_{\text{rad.}}$  is the radiated luminosity and  $E$  is the internal energy of the ejecta. In the special case where  $t_0 = 0$ ,  $t$  is sufficiently large such that  $E(t) \approx 0$ , and  $L_{\text{rad.}} = L_{\text{bolometric}}$ , the argument reduces to a connection between an observable (bolometric luminosity) and a physical quantity ( $^{56}\text{Ni}$ ).

Figure 39 illustrates this method applied to one of our models. The approximation works until about 60 days post-explosion (black curve), after which the leakage of gamma rays becomes significant. If one assumes full trapping, Equation (20) will hold as long as the radiation dominates the internal energy. Some deviation is expected because the internal energy is not all in the form of radiation; an appreciable fraction is in the electrons.

In the special case when  $t_0 = 0$  and  $E(t) = 0$ , Equation (20) expresses the equality between the two integrals. At around 70 days the nickel mass inferred from this relation peaks and reaches its closest point with respect to that in the actual model (blue dashed line). After the peak, it goes down again owing to leakage, but it does not quite reach the “true” value because the internal energy is not small enough at that time. At 70 days the internal energy is roughly  $2 \times 10^{47}$  erg, only about 3 times less than its value at 3 days. Though it underestimates the nickel mass, this method is more accurate than “Arnett’s rule” for all of our Ib and Ic models.

### 7.3. Type III

None of the exploded models from the Z9.6, W18, and N20 engines showed a clearly linear decline after the shock breakout. All of the explosions from progenitors smaller than  $30 M_{\odot}$  showed a plateau of roughly constant luminosity. The

shortest plateau, as measured by the lower bound, was 79 days for the  $12.25 M_{\odot}$  model with a  $7.8 M_{\odot}$  envelope. And the exploded model with the least amount of envelope mass, the  $29.6 M_{\odot}$  model of the N20 engine with a  $3.9 M_{\odot}$  envelope, yielded an 84-day-long plateau. Given that Type III should come from at least some stars in the  $9$ – $120 M_{\odot}$  range, their absence warrants an explanation.

There are several possibilities. We may just have missed them because of sparse mass sampling above  $35 M_{\odot}$ . This is unlikely. Type III is expected to come from a star that has lost most of its hydrogen envelope, but retains a large radius and, possibly, makes a lot of  $^{56}\text{Ni}$ . Our model set indeed had  $5 M_{\odot}$  spacing from 35 to  $60 M_{\odot}$ , but none of those stars blew up.

Second, their absence may reflect a deficiency in pre-SN modeling. This is quite possible. Over the years, one of us has noted a chronic problem calculating ab initio models of very massive stars with envelope masses below  $1 M_{\odot}$  using KEPLER. The envelopes expand to such large radii (over  $10^{14}$  cm) that they begin to recombine. Density and even pressure inversions develop near the surface, and the calculation cannot be carried further. Such was the case with the  $35 M_{\odot}$  model studied here and in Woosley & Heger (2007). At central helium depletion this star had an extended low-density envelope of about  $1 M_{\odot}$  with a radius of  $8.3 \times 10^{13}$  cm and a luminosity of  $1.35 \times 10^{39}$  erg s $^{-1}$ , only slightly below the Eddington limit for its remaining mass,  $15 M_{\odot}$ . As the star attempted to adjust its structure and ignite carbon, its luminosity increased above  $1.6 \times 10^{39}$  erg s $^{-1}$ , and the envelope became unstable. It is quite possible that at this point the envelope comes off. The central temperature was over  $5 \times 10^8$  K, and it would not have been long before the star died. Fortunately perhaps, there is no way that neutrinos would blow up this model, so this behavior is not an issue for the present paper, but a similar fate might befall a lower-mass star in a binary system, or the KEPLER calculation may just be wrong. More study is clearly needed.

Finally, it should be noted that the mass range where Type III might have occurred,  $30$ – $40 M_{\odot}$ , is also a mass range where the effects of rotation are expected to be important to the death of the star (Heger et al. 2005).

SNe III could thus be a consequence of collisions with recently ejected envelopes, binary systems, jets, magnetars, stellar evolution still to be done properly, or all five, and that makes them interesting.

## 8. CONCLUSIONS

The deaths of massive stars from  $9.0$  to  $120 M_{\odot}$  as SNe have been surveyed using an improved depiction of the explosion physics. Models are one-dimensional, of a single metallicity (solar), and do not include any effects of rotation. Nevertheless, they capture many essential aspects of a general solution neglected in past studies, including the explosion effects of a nonmonotonic variation of the pre-SN compactness (Figure 1) with mass. The explosions are calibrated to reproduce the characteristics of two well-studied SNe: the Crab and SN 1987A. The Crab is believed to have been a low-mass SN, near  $10 M_{\odot}$ , with a low explosion energy,  $\sim 10^{50}$  erg, that made very little iron. SN 1987A was a star near  $18 M_{\odot}$  that exploded with  $1.3 \times 10^{51}$  erg and made  $0.07 M_{\odot}$  of  $^{56}\text{Ni}$ . These two calibration points anchor our survey. Multiple models for the central engine for 87A were employed and one for the Crab.

Calibrating to these two events, and using lessons learned from previous 3D modeling efforts of core collapse, results in fiducial “central engines” that describe the evolution of only the inner  $1.1 M_{\odot}$  of the collapsing iron core (Section 3.1). These central engines, or inner boundary conditions, are characterized by just a few physically descriptive parameters (Table 3). These inner core evolution prescriptions are then used to follow the evolution of 200 pre-SN stars (Section 2.3; Table 2) in the mass range  $9.0$ – $120 M_{\odot}$ . Outside  $1.1 M_{\odot}$ , neutrino transport was followed in an approximate, efficient way for each stellar model, thus assuring a physical representation of the explosion that was sensitive to the structure of individual pre-SN stars. Above  $12 M_{\odot}$ , five central engines for various SN 1987A models were employed, two of them extensively. From  $9.0$  to  $12 M_{\odot}$ , the properties of the central engine were interpolated between Crab-like and 87A-like behavior. The Crab model itself was based on a  $9.6 M_{\odot}$  star whose explosion has been previously studied in 3D.

As a result of these simulations, a large diversity of successful and failed explosions was generated. Kinetic energies at infinity varied from  $0.11 \times 10^{51}$  to  $2.03 \times 10^{51}$  erg. The outcome of each calculation depended on the structure of the pre-SN star and central engine employed. All stars below  $12 M_{\odot}$  exploded, albeit weakly. Despite their small compactness parameters and ease of explosion, their final energies were low because a smaller fraction of the neutrino power radiated by the PNS was converted into kinetic energy of expansion. The steep density gradient outside the iron core reduced the absorption. Conversely, larger stars trapped a larger proportion of the neutrino radiation and had a bigger neutrino luminosity from accretion, but also had a larger binding energy and ram pressure to overcome. Some exploded with variable energy up to  $2 \times 10^{51}$  erg; some not at all.

There was no single mass below which all stars exploded and above which BHs formed, but rather there were islands of “explodability” in a sea of BH formation (Figure 13). A similar result was found by Pejcha & Thompson (2015), suggesting that the outcome of SN explosions is more influenced by pre-SN structure than details of the central engine, provided that that engine is sufficiently powerful to explode many stars. Stars above  $35 M_{\odot}$  lost their envelopes, and a few that experienced severe mass loss as Wolf-Rayet stars exploded as SNe Ibc, but most became BHs. Typically 95% of the stars that did explode were SNe IIp with masses less than  $20 M_{\odot}$  (Table 4). The median SN mass, neglecting any explosions below  $9 M_{\odot}$ , was  $12 M_{\odot}$ . Half were heavier and half lighter. The heavier half accounted for most of the nucleosynthesis.

From the baryonic masses of the remnants, it was possible to create a distribution of neutron star masses and an average. Both agreed very well with observations (Table 4 and Figure 18), with typical neutron star gravitational masses near  $1.40 M_{\odot}$ . The heaviest neutron star made was  $1.77 M_{\odot}$ , and the lightest,  $1.23 M_{\odot}$ . While electron-capture SNe were not computed here, their neutron stars should result from the collapse of Chandrasekhar mass cores with  $Y_e$  still close to 0.50. The neutron stars resulting from our  $9$  and  $10 M_{\odot}$  models, which have experienced appreciable electron capture during oxygen and silicon burning prior to collapse, can actually be lighter.

For those stars that made BHs, which were most, but not all, of the stars above  $20 M_{\odot}$  and some below  $20 M_{\odot}$ , only a few

produced their BHs by fallback. Stars that in past surveys produced BHs by fallback more frequently did not explode at all in the present study.

The present calculations with P-HOTB also included a contribution to the explosion energy from the neutrino-powered wind and from recombination, of order  $10^{49}$ – $10^{50}$  erg, that gave an extra push to the inner zones during the first second or so after the shock was launched. This helped to prevent their reimplosion. Usually BH production involved the collapse of the full star, including its hydrogen envelope. Other mechanisms are necessary and were invoked to explain envelope ejection during BH formation. If the full pre-SN star always collapsed, the average BH mass (IMF weighted) was  $13.3$ – $13.8 M_{\odot}$ ; if only the helium core collapsed, it was  $7.7$ – $9.2 M_{\odot}$  (Table 4). The latter is in better agreement with observations and suggests that BH formation is accompanied by weak explosions that eject only the hydrogen envelope. These weak SNe would have distinctive light curves and colors. The gap between neutron stars and BH masses from  $\sim 2$  to  $\sim 4 M_{\odot}$  suggested by observations was naturally obtained because of the lack of fallback SNe that could fill this mass interval.

One important result of this study is the nucleosynthesis expected from massive stars calculated using the more realistic depiction of explosion. This was calculated using the KEPLER code and an amply large nuclear reaction network complete up to the element bismuth. A trajectory near the final mass cut in P-HOTB was taken as the inner boundary for the KEPLER calculation, and the infall and time of reversal were nearly the same. The velocity of the piston in KEPLER was varied, however, to give near perfect agreement in explosion energy with the P-HOTB calculations and to reproduce the iron synthesis to better than 10% in most cases. In a few cases the latter required a slight adjustment of the piston mass. Neutrino interactions, except for the neutrino process of nucleosynthesis, were neglected in the KEPLER studies, and the neutrino-powered wind was not carried. In practice, this meant the neglect of a possible  $r$ -process or  $\nu p$ -process component and some uncertainty in the nucleosynthesis of nickel, copper, and zinc.

The contributions from various-mass stars were then determined, as well as their overall IMF-weighted production factors. The lighter SNe below  $12 M_{\odot}$ , half of all SNe numerically, make a relatively small contribution to the overall nucleosynthesis, but are important for some elements. Carbon, nitrogen, lithium, boron, and fluorine, as well as numerous species in the iron group, were produced in solar or supersolar proportions to oxygen (Figure 21). Besides their contribution to Population I nucleosynthesis in nature, these abundances are also of interest for the large fraction of SN remnants they would characterize. The iron-to-oxygen ratio was nearly normal, despite the fact that overall the massive stars only account for a minor fraction of the iron in the Sun (Section 6.4.3 and Wheeler et al. 1989; Meléndez & Barbui 2002; Chiappini et al. 2003). Boron was unusually high owing to the operation of the neutrino process in a shell close to the neutron star with a large abundance of carbon.

Explosions from  $12$  to  $30 M_{\odot}$  are responsible for most of the nucleosynthesis. The elemental production pattern (Figure 22) is consistently solar from boron to copper, with the expected deficiency in the iron group due to SN Ia production. Carbon, nitrogen, and fluorine are also greatly reduced compared with

the low-mass SNe. In general, there is a tendency to slightly underproduce the intermediate-mass elements, Si, S, Ar, and Ca, with respect to oxygen. This may indicate a smaller than optimal abundance for oxygen in the Sun, or the lack of some other component, e.g., SNe Ia. The *s*-process production, from Cu to Zr, is less than in previous works (e.g., Woosley & Heger 2007) and is problematic.

Above  $30 M_{\odot}$ , there were few explosions, but even stars that make BHs still contribute their winds (Figure 23). Because mass-loss rates are uncertain, the nucleosynthesis of these stars must be treated with caution. For standard assumptions, carbon and oxygen are substantially produced in the winds of massive Wolf–Rayet stars, and nitrogen, neon, and sodium also have important components. Indeed, the abundances of these light elements are so great that stars in this mass range make little else when the other productions are normalized to them.

Integrating over the entire full range from 9 to  $120 M_{\odot}$ , and examining isotopes as well as elements, the nucleosynthesis bears strong resemblance both to the solar pattern and to the earlier survey by Woosley & Heger (2007), but with notable exceptions.  $^{12}\text{C}$  and  $^{22}\text{Ne}$  are slightly overproduced. This might be an indication that the mass-loss rates used here are high by about a factor of two, but the  $^{22}\text{Ne}$  yield would also be reduced in stars with less than solar metallicity, because of the smaller neutron excess. C and O production in the winds of low-metallicity stars would also be reduced. The excesses would instead end up in BHs. A full galactic chemical evolution model would need to be done to see whether these overproductions are problematic. Fluorine is underproduced by a factor of two, suggesting a possible contribution from lower-mass stars. Radioactive  $^{40}\text{K}$  is greatly overproduced, but this is not a problem since a large uncertain fraction of the radioactive species would decay before the Sun was born. The iron group retains the underproduction seen in the intermediate-mass explosions, but some copper and nickel are slightly overproduced, possibly owing to the neglect of neutrino interactions at the base of the ejecta. Also notable are the deficient productions of  $^{44}\text{Ca}$  and  $^{55}\text{Mn}$  and of the *s*- and *p*-processes.

In fact, above the iron group, the fit to solar abundances is substantially poorer than in Woosley & Heger (2007), which used essentially the same stellar physics but an inferior model for the explosion. The underproductions are a consequence of many massive stars that were once prolific sources of the *s*-process now imploding to BHs. To a lesser extent, it also reflects the use of a rate for the  $^{22}\text{Ne}(\alpha, n)^{25}\text{Mg}$  reaction that is about  $\sim 50\%$  smaller than a recent reanalysis of experimental data. Given the critical role of the light *s*-process as a diagnostic here, our calculations should be repeated with a variable value for this rate to test the sensitivity of the outcome. The heavy *p*-process is also underproduced compared both with the Sun and with the results from Woosley & Heger (2007). This again reflects a deficiency of massive star explosions with thick layers that experience explosive neon burning. The origin of the light *p*-process below  $A = 130$  and specifically of the nucleus  $^{92}\text{Mo}$  continues to be a mystery. In total, the nucleosynthesis would be improved if more massive stars blew up (Brown & Woosley 2013).

More  $^{26}\text{Al}$  is produced relative to  $^{60}\text{Fe}$  than in the 2007 survey because some of the major producers of  $^{60}\text{Fe}$  now make BHs. This is good news, but should be treated cautiously because the same changes necessary to increase light *s*-process production might also increase the yield of  $^{60}\text{Fe}$ . The

production ratio from the present survey for  $^{60}\text{Fe}/^{26}\text{Al}$ , averaged over a Salpeter IMF, is, by mass,  $\sim 0.90$ . The observed value is  $0.35 \pm 0.1$ . The Woosley & Heger (2007) survey gave 1.8. Part of the remaining discrepancy probably has to do with uncertain reaction rates.

As is well known, the underproduction of iron in massive stars is actually desirable since most of iron comes from SNe Ia. Here we find that 28% of the solar abundance relative to oxygen is made in massive stars. Since both are primary elements whose synthesis is independent of neutron excess, the same ratio would probably characterize low-metallicity stars. If the SN Ia rate is at least 1/6 to 1/5 of the SN IIp rate, then iron is made in solar proportions. Roughly comparable contributions from both sub-Chandrasekhar mass models and the traditional Chandrasekhar mass model are needed, however, to produce both  $^{44}\text{Ca}$  and  $^{55}\text{Mn}$ . The sub-Chandrasekhar mass model also helps boost the deficient production of the alpha nuclei from silicon through calcium.

The excellent agreement of  $^{11}\text{B}/^{16}\text{O}$  in the integrated sample provides an accurate measure of the  $\mu$ - and  $\tau$ -neutrino temperature during PNS evolution.

A total of 194 SN light curves were calculated. The vast majority of these were SNe IIp, but the successful explosions over  $30 M_{\odot}$  made a variety of SNe Ibc. These are not the common SNe Ibc, though, because they are too faint and broad. Presumably the common events come from lower-mass explosions stripped of their envelopes in binary systems. The massive faint variety should exist in nature, though, and should be sought.

The 181 SN IIp models are a community resource that is freely available (see footnote 4), and they offer a rich opportunity for modeling the spectrum and colors of a large comprehensive sample with standard identical physics. Here we analyzed (Section 14) the bolometric light curves using semianalytic approximations from Popov (1993) and Kasen & Woosley (2009). While the range in plateau luminosities spans one and a half orders of magnitude, its systematics are amazingly well represented by the analytic formulae (Figure 31). This shows that the systematics are well understood and encapsulated in simple scaling relations, lending confidence to the proposition that, with additional constraints from the spectrum, colors, dilution factor, etc., SNe IIp may be useful cosmological yardsticks.

Figure 37 shows a tight correlation between SN IIp luminosity on the plateau and its total explosion energy. This is well worth checking with an observational sample with spectroscopically determined kinetic energies. It also gives a useful tool for finding “unusual” SNe. None of our explosions exceeded  $2.03 \times 10^{51}\text{ erg}$ , and none were brighter than  $10^{42.7}\text{ erg s}^{-1}$ . An SN IIp brighter than this, say,  $10^{43}\text{ erg s}^{-1}$ , then is not powered by neutrinos. This gives a physical basis for discerning “superluminous” SNe of Type IIp. Figure 37 also shows that the fraction of kinetic energy that comes out as light in a neutrino-powered SN IIp is roughly constant,  $\sim 3\% \pm 1\%$  for the 95% of SNe IIp lighter than  $21 M_{\odot}$ .

While the width–luminosity relation for SNe IIp is not nearly so tight or “calibratable” as for SNe Ia, typical SNe IIp of a given plateau duration have the same luminosity at day 50 to about  $\pm 25\%$  (Figure 36). This is not true, however, for a substantial sample of low-energy SNe below  $12 M_{\odot}$ . These would need to be spectroscopically distinguished on the basis of their low photospheric speed.

With less precision, the mass of the SN progenitor can also be determined from measurements of the total radiated light (to good approximation  $L_{50} t_p$ ) and estimates of the explosion energy (Figure 38). The figure is especially useful for distinguishing low-mass SNe but loses utility in separating SNe in the mass range  $13\text{--}21 M_\odot$  because of the much slower variation of integrated light in this range. In practice, the need to determine the explosion energy accurately may limit the application.

The success of the present approach in fitting many observational constraints, including neutron star masses, BH masses, SN kinetic energies, light curves, and nucleosynthesis, is gratifying and gives hope that it may be more broadly applied in the future. The existence of a large set of models with controlled, well-understood physics will be useful for the statistical analysis of large data sets in the future. There is surely room for improvement, though. Nuclear reaction rates need updating, and the effect of varying the mass loss should be explored. Rotation can be included in the pre-SN models and approximated in the explosion. A broader range of metallicities can be explored. The core physics, currently 1D and calibrated using just two observed events, can be improved by calibrating to a greater range of 3D simulations and observations. The survey can be done in 2D to capture essential aspects of the mixing, and the neutrino wind included in the yields. Given the vast amount of data expected in the near future from large dedicated transient surveys, the effort is worth it and it will happen.

For now, though, we offer not only the results and analysis in this paper but all pre-SN models, exploded models, nucleosynthetic yields, and the light curves in the electronic edition, as well as at the MPA-Garching archive (see footnote 4).

We thank Alex Heger for the data of his Z9.6 progenitor model, his numerous contributions in developing the KEPLER code, and many insights into the topics of this paper. The help of Feryal Özal with comparing our neutron star masses with observational data and of Gabriel Martínez-Pinedo with our analysis of  $^{19}\text{F}$  production is also appreciated. T.E. and H.-T.J. thank L. Hüdepohl, T. Melson, M. Ugliano, and A. Wongwathanarat for numerical support and R. Hix and F.-K. Thielemann for providing the NSE solver introduced into P-HOTB by K. Kifonidis. This work was supported by NASA (NNX14AH34G) and the UC Office of the President (12-LR-237070). At Garching, funding by Deutsche Forschungsgemeinschaft through grant EXC 153 “Excellence Cluster Universe” and the European Research Council through grant ERC-AdG No. 341157-COCO2CASA is acknowledged.

## REFERENCES

- Arcavi, I., Gal-Yam, A., Cenko, S. B., et al. 2012, *ApJL*, **756**, L30  
 Arcones, A., Janka, H.-T., & Scheck, L. 2007, *A&A*, **467**, 1227  
 Arnett, W. D. 1982, *ApJ*, **253**, 785  
 Arnett, W. D., Bahcall, J. N., Kirshner, R. P., & Woosley, S. E. 1989, *ARA&A*, **27**, 629  
 Bouchet, P., Phillips, M. M., Suntzeff, N. B., et al. 1991, *A&A*, **245**, 490  
 Brown, J. M., & Woosley, S. E. 2013, *ApJ*, **769**, 99  
 Buchmann, L. 1996, *ApJL*, **468**, L127  
 Burbidge, E. M., Burbidge, G. R., Fowler, W. A., & Hoyle, F. 1957, *RvMP*, **29**, 547  
 Burrows, A. 2013, *RvMP*, **85**, 245  
 Cayrel, R., Depagne, E., Spite, M., et al. 2004, *A&A*, **416**, 1117  
 Chabrier, G. 2003, *PASP*, **115**, 763  
 Chiappini, C., Romano, D., & Matteucci, F. 2003, *MNRAS*, **339**, 63  
 Chugai, N. N., & Utrobin, V. P. 2014, *AstL*, **40**, 291  
 Costa, V., Pumo, M. L., Bonanno, A., & Zappalà, R. A. 2006, *A&A*, **447**, 641  
 Couch, S. 2013, *ApJ*, **775**, 35  
 Crowther, P. A., Lennon, D. J., & Walborn, N. R. 2006, *A&A*, **446**, 279  
 Dessart, L., Hillier, D. J., Li, C., & Woosley, S. 2012, *MNRAS*, **424**, 2139  
 Dessart, L., Hillier, D. J., Livne, E., et al. 2011, *MNRAS*, **414**, 2985  
 Dessart, L., Hillier, D. J., Woosley, S., et al. 2015, *MNRAS*, **453**, 2189  
 Eastman, R. G., Schmidt, B. P., & Kirshner, R. 1996, *ApJ*, **466**, 911  
 Eldridge, J. J., Fraser, M., Smartt, S. J., Maund, J. R., & Crockett, R. M. 2013, *MNRAS*, **436**, 774  
 Enzman, L. M., & Woosley, S. E. 1988, *ApJ*, **333**, 754  
 Ertl, T., Janka, H.-Th., Woosley, S. E., Sukhbold, T., & Ugliano, M. 2015, *ApJ*, **818**, 124  
 Fischer, T., Whitehouse, S. C., Mezzacappa, A., Thielemann, F.-K., & Liebendörfer, M. 2010, *A&A*, **517**, A80  
 Foglizzo, T., Kazeroni, R., Guilet, J., et al. 2015, *PASA*, **32**, e009  
 Fransson, C., & Kozma, C. 2002, *NewAR*, **46**, 487  
 Fröhlich, C., Martínez-Pinedo, G., Liebendörfer, M., et al. 2006, *PhRvL*, **96**, 142502  
 Hamuy, M. 2003, *ApJ*, **582**, 905  
 Hanke, F., Marek, A., Müller, B., & Janka, H.-T. 2012, *ApJ*, **755**, 138  
 Heger, A., & Woosley, S. E. 2010, *ApJ*, **724**, 341  
 Heger, A., Woosley, S. E., & Spruit, H. C. 2005, *ApJ*, **626**, 350  
 Higdon, J. C., & Lingenfelter, R. E. 2003, *ApJ*, **590**, 822  
 Hoffman, R. D., Woosley, S. E., Fuller, G. M., & Meyer, B. S. 1996, *ApJ*, **460**, 478  
 Humphreys, R. M., & McElroy, D. B. 1984, *ApJ*, **284**, 565  
 Iglesias, C. A., & Rogers, F. J. 1996, *ApJ*, **464**, 943  
 Israel, M. H., Binns, W. R., Christian, E. R., et al. 2015, Proc. ICRC, Cosmic Ray Physics: Experimental Results (Trieste: SISSA), 275  
 Iwamoto, K., Brachwitz, F., Nomoto, K., et al. 1999, *ApJS*, **125**, 439  
 Janka, H.-T. 2012, *ARNPS*, **62**, 407  
 Janka, H.-T., Hanke, F., Hüdepohl, L., et al. 2012, *PTEP*, **2012**, 01A309  
 Janka, H.-T., Müller, B., Kitaura, F. S., & Buras, R. 2008, *A&A*, **485**, 199  
 Janka, H.-T., & Müller, E. 1996, *A&A*, **306**, 167  
 Jerkstrand, A., Timmes, F. X., Magkotsios, G., et al. 2015, *ApJ*, **807**, 110  
 Käppeler, F., Gallino, R., Bisterzo, S., & Aoki, W. 2011, *RvMP*, **83**, 157  
 Kasen, D., & Woosley, S. E. 2009, *ApJ*, **703**, 2205  
 Katz, B., Kushnir, D., & Dong, S. 2013, arXiv:1301.6766  
 Kifonidis, K., Plewa, T., Janka, H.-T., & Müller, E. 2003, *A&A*, **408**, 621  
 Kitaura, F. S., Janka, H.-T., & Hillebrandt, W. 2006, *A&A*, **450**, 345  
 Kochanek, C. S. 2014, *ApJ*, **785**, 28  
 Kochanek, C. S. 2015, *MNRAS*, **446**, 1213  
 Kushnir, D. 2015, arXiv:1506.02655  
 Langer, N. 1992, *A&A*, **265**, L17  
 Lattimer, J. M. 2012, *ARNPS*, **62**, 485  
 Lattimer, J. M., & Prakash, M. 2001, *ApJ*, **550**, 426  
 Lattimer, J. M., & Swesty, F. D. 1991, *NuPhA*, **535**, 331  
 Li, W., Chornock, R., Leaman, J., et al. 2011, *MNRAS*, **412**, 1473  
 Liebendörfer, M. 2005, *ApJ*, **633**, 1042  
 Limongi, M., & Chieffi, A. 2006a, *ApJ*, **647**, 483  
 Limongi, M., & Chieffi, A. 2006b, *NewAR*, **50**, 474  
 Lodders, K. 2003, *ApJ*, **591**, 1220  
 Longland, R., Iliadis, C., & Karakas, A. I. 2012, *PhRvC*, **85**, 065809  
 Lovegrove, E., & Woosley, S. E. 2013, *ApJ*, **769**, 109  
 Maeder, A. 1987, *A&A*, **178**, 159  
 Maeder, A. 1992, *A&A*, **264**, 105  
 Meléndez, J., & Barbuy, B. 2002, *ApJ*, **575**, 474  
 Melson, T., Janka, H.-T., & Marek, A. 2015, *ApJL*, **801**, L24  
 Meynet, G., & Arnould, M. 1993, in Proc. 2nd Int. Symp. on Nuclear Astrophysics, Nuclei in the Cosmos, Vol. 2, ed. F. Käppeler & K. Wisshak (Bristol: IOP Publishing), 503  
 Mirizzi, A., Tamborra, I., Janka, H.-Th., et al. 2015, *La Rivista del Il Nuovo Cimento*, **39**, 1  
 Morris, T., & Podsiadlowski, P. 2007, *Sci*, **315**, 1103  
 Müller, B. 2015, *MNRAS*, arXiv:1506.05139  
 Müller, E. 1986, *A&A*, **162**, 103  
 Nadezhin, D. K. 1980, *Ap&SS*, **69**, 115  
 Nieuwenhuijzen, H., & de Jager, C. 1990, *A&A*, **231**, 134  
 Nomoto, K. 1987, *ApJ*, **322**, 206  
 Nomoto, K., & Hashimoto, M. 1988, *PhR*, **163**, 13  
 Nomoto, K., Kobayashi, C., & Tominaga, N. 2013, *ARA&A*, **51**, 457  
 Nomoto, K., Sugimoto, D., Sparks, W. M., et al. 1982, *Natur*, **299**, 803  
 O’Connor, E., & Ott, C. D. 2011, *ApJ*, **730**, 70

- Özel, F., Psaltis, D., Narayan, R., & Santos Villarreal, A. 2012, *ApJ*, **757**, 55
- Pejcha, O., & Prieto, J. L. 2015, *ApJ*, **806**, 225
- Pejcha, O., & Thompson, T. A. 2015, *ApJ*, **801**, 90
- Podsiadlowski, P. 1992, *PASP*, **104**, 717
- Popov, D. V. 1993, *ApJ*, **414**, 712
- Poznanski, D. 2013, *MNRAS*, **436**, 3224
- Rauscher, T., Heger, A., Hoffman, R. D., & Woosley, S. E. 2002, *ApJ*, **576**, 323
- Rogers, F. J., & Iglesias, C. A. 1992, *ApJS*, **79**, 507
- Saio, H., Nomoto, K., & Kato, M. 1988, *Natur*, **334**, 508
- Salpeter, E. E. 1955, *ApJ*, **121**, 161
- Scalo, J. M. 1986, *FCPh*, **11**, 1
- Scheck, L., Kifonidis, K., Janka, H.-T., & Müller, E. 2006, *A&A*, **457**, 963
- Schwab, J., Podsiadlowski, P., & Rappaport, S. 2010, *ApJ*, **719**, 722
- Seitenzahl, I. R., Cescutti, G., Röpke, F. K., Ruiter, A. J., & Pakmor, R. 2013a, *A&A*, **559**, L5
- Seitenzahl, I. R., Ciaraldi-Schoolmann, F., Röpke, F. K., et al. 2013b, *MNRAS*, **429**, 1156
- Shigeyama, T., & Nomoto, K. 1990, *ApJ*, **360**, 242
- Shigeyama, T., Nomoto, K., & Hashimoto, M. 1988, *A&A*, **196**, 141
- Shiode, J. H., & Quataert, E. 2014, *ApJ*, **780**, 96
- Sieverding, A., Huther, L., Langanke, K., Martínez-Pinedo, G., & Heger, A. 2015, arXiv:1505.01082
- Smartt, S. J. 2009, *ARA&A*, **47**, 63
- Smartt, S. J. 2015, *PASA*, **32**, e016
- Smith, N. 2007, *AJ*, **133**, 1034
- Smith, N. 2013, *MNRAS*, **434**, 102
- Smith, N., & Arnett, W. D. 2014, *ApJ*, **785**, 82
- Spiro, S., Pastorello, A., Pumo, M. L., et al. 2014, *MNRAS*, **439**, 2873
- Steiner, A. W., Hempel, M., & Fischer, T. 2013, *ApJ*, **774**, 17
- Sukhbold, T., & Woosley, S. E. 2014, *ApJ*, **783**, 10
- Suntzeff, N. B., Phillips, M. M., Elias, J. H., Walker, A. R., & Depoy, D. L. 1992, *ApJL*, **384**, L33
- Thielemann, F.-K., Nomoto, K., & Hashimoto, M.-A. 1996, *ApJ*, **460**, 408
- Timmes, F. X., Woosley, S. E., Hartmann, D. H., et al. 1995, *ApJ*, **449**, 204
- Timmes, F. X., Woosley, S. E., & Taam, R. E. 1994, *ApJ*, **420**, 348
- Timmes, F. X., Woosley, S. E., & Weaver, T. A. 1995, *ApJS*, **98**, 617
- Tominaga, N., Blinnikov, S. I., & Nomoto, K. 2013, *ApJL*, **771**, L12
- Ugliano, M., Janka, H.-T., Marek, A., & Arcones, A. 2012, *ApJ*, **757**, 69
- Utrobin, V., Wongwathanarat, A., Janka, H.-T., & Mueller, E. 2014, *A&A*, **581**, A40
- Utrobin, V. P. 2005, *AstL*, **31**, 806
- Utrobin, V. P., & Chugai, N. N. 2011, *A&A*, **532**, A100
- Valenti, S., Fraser, M., Benetti, S., et al. 2011, *MNRAS*, **416**, 3138
- Vinkó, J., Takáts, K., Szalai, T., et al. 2012, *A&A*, **540**, A93
- Walborn, N. R., Lasker, B. M., Laidler, V. G., & Chu, Y.-H. 1987, *ApJL*, **321**, L41
- Wanajo, S., Janka, H.-T., & Kubono, S. 2011a, *ApJ*, **729**, 46
- Wanajo, S., Janka, H.-T., Müller, B., & Kubono, S. 2011b, *JPhCS*, **312**, 042008
- Wanajo, S., Janka, H.-Th., & Müller, B. 2011c, *ApJL*, **726**, L15
- Wang, W., Harris, M. J., Diehl, R., et al. 2007, *A&A*, **469**, 1005
- Weaver, T. A., & Woosley, S. E. 1980, in Ninth Texas Symp. on Relativistic Astrophysics, ed. J. Ehlers, J. J. Perry, & M. Walker (New York: NY Academy of Science), 335
- Weaver, T. A., Zimmerman, G. B., & Woosley, S. E. 1978, *ApJ*, **225**, 1021
- Weiss, A., Hillebrandt, W., & Truran, J. W. 1988, *A&A*, **197**, L11
- Wellstein, S., & Langer, N. 1999, *A&A*, **350**, 148
- Wheeler, J. C., Sneden, C., & Truran, J. W., Jr. 1989, *ARA&A*, **27**, 279
- Wiktorowicz, G., Belczynski, K., & Maccarone, T. 2014, *ApJ*, submitted (arXiv:1312.5924)
- Woosley, S. E. 1988, *ApJ*, **330**, 218
- Woosley, S. E., Hartmann, D. H., Hoffman, R. D., & Haxton, W. C. 1990, *ApJ*, **356**, 272
- Woosley, S. E., & Heger, A. 2006, *ApJ*, **637**, 914
- Woosley, S. E., & Heger, A. 2007, *PhR*, **442**, 269
- Woosley, S. E., & Heger, A. 2015, *ApJ*, **810**, 34
- Woosley, S. E., Heger, A., & Weaver, T. A. 2002, *RvMP*, **74**, 1015
- Woosley, S. E., Heger, A., Weaver, T. A., & Langer, N. 1997, arXiv:astro-ph/9705146
- Woosley, S. E., & Kasen, D. 2011, *ApJ*, **734**, 38
- Woosley, S. E., Langer, N., & Weaver, T. A. 1993, *ApJ*, **411**, 823
- Woosley, S. E., Pinto, P. A., & Enzman, L. 1988, *ApJ*, **324**, 466
- Woosley, S. E., & Weaver, T. A. 1995, *ApJS*, **101**, 181
- Yamaguchi, H., Badenes, C., Foster, A. R., et al. 2015, *ApJL*, **801**, L31
- Yang, H., & Chevalier, R. A. 2015, *ApJ*, **806**, 153
- Zhang, W., Woosley, S. E., & Heger, A. 2008, *ApJ*, **679**, 639